MEASUREMENT AND INTERPRETATION OF CRUSTAL DEFORMATION RATES ASSOCIATED WITH POSTGLACIAL REBOUND

GRANT NAG5-1930

Semiannual Status Report No. 4

For the Period 15 September 1993 through 14 March 1994

Principal Investigator

Dr. James L. Davis

March 1994

Prepared for
National Aeronautics and Space Administration
Washington, D.C. 20546

Smithsonian Institution
Astrophysical Observatory
Cambridge, Massachusetts 02138

The Smithsonian Astrophysical Observatory is a member of the Harvard-Smithsonian Center for Astrophysics

The NASA Technical Officer for this Grant is Dr. Bruce Bills, Code 921, Laboratory for Terrestrial Physics, Earth Sciences Directorate, NASA Goddard Space Flight Center, Greenbelt, Maryland 20771

Appendix. Mitrovica et al. [1994a] and [1994b]

I. Introduction

This project involves obtaining GPS measurements in Scandinavia, and using the measurements to estimate the viscosity profile of the Earth's mantle and to correct tide-gauge measurements for the rebound effect. Below, we report on several aspects of this project.

II. GPS Measurements

The DSGS was not scheduled to be reoccupied with DOSE receivers during the report period. The permanent network set up by Onsala Space Observatory continues to operate, and the data are being evaluated.

III. Theoretical Advances

An important technical advance we intend for this project is to use the full three-dimensional site velocity information for inferring geophysical parameters. During the report period, two papers [Mitrovica et al. 1994a,b] have been been accepted for publication in the Journal of Geophysical Research and will be published in April. Reprints of these papers are contained in the Appendix.

References

Mitrovica, J.X., J.L. Davis, and I.I. Shapiro, A spectral formalism for computing three-dimensional deformations due to surface loads, 1. Theory, *J. Geophys. Res.*, in press, 1994a.

Mitrovica, J.X., J.L. Davis, and I.I. Shapiro, A spectral formalism for computing three-dimensional deformations due to surface loads, 2. Present-day glacial isostatic adjustment, *J. Geophys. Res.*, in press, 1994b.

AGU JGR galley style, v3.0, 29 Oct 93

A spectral formalism for computing three-dimensional deformations due to surface loads
1. Theory

J. X. Mitrovica
Department of Physics, University of Toronto, Toronto, Ontario, Canada

J. L. Davis and I. I. Shapiro
Harvard-Smithsonian Center for Astrophysics, Cambridge, Massachusetts

Abstract. We outline a complete spectral formalism for computing high spatial resolution three-dimensional deformations arising from the surface mass loading of a spherically symmetric planet. The main advantages of the formalism are that all surface mass loads are always described using a consistent mathematical representation (expansions using spherical harmonic basis functions) and that calculations of deformation fields for various spatial resolutions can be performed by simply altering the spherical harmonic degree truncation level of the procedure. The latter may be important when incorporating improved observational constraints on a particular surface mass load, when considering potential errors in the computed field associated with mass loading having a spatial scale unresolved by the observational constraints, or when treating a number of global surface mass loads constrained with different spatial resolutions. These advantages do not extend to traditional "Green's function" approaches which involve surface element discretizations of the global mass loads. In the practical application of the Green's function approach the discretization is subjective and dependent on the particular surface mass load being considered. Furthermore, treatment of mass loads with higher spatial resolutions can require tedious rediscretization of the surface elements. Another advantage of the spectral formalism, over the Green's function approach, is that a posteriori analyses of the computed deformation fields, such as degree correlations, power spectra, and filtering analyses, are easily performed. In developing the spectral formalism, we consider specific cases where the Earth's mantle is assumed to respond as an elastic, slightly anelastic, or linear viscoelastic medium. In the case of an elastic or slightly anelastic mantle rheology the spectral response equations incorporate frequency dependent Love numbers. The formalism can therefore be used, for example, to compute the potentially resonant deformational response associated with the free core nutation and Chandler wobble eigenfunctions. For completeness, the spectral response equations include both body forces, as arise from the gravitational attraction of the Sun and the Moon, and surface mass loads. In either case, and for both elastic and anelastic mantle rheologies, we outline a pseudo-spectral technique for computing the ocean adjustment associated with the total gravitational perturbation induced by the external forcing. Three-dimensional deformations computed using the usual Love number approach are generally referenced to an origin located at the center of mass of the undeformed planet. We derive a spectral technique for transforming the results to an origin located at the center of mass of the deformed planet.

Paper number 93JB03128.

Introduction

The Earth is subject to a number of external forcings having characteristic time scales which vary over many orders of magnitude. The gravitational potential due to the Sun and the Moon gives rise to both body tides and surface mass load variations associated with ocean tides which have significant power at periods ranging from less than a day to several decades [e.g., *Cartwright and Tayler*, 1971]. Time series of surface pressure measurements indicate comparably large ranges in atmospheric loading time scales [e.g., *Trenberth*, 1981; *Müller and Zürn*, 1983; *Rabbel and Zschau*, 1985]. Furthermore, the mass balance of continent-based ice sheets fluctuates with time scales ranging up to the period of approximately 10^5 years characteristic of the late Pleistocene glacial cycles [e.g., *Shackleton*, 1967; *Broecker and Van Donk*, 1970], though small land-based ice sheets and glaciers are known to be presently melting over significantly shorter timescales [*Meier*, 1984].

The prediction of solid Earth deformations associated with these surface mass loads is a classic problem in geophysics. (See *Farrell* [1972] for a detailed discussion.) The advent and dramatic improvements in the accuracy of space geodetic measurement techniques, including very long baseline interferometry (VLBI), surveying using the Global Positioning System (GPS) and satellite and lunar laser ranging (SLR and LLR), have revived considerable interest in such predictions. Indeed, analyses of the effect of atmospheric loading [e.g., *van Dam and Wahr*, 1987; *van Dam*, 1991], ocean loading [e.g., *Scherneck*, 1991], and late Pleistocene glacial loading [e.g., *Tushingham*, 1991] on baselines determined using space geodetic measurement techniques have all been recently considered.

Solid Earth deformations associated with surface mass loads have been computed using an approach developed from the work of *Longman* [1962, 1963] and *Farrell* [1972]. *Farrell* [1972], following *Longman* [1962, 1963], computed Green's functions for the radial and tangential displacements associated with the impulse loading of a spherically symmetric planet having an elastic mantle rheology. The response of the Earth model to an arbitrary surface mass load can then be computed via a surface convolution of the mass load with the appropriate Green's function. In the practical application of *Farrell's* [1972] Green's function approach the surface mass load is commonly discretized using a number of surface elements [*Jentzcsh*, 1985]. The response of the Earth model as a function of position relative to a set of such surface elements with varying geometries is precomputed. The two-dimensional convolution required to obtain the response to an arbi-

0148-0227/94/93JB-03128$05.00

trary surface mass load then reduces to a weighted sum of a relatively small number of "surface element" responses. The discretization procedure clearly reduces the effort involved in generating a number of different deformation fields. Nevertheless, it is also motivated by the finite spatial resolution with which the surface mass loads are known. As an example, *van Dam and Wahr* [1987] discretized their atmospheric load into a 2.5° × 2.5° grid system to be consistent with the resolution of the meteorological data sets available to them.

There have been recent attempts to compute Green's functions for Earth models of increasing complexity. For example, a number of analyses have incorporated the effect of mantle anelasticity on the impulse response [*Wang*, 1986; *Scherneck*, 1991; *Pagiatakis*, 1990]. Furthermore, *Pagiatakis* [1990] has also considered the influence of mantle anisotropy. In a summary of these results, *Scherneck* [1991] has shown that discrepancies between the Green's functions derived by *Scherneck* [1991] and *Pagiatakis* [1990] and those of *Farrell* [1972] are generally less than 2%.

The Green's function approach has also been extended to consider the (deformational and sea level) response of an Earth model with a linear viscoelastic mantle rheology to an applied surface mass load [*Peltier*, 1974]. The most common application is the analysis of the response of the Earth to the last major deglaciation event of the current ice age [e.g., *Peltier and Andrews*, 1976; *Clark et al.*, 1978; *Wu and Peltier*, 1983; *Peltier*, 1985; *Tushingham*, 1991; *James and Lambert*, 1993]. In the case of a viscoelastic mantle rheology, the impulse response Green's functions are dependent on time, as well as on the angular distance from the point load. As a consequence, a calculation of the response of an Earth model to various surface load elements becomes substantially more time consuming. In this regard, the recent analysis of *Tushingham and Peltier* [1991] has adopted a circular disk load discretization of the late Pleistocene ice sheets in which the smallest disk diameter is 1°.

In its practical application the main disadvantages of the Green's function approach are that the surface elements are arbitrarily chosen (and are often dependent, in the literature, on the particular global mass load being considered) and that changes in the spatial resolution of the surface mass load often require a tedious rediscretization of the load geometry. (Compare, for example, the discretizations of *Wu and Peltier* [1983] and *Tushingham and Peltier* [1991].) It is, as a consequence, difficult to consider the effect on the predicted deformation field of discretization errors associated with the representation of the surface mass load. Furthermore, the a priori construction of the Green's function generally involves a sum to very high harmonic degree (*Farrell* [1972] truncated the sum at degree 10,000) which is not necessarily consistent with the observationally constrained resolution available

regarding the surface mass load. In the case of an elastic mantle rheology this fact is of little consequence since the summation is performed only once. However, in the viscoelastic case, where the radial viscosity profile is generally a free parameter, Green's functions (which depend on this profile) may be computed many times. Hence a method which incorporates the impulse response of the Earth model to a spherical harmonic degree consistent with the resolution of the surface load is advantageous.

In this paper we outline a spectral, i.e., spherical harmonic, formalism for computing three-dimensional deformations arising from surface mass loads. Within the formalism, all surface mass loads are described using a consistent mathematical representation based upon spherical harmonic decompositions and the surface convolutions required to compute the radial and tangential surface displacements associated with the load can be performed analytically. In this case, the resulting analytic expressions truncate at the spherical harmonic degree level chosen for the surface mass load (which, in turn, will be governed by the observational constraints on that mass load). Consideration of different spatial resolutions will require no more preliminary effort than a change in this truncation level. Another obvious advantage of a spectral formalism is that a posteriori analyses of the computed deformation fields, such as the determination of power spectra and degree correlations or the filtering of specific spatial wavelengths, are trivially performed.

As *Farrell* [1972] has pointed out in regard to the surface-mass-load problem, the primary disadvantage of spectral techniques is that their spatial resolution is independent of position. As a consequence, incorporating highly resolved observational constraints at one location on the Earth's surface forces better resolution than may be necessary from observational constraints from other regions. The computational power and availability of modern work stations, however, make this argument less of a practical limitation than it was 20 years ago. For example, we have implemented the algorithms presented below on a Hewlett-Packard model 730 work station (employing RISC architecture) with 32 Mbytes of RAM and found that with no special techniques we are able rapidly to obtain spherical harmonic truncation levels of degree 2048 when considering the deformation field induced by a specific surface mass load. This resolution corresponds to a spatial resolution of 0.1° or 10 km, superior to the resolution adopted in analyses of the deformation of the Earth based on the surface element Green's function approach. (The spatial resolutions described above in the context of recent analyses of this type are an indication of this disparity.) In this regard, the spatial resolutions we have obtained are certainly better than those which characterize current observational constraints on the various global surface mass loads. These results suggest that

it is time to reconsider the utility of spectral techniques in analyses of Earth deformations by surface loads; it is intended that this study will provide the algorithms necessary to do so.

To our knowledge, the analysis of *Pertsev* [1966] was the first to suggest using a spectral approach to compute the response of an Earth model whose Love numbers have been calculated. *Pertsev* [1966] was specifically concerned with variations in gravity associated with semidiurnal ocean tides on an elastic Earth. In addition, *Peltier* [1976] derived, but did not apply, a spectral formalism for computing radial deformations on a linear viscoelastic Earth. Spectral formalisms have also been derived to compute the redistribution of ocean mass associated with the melting of late Pleistocene ice sheets on a viscoelastic Earth [*Nakada and Lambeck*, 1987; *Mitrovica and Peltier*, 1991a]. The *Nakada and Lambeck* [1987] approach represents an approximate solution to the governing sea level equation, while the spectral and pseudo-spectral algorithms described by *Mitrovica and Peltier* [1991a] yield a gravitationally self-consistent solution of the equilibrium ocean adjustment. Finally, *Dickman* [1989] has outlined a spherical harmonic approach to predicting long-period ocean tides which incorporates a number of important physical effects (ocean bottom friction, etc.). Regardless of the assumed mantle rheology, horizontal deformations induced by surface mass loads have not, to date, been treated using a spectral approach.

In deriving a spectral formalism for computing three-dimensional deformations, we will consider Earth models characterized by elastic, slightly anelastic, and viscoelastic mantle responses. In the case of elastic and anelastic mantle rheologies, we incorporate frequency dependent Love numbers in the derivation of the spectral response equations. As a consequence, the formalism can be used, for example, to predict the resonant deformational response associated with mass load variations having frequencies near the eigenfrequencies of the free core nutation and Chandler wobble normal modes of the planet [*Wahr*, 1981a,b]. The spectral response equations require, as input, the spherical harmonic coefficients of the surface mass load and the Love numbers appropriate to the rheological model being considered. The reader is referred to the discussions of *Longman* [1962, 1963] and *Farrell* [1972], *Wahr and Bergen* [1986], and *Peltier* [1974, 1985], for the treatment of Earth models with, respectively, elastic, anelastic, and linear viscoelastic mantle rheologies.

The Love numbers are generally defined such that displacements computed using them are referenced to an origin located at the center of mass of the undeformed planet. (See *Farrell* [1972] for a detailed discussion of this point.) As a consequence, the computed positions will include a component associated with a pure translation of the center of mass of the deformed planet (which

does not include the surface mass load) relative to its original position. To complete the present study, we provide a straightforward spectral approach for transforming the computed positions to a reference frame whose origin is located at the center of mass of the deformed planet. The latter positions are more accurately interpreted as "deformations."

For the case of elastic and anelastic mantle rheologies we provide a pseudo-spectral technique for computing the ocean adjustment associated with the gravitational perturbation induced by the surface mass loading. The technique outputs the spherical harmonic coefficients of the ocean adjustment, as do the algorithms of *Nakada and Lambeck* [1987] and *Mitrovica and Peltier* [1991a] for the viscoelastic case, as well as that of *Dickman* [1989] for his ocean tide theory. As a consequence, the spectral response equations derived herein are well suited for computing the three-dimensional crustal deformations associated with these mass redistributions.

In a companion article [*Mitrovica et al.*, this issue] we considered predictions of present-day three-dimensional crustal deformation rates associated with the melting of the late Pleistocene ice sheets. We will use the spectral response equations derived herein to predict the three-dimensional deformations which arise from a realistic space-time deglaciation chronology and gravitationally self-consistent ocean mass adjustments.

A Love Number Formulation of the Earth's Response to External Loads

In this and following sections we develop a complete spectral formalism for computing the response of a spherically symmetric, self-gravitating planet to an arbitrary external load. We focus mainly on radial and tangential surface deformations. Nevertheless, the theory can also be used with the appropriate Green's function (see below) to compute anomalies in the gravitational field of the planet. As discussed in the introduction, we consider elastic, anelastic, and linear viscoelastic mantle rheologies and in each case incorporate gravitationally self-consistent ocean loading components in the formulation. The spectral formalism is based on the usual Love number formulation of the external loading problem which we review, briefly, below.

Farrell [1972], following *Longman* [1962, 1963], outlined a numerical procedure for determining the tidal and surface load Love numbers of a spherically symmetric, self-gravitating Earth having an elastic mantle and a fluid core. These numbers, originally defined by *Love* [1909] (and also by *Shida and Matsuyama* [1912]), govern the response of the planetary model to a gravitational potential and surface mass load forcing, respectively. In consider-

ing the Earth's tidal response, let us begin by assuming an Earth model which experiences no frictional dissipation (i.e., we assume no anelastic component of the response). In this case the tidal Love numbers may be written in the form

$$h_\ell^T = h_\ell^{T,E} \tag{1}$$

$$l_\ell^T = l_\ell^{T,E} \tag{2}$$

$$k_\ell^T = k_\ell^{T,E} \tag{3}$$

where the superscript E denotes a coefficient determined from a model with a purely elastic mantle rheology and l is the spherical harmonic degree. The Love numbers h_ℓ^T, l_ℓ^T, and k_ℓ^T represent coefficients in harmonic expansions of the radial and tangential displacement and a potential perturbation due to the planetary mass redistribution (i.e., body tide), respectively, induced by the tidal potential.

Let us denote the tidal potential on the Earth's surface at a geographic location of colatitude θ, east longitude ψ, and time t, as $W(\theta,\psi,t)$. Practical representations of $W(\theta,\psi,t)$ have traditionally been based on the determination of time dependent coefficients in a spherical harmonic expansion of the tidal potential [e.g., *Cartwright and Tayler,* 1971; *Cartwright and Edden,* 1973]. We can thus write

$$W(\theta,\psi,t) = \sum_{\ell=2}^{\infty} \sum_{m=-\ell}^{\ell} W_{\ell m}(t)\, Y_{\ell m}(\theta,\psi)\,. \tag{4}$$

The $Y_{\ell m}(\theta,\psi)$ are surface spherical harmonics normalized (in our formalism) such that

$$\iint_\Omega Y^*_{\ell' m'}(\theta,\psi) Y_{\ell m}(\theta,\psi) \sin\theta \; d\theta d\psi = 4\pi \delta_{\ell\ell'} \delta_{mm'}\,, \tag{5}$$

where $\iint_\Omega$ is used to indicate integration over the entire solid angle and δ_{ij} is the Kronecker delta.

Using (1)–(3) and (4), the response of the Earth to the tidal potential may be written as [*Melchior,* 1983]

$$U^T(\theta,\psi,t) = \frac{1}{g} \sum_{\ell=2}^{\infty} \sum_{m=-\ell}^{\ell} h_\ell^{T,E}\, W_{\ell m}(t)\, Y_{\ell m}(\theta,\psi) \tag{6}$$

$$\vec{V}^T(\theta,\psi,t) = \frac{1}{g} \sum_{\ell=2}^{\infty} \sum_{m=-\ell}^{\ell} l_\ell^{T,E}\, W_{\ell m}(t)\, \vec{\nabla} Y_{\ell m}(\theta,\psi) \tag{7}$$

and

$$\phi^T(\theta,\psi,t) = \sum_{\ell=2}^{\infty} \sum_{m=-\ell}^{\ell} k_\ell^{T,E}\, W_{\ell m}(t)\, Y_{\ell m}(\theta,\psi)\,, \tag{8}$$

where U^T and $\vec{V}^T$ are the radial and tangential body tide displacements, ϕ^T is the potential perturbation due to the planetary mass redistribution, and g is the surface gravitational acceleration. The symbol $\vec{\nabla}$ denotes the two-dimensional gradient operator:

$$\vec{\nabla} = \hat{\theta}\frac{\partial}{\partial\theta} + \hat{\psi}\frac{1}{\sin\theta}\frac{\partial}{\partial\psi} \ . \tag{9}$$

The terms $\vec{\nabla}Y_{\ell m}(\theta,\psi)$ will play an important role in this study, and in the appendix we provide expressions for them in terms of a set of $Y_{\ell m}(\theta,\psi)$.

Equations (6)–(8) may be used to compute the basic deformational and gravitational response of the solid Earth to the tidal potential forcing. The equations can be combined to generate expressions for other responses of geophysical importance. For example, in considering the gravitationally self-consistent redistribution of ocean mass induced by the tidal potential (as we do below), it is useful to have an expression for the gravitational potential perturbation at the deformed solid surface induced by both the tidal potential and the resulting body tides. The perturbation, which we denote by $\Phi^T(\theta,\psi,t)$, is [*Longman,* 1963]

$$\Phi^T(\theta,\psi,t) = \sum_{\ell=2}^{\infty}\sum_{m=-\ell}^{\ell}\left[1 + k_\ell^{T,E} - h_\ell^{T,E}\right] W_{\ell m}(t)\ Y_{\ell m}(\theta,\psi) \ , \tag{10}$$

where the term equal to unity reflects the direct effect of the tidal potential and the term $h_\ell^{T,E}$ arises from transforming from the undeformed to the deformed solid surface.

Let us turn now to the surface load Love numbers. In computing the response of the Earth to variations in surface mass loads we will consider examples where both elastic and linear viscoelastic mantle rheologies are relevant. As a consequence, we require an extension of the elastic Love number forms (1)–(3) to the general linear viscoelastic case. Such an extension has been provided by *Peltier* [1974, 1976], who invoked the correspondence principle [*Biot,* 1954] to derive so-called viscoelastic surface load Love numbers. These dimensionless numbers define the response of the Earth model to an applied point impulse load. In the time domain these Love numbers, which we denote as h_ℓ^L, l_ℓ^L, and k_ℓ^L, have the following normal mode form [*Peltier,* 1976]

$$h_\ell^L(t) = h_\ell^{L,E}\delta(t) + \sum_{k=1}^{K(\ell)} r1_k^{L,\ell}\exp(-s_k^\ell t) \tag{11}$$

$$l_\ell^L(t) = l_\ell^{L,E}\delta(t) + \sum_{k=1}^{K(\ell)} r2_k^{L,\ell}\exp(-s_k^\ell t) \tag{12}$$

and

$$k_\ell^L(t) = k_\ell^{L,E}\delta(t) + \sum_{k=1}^{K(\ell)} r3_k^{L,\ell} \exp(-s_k^\ell t) \; . \qquad (13)$$

The first term on the right-hand sides of each of (11)–(13) represents the instantaneous elastic response to an applied point mass impulse load. The second term is the nonelastic response which is represented by a superposition of $K(\ell)$ modes of pure exponential decay. The formalism outlined by *Peltier* [1985] can be used to compute the normal mode amplitudes $r1_k^{L,\ell}$, $r2_k^{L,\ell}$, and $r3_k^{L,\ell}$ and the inverse decay times (eigenfrequencies) s_k^ℓ.

The h_ℓ^L, l_ℓ^L, and k_ℓ^L surface load Love numbers represent the coefficients of degree ℓ in Legendre polynomial expansions of Green's functions for the radial and tangential displacement and the potential perturbation due to mass redistribution of the planet, respectively. The Green's functions can be written as

$$G_U^L(\gamma, t) = \frac{a}{M_e} \sum_{\ell=0}^{\infty} h_\ell^L(t) P_\ell(\cos\gamma) \qquad (14)$$

$$\vec{G}_V^L(\gamma, t) = \frac{a}{M_e} \sum_{\ell=0}^{\infty} l_\ell^L(t) \; \frac{\partial}{\partial\gamma} P_\ell(\cos\gamma) \; \hat{\gamma} \qquad (15)$$

and

$$G_\phi^L(\gamma, t) = \frac{ag}{M_e} \sum_{\ell=0}^{\infty} k_\ell^L(t) \; P_\ell(\cos\gamma), \qquad (16)$$

respectively, where a is the mean radius of the Earth and M_e its mass, $\hat{\gamma}$ is a unit vector tangent to the surface (i.e., horizontal) in the direction of the great circle extending from the load point (θ', ψ') to the observation point (θ, ψ), and γ is the angular distance between these two points, given by

$$\cos\gamma = \cos\theta\cos\theta' + \sin\theta\sin\theta'\cos(\psi - \psi'). \qquad (17)$$

The Green's functions (14)–(16) can be combined to generate Green's functions for a number of geophysical observables. *Mitrovica and Peltier* [1989] have derived Green's functions for both the free air gravity anomaly and the geoid anomaly. (See also *Mitrovica and Peltier* [1991b].) *Longman* [1963] determined Green's functions for both the gravity anomaly and the gravitational potential perturbation at the deformed surface for the case of an elastic mantle rheology. In the viscoelastic case the gravitational potential perturbation Green's function G_Φ^L has the following form [*Peltier and Andrews*, 1976]:

$$G_\Phi^L(\gamma, t) = \frac{ag}{M_e} \sum_{\ell=0}^{\infty} \Bigg[\left(1 + k_\ell^{L,E} - h_\ell^{L,E}\right) \delta(t) + \sum_{k=1}^{K(\ell)} \left(r3_k^{L,\ell} - r1_k^{L,\ell}\right) \exp\left(-s_k^\ell t\right) \Bigg] P_\ell(\cos\gamma) \quad (18)$$

where the term equal to unity in the multiplier term of the delta function incorporates the direct gravitational attraction of the impulse load and the terms in $h_\ell^{L,E}$ and $r1_k^{L,\ell}$ arise from transforming from the undeformed to the deformed surface.

The response of a spherically symmetric, self-gravitating, viscoelastic planet to an arbitrary surface mass load $L(\theta,\psi,t)$ (with dimensions of mass per unit area) can be computed by convolving the load, in the space and time dimensions, with the appropriate Green's function. If we denote a general Green's function as $G^L(\gamma,t)$, then the response R is given by

$$R(\theta,\psi,t) = \int_{-\infty}^{t} \iint_{\Omega} a^2 L(\theta',\psi',t') G^L(\gamma, t-t') d\Omega'\, dt', \qquad (19)$$

where γ is given by (17). The response $R(\theta,\psi,t)$ will be a scalar quantity for the case of the Green's functions G_U^L, G_ϕ^L, and G_Φ^L, and a vector quantity for the tangential displacement Green's function $\vec{G}_V^L$.

The Green's functions (14)–(16) represent extensions to the viscoelastic case of the analogous Green's functions described by *Longman* [1963] and *Farrell* [1972] for the purely elastic case. Indeed, the latter can be derived from the former by considering only the elastic component of (11)–(13) in the summations of (14)–(16), that is, for the special case of a purely elastic response, we can write

$$G_U^{L,E}(\gamma) = \frac{a}{M_e} \sum_{\ell=0}^{\infty} h_\ell^{L,E} P_\ell(\cos\gamma) \qquad (20)$$

$$\vec{G}_V^{L,E}(\gamma) = \frac{a}{M_e} \sum_{\ell=0}^{\infty} l_\ell^{L,E} \frac{\partial}{\partial\gamma} P_\ell(\cos\gamma)\hat{\gamma} \qquad (21)$$

and

$$G_\phi^{L,E}(\gamma) = \frac{ag}{M_e} \sum_{\ell=0}^{\infty} k_\ell^{L,E} P_\ell(\cos\gamma). \qquad (22)$$

In this case the general response (19) would simplify to

$$R^E(\theta,\psi,t) = \iint_{\Omega} a^2 L(\theta',\psi',t) G^{L,E}(\gamma)\, d\Omega'. \qquad (23)$$

The now classic method of computing the response $R^E(\theta,\psi,t)$ discussed by *Farrell* [1972] consists of a direct application of (20)–(23). First, the Love numbers $h_\ell^{L,E}$, $l_\ell^{L,E}$, and $k_\ell^{L,E}$ are computed for a specific "elastic" Earth model. Second, the summations in (20)–(22) are computed to very high spherical harmonic degree by making use of asymptotic properties associated with infinite sums. Finally, the convolution between the Green's

function and the specified load $L(\theta, \psi, t)$ is computed in the space domain numerically. In this respect, the two-dimensional convolution can be discretized by using (20)–(22) to compute Green's functions for finite surface elements [*Jentzsch*, 1985]. These elements are commonly chosen to be circular disks (in which case "equivalent" Green's functions need to be computed for disks of various sizes and at various angular distances from the observation point), but *Goad* [1980], for example, has advocated the use of surface ring sectors. Other discretizations are also common [e.g., *van Dam*, 1991].

The *Farrell* [1972] methodology has been adopted by, for example, *Rabbel and Zschau* [1985], *van Dam and Wahr* [1987], and *van Dam* [1991] in considering deformations and gravity changes associated with atmospheric loading. The same approach has also been used to consider the planetary response to tidal loading [*Goad*, 1980; *Wang*, 1986; *Francis and Dehant*, 1987; *Scherneck*, 1991].

The majority of numerical predictions of the glacial isostatic adjustment of the Earth in consequence of the melting of the late Pleistocene ice sheets have proceeded via an extension of *Farrell's* [1972] space-domain convolution approach to the viscoelastic case, as defined by (14)–(19). These studies include the analysis of gravitationally self-consistent sea level change [*Farrell and Clark*, 1976; *Peltier et al.*, 1978; *Wu and Peltier*, 1983], as well as crustal deformations [e.g., *Peltier*, 1974; *James and Morgan*, 1990; *Spada et al.*, 1992]. Indeed, as discussed in the introduction, predictions of three-dimensional crustal deformations associated with the phenomenon have only been computed using such an approach. In the viscoelastic case, calculation of the point mass Green's functions (or of the surface element Green's functions) requires substantially more effort than in the elastic case, since the functions are time dependent.

In the next section we outline a special approach which allows for the analytic determination of the required surface convolution integrals. In subsequent sections the results are applied to consider the response of Earth models having elastic, anelastic, and viscoelastic rheologies, to arbitrary surface loads.

Response to an Arbitrary Surface Mass Load of a Spherically Symmetric Earth: A Spectral Approach

As in the case of the tidal potential, let us represent the surface load $L(\theta, \psi, t)$ in terms of a spherical harmonic expansion of the form

$$L(\theta, \psi, t) = \sum_{\ell,m} L_{\ell m}(t)\, Y_{\ell m}(\theta, \psi), \qquad (24)$$

where we have adopted the short-form notation

$$\sum_{\ell,m} \equiv \sum_{\ell=0}^{\infty} \sum_{m=-\ell}^{\ell} .$$

The surface load Green's functions described in the last section are of two forms, which we may denote symbolically as

$$G_1(\gamma,t) = \sum_{\ell=0}^{\infty} A_\ell(t)\ P_\ell(\cos\gamma) \tag{25}$$

and

$$\vec{G}_2(\gamma,t) = \sum_{\ell=0}^{\infty} B_\ell(t)\ \frac{\partial}{\partial\gamma} P_\ell(\cos\gamma)\hat{\gamma}, \tag{26}$$

where (14), (16), (18), (20), and (22) are of the form (25), whereas the vector Green's function for the tangential displacement (15) and (21) are of the form (26).

To begin, let us consider the form (26). Using (26) and (24) in the response (19) yields

$$\begin{aligned}\vec{R}(\theta,\psi,t) = \sum_{\ell=0}^{\infty} a^2 \int_{-\infty}^{t} B_\ell(t-t') \\ \times \left[\sum_{\ell',m'} L_{\ell'm'}(t') \right. \\ \left. \times \iint_{\Omega} Y_{\ell'm'}(\theta',\psi') \frac{\partial}{\partial\gamma} P_\ell(\cos\gamma)\hat{\gamma}\ d\Omega' \right] dt'\end{aligned} \tag{27}$$

It is straightforward to show that, in general,

$$\frac{\partial}{\partial\gamma} f(\gamma)\hat{\gamma} = \vec{\nabla} f(\gamma), \tag{28}$$

where $\vec{\nabla}$ is the two-dimensional gradient operator defined in (10), γ is the arc length defined by (17), $\hat{\gamma}$ is a unit vector defined below (16), and $f(\gamma)$ is an arbitrary function. Equation (28) indicates that the directional derivative operator $\hat{\gamma}\partial/\partial\gamma$ acting on $f(\gamma)$ is equivalent to the gradient operator $\vec{\nabla}$ acting on $f(\gamma)$. The gradient operator is, of course, independent of the load point coordinate (θ',ψ'). Using (28) in (27) yields

$$\begin{aligned}\vec{R}(\theta,\psi,t) = \sum_{\ell=0}^{\infty} a^2 \int_{-\infty}^{t} B_\ell(t-t') \\ \times \left[\sum_{\ell',m'} L_{\ell'm'}(t') \right. \\ \left. \times \iint_{\Omega} Y_{\ell'm'}(\theta',\psi') \vec{\nabla} P_\ell(\cos\gamma)\ d\Omega' \right] dt'\end{aligned} \tag{29}$$

It is clear from (29) that the vector operator (which operates on the unprimed quantities) can be moved outside the surface integral. Doing so, and using the following addition theorem of spherical harmonics [e.g., *Jackson*, 1975],

$$P_\ell(\cos\gamma) = \frac{1}{2\ell+1} \sum_{m=-\ell}^{\ell} Y^*_{\ell m}(\theta',\psi')\, Y_{\ell m}(\theta,\psi) \qquad (30)$$

in (29) yields

$$\vec{R}(\theta,\psi,t) = \sum_{\ell,m} \frac{a^2}{(2\ell+1)} \vec{\nabla} Y_{\ell m}(\theta,\psi) \times \int_{-\infty}^{t} B_\ell(t-t') \left\{ \sum_{\ell',m'} L_{\ell' m'}(t') \times \iint_{\Omega} Y^*_{\ell m}(\theta',\psi') Y_{\ell' m'}(\theta',\psi') d\Omega' \right\} dt' \qquad (31)$$

Finally, using the orthogonality property (5) in (31) generates the expression

$$\vec{R}(\theta,\psi,t) = \sum_{\ell,m} \left\{ \frac{4\pi a^2}{(2\ell+1)} \int_{-\infty}^{t} B_\ell(t-t') L_{\ell m}(t') dt' \right\} \times \vec{\nabla} Y_{\ell m}(\theta,\psi). \qquad (32)$$

An analogous, though simplified, procedure applied to a Green's function of the form (25) yields the following expression for the response:

$$R(\theta,\psi,t) = \sum_{\ell,m} \left\{ \frac{4\pi a^2}{(2\ell+1)} \int_{-\infty}^{t} A_\ell(t-t') L_{\ell m}(t') dt' \right\} \times Y_{\ell m}(\theta,\psi). \qquad (33)$$

The quantity in braces in (33) represents the set of spherical harmonic coefficients for the scalar response $R(\theta,\psi,t)$. That is, if we write the usual spherical harmonic expansion as

$$R(\theta,\psi,t) = \sum_{\ell,m} R_{\ell m}(t) Y_{\ell m}(\theta,\psi), \qquad (34)$$

then clearly,

$$R_{\ell m}(t) = \frac{4\pi a^2}{(2\ell+1)} \int_{-\infty}^{t} A_\ell(t-t') L_{\ell m}(t')\, dt'. \qquad (35)$$

To write the vector response (32) in an analogous, purely spectral form requires more work. The results of the

appendix can be used to generate a set of coefficients $\vec{D}_{\ell m \ell' m'}$ defined such that

$$\vec{\nabla} Y_{\ell m}(\theta, \psi) = \sum_{\ell', m'} \vec{D}_{\ell m \ell' m'} Y_{\ell' m'}(\theta, \psi). \qquad (36)$$

For each ℓ, m pair, only a very small number of coefficients $\vec{D}_{\ell m \ell' m'}$ are nonzero. Using (36) in (32) yields, after a small amount of algebra,

$$\vec{R}(\theta, \psi, t) = \sum_{\ell, m} \vec{R}_{\ell m} Y_{\ell m}(\theta, \psi), \qquad (37)$$

where

$$\vec{R}_{\ell m} = \sum_{\ell', m'} \left[\frac{4\pi a^2}{(2\ell' + 1)} \int_{-\infty}^{t} B_{\ell'}(t - t') L_{\ell' m'}(t') \, dt' \right] \times \vec{D}_{\ell' m' \ell m} \qquad (38)$$

are the required spherical harmonic coefficients of the components of the vector response $\vec{R}(\theta, \psi, t)$.

Equations (34), (35), (37), and (38) represent the spectral expressions sought at the outset of this section. Equations (34) and (35) are relevant to the calculation of the radial displacement response and of anomalies in the gravitational field. Equations (37) and (38) are appropriate for analyses of the horizontal deformations associated with an arbitrary surface mass load.

In the following sections we use the general results derived here to consider several particular applications. First, the three-dimensional deformational response of a spherically symmetric Earth, with an elastic mantle rheology, to an arbitrary external load. Second, we generalize the elastic case to consider the effects of mantle anelasticity. In both the purely elastic and anelastic cases we provide a spectral formalism for computing the response which is generalized to incorporate frequency dependent tidal and surface load Love numbers. In each application we will outline a procedure for incorporating gravitationally self-consistent ocean redistribution contributions to the surface mass load and consider special cases of the various formalisms. Finally, we use the results derived in this section to derive spectral response equations associated with the surface mass load problem on a linear viscoelastic planetary model.

Response to an Arbitrary External Load of a Spherically Symmetric Earth With an Elastic Mantle Rheology

The external load to be considered in this section will consist of a tidal potential $W(\theta, \psi, t)$ and an arbitrary surface mass load. The direct response of the solid Earth

to the tidal potential is given by (6)–(8), and the response to the mass load is given by (32) and (33), as well as (34), (35), (37), and (38). In this section, the $A_\ell(t)$ and $B_\ell(t)$ will be generated from the elastic components of the surface load Love numbers of (11)–(13). It will be instructive to consider a surface mass load separated into several geophysically distinct terms. For example, we can write

$$\begin{aligned} L(\theta,\psi,t) &= L^{\mathrm{ATM}}(\theta,\psi,t) + L^{\mathrm{ICE}}(\theta,\psi,t) \\ &+ L^{\mathrm{EO}}(\theta,\psi,t) + L^{\mathrm{NEO}}(\theta,\psi,t) \\ &+ L^{\mathrm{MISC}}(\theta,\psi,t). \end{aligned} \tag{39}$$

$L^{\mathrm{ATM}}(\theta,\psi,t)$ is the contribution to the surface mass load from atmospheric pressure [e.g., *van Dam and Wahr,* 1987]. $L^{\mathrm{ICE}}(\theta,\psi,t)$ is included to represent the load associated with the recent retreat of small ice sheets and glaciers [*Meier,* 1984] or any mass variation associated with very large ice sheets such as Greenland and Antarctica [e.g., *Zwally,* 1989]. $L^{\mathrm{MISC}}(\theta,\psi,t)$ represents any other surface mass load not associated with ocean mass redistributions. $L^{\mathrm{EO}}(\theta,\psi,t)$ is the contribution to the surface mass load from gravitationally self-consistent ocean mass redistributions caused by the deformation of the Earth due to the tidal potential and the surface mass load and by the direct gravitational effect of these forcings. *Dahlen* [1976] and *Agnew and Farrell* [1978] call this component the "equilibrium ocean tide." We will use the term "equilibrium ocean load" instead since we are including, in general, surface mass load contributions which are not associated with the Earth's response to the tidal potential alone. $L^{\mathrm{NEO}}(\theta,\psi,t)$ represents the portion of the actual ocean mass redistribution not accounted for by the equilibrium ocean load. $L^{\mathrm{NEO}}(\theta,\psi,t)$ can be estimated by considering the difference between $L^{\mathrm{EO}}(\theta,\psi,t)$ and ocean redistributions generated using: general analytic treatments [e.g., *Dickman,* 1989], a combination of observational constraints and theory [*Schwiderski,* 1978] or recent satellite derived observations [*Christodoulidis et al.,* 1988]. Whereas $L^{\mathrm{EO}}(\theta,\psi,t)$ can be computed precisely for a particular Earth model (see the "pseudo-spectral" algorithm below), $L^{\mathrm{NEO}}(\theta,\psi,t)$ is uncertain (see discussion by *Dickman* [1989]), motivating the partition of the two ocean loading terms in (39).

For a particular surface load component $L^i(\theta,\psi,t)$, let us denote the corresponding spherical harmonic coefficients, as in (24), by $L^i_{\ell m}$. Then, using (6) and (7), (11), and (12) (excluding the nonelastic components), (25), (26), (32), (33), and (36) yields the spherical harmonic expansions:

$$U(\theta,\psi,t) = \sum_{\ell,m} U_{\ell m} Y_{\ell m}(\theta,\psi) \tag{40}$$

and

$$\vec{V}(\theta,\psi,t) = \sum_{\ell,m} \vec{V}_{\ell m}(t) Y_{\ell m}(\theta,\psi), \tag{41}$$

where the spherical harmonic coefficients are given by

$$U_{\ell m}(t) = h_\ell^{T,E} \frac{W_{\ell m}(t)}{g} + \frac{4\pi a^3}{(2\ell+1)M_e} h_\ell^{L,E} L_{\ell m}(t) \tag{42}$$

$$\vec{V}_{\ell m}(t) = \sum_{\ell',m'} \left[l_{\ell'}^{T,E} \frac{W_{\ell' m'}(t)}{g} + \frac{4\pi a^3}{(2\ell'+1)M_e} l_{\ell'}^{L,E} L_{\ell' m'}(t) \right] \times \vec{D}_{\ell' m' \ell m}, \tag{43}$$

and

$$\begin{aligned} L_{\ell m}(t) &= L_{\ell m}^{\mathrm{ATM}}(t) + L_{\ell m}^{\mathrm{ICE}}(t) \\ &+ L_{\ell m}^{\mathrm{EO}}(t) + L_{\ell m}^{\mathrm{NEO}}(t) \\ &+ L_{\ell m}^{\mathrm{MISC}}(t). \end{aligned} \tag{44}$$

$U(\theta,\psi,t)$ and $\vec{V}(\theta,\psi,t)$ represent the radial and tangential deformations due to the tidal potential $W(\theta,\psi,t)$ and the total surface mass load $L(\theta,\psi,t)$ acting on a spherically symmetric planet with a purely elastic mantle.

The various contributions to $L_{\ell m}(t)$ of (44) can be generated from a spherical harmonic decomposition of the associated space dependent fields of (39). These fields are, in large part, constrained by observation. For example, $L_{\ell m}^{\mathrm{ATM}}(\theta,\psi,t)$ can be easily generated from meteorological maps of surface pressure variations. As discussed above, the $L_{\ell m}^{\mathrm{EO}}$ are a notable exception to this requirement since they can be computed by solving an equation, known as the sea level equation, based on the gravitational potential perturbation associated with the external loading of the planetary model. In a later section, we provide a straightforward pseudo-spectral algorithm for generating solutions of the sea level equation on a spherically symmetric Earth with an elastic mantle rheology to extremely high spatial resolution. The algorithm outputs the coefficients $L_{\ell m}^{\mathrm{EO}}$ and it is thus particularly well suited for application within the spectral formalism for computing the response of the Earth described above.

Frequency Dependent Love Numbers

The expressions (1)–(3), for the tidal Love numbers and the elastic components of (11)–(13), for the surface load Love numbers, assume that these numbers are constant, independent of (temporal) frequency. In fact, it is well known that these numbers are frequency dependent, in some frequency ranges quite strongly so, and in this section we will generalize the results derived above to incorporate this particularly important aspect of the response of the Earth.

Wahr [1981a,b] has shown that the frequency dependence of the Love numbers can be expressed in terms of resonance expansions. Each of the Love numbers has a nonresonant component which is weakly dependent on frequency, as a consequence of the effect, on the response, of inertial and coriolis forces, and of the ellipticity of the planet. A much stronger frequency dependence is evident in the resonance terms of the Love number expansions [*Wahr*, 1981b] which arise from the existence of certain eigenfunctions in the Earth's free response which include a deformational component; in particular, the Chandler wobble (CW), and the free core nutation (FCN), eigenfunctions. The Love numbers at frequencies near the eigenfrequencies of these eigenfunctions (near 14 months for the CW eigenfunctions and near one sidereal day for the FCN eigenfunction) can differ significantly from the value associated with the nonresonant component alone [*Wahr*, 1981b]. The near-diurnal period of the FCN eigenfunction suggests, given the significant near-diurnal components of the tidal forcing, that predictions of the tidal response of the Earth (for example) should include this frequency dependence. (See also *Schemeck* [1991].) As a consequence, let us write

$$\begin{aligned} h_\ell^{T,E} &= h_\ell^{T,E}(\omega) \\ l_\ell^{T,E} &= l_\ell^{T,E}(\omega) \\ k_\ell^{T,E} &= k_\ell^{T,E}(\omega) \\ h_\ell^{L,E} &= h_\ell^{L,E}(\omega) \\ l_\ell^{L,E} &= l_\ell^{L,E}(\omega) \\ k_\ell^{L,E} &= k_\ell^{L,E}(\omega), \end{aligned} \tag{45}$$

where ω denotes the frequency.

To incorporate (45) into the response equations derived above, we will require explicit expressions for the frequency dependence of the tidal and surface mass load forcing. We begin with the tidal potential.

In the analysis of *Cartwright and Tayler* [1971] and *Cartwright and Edden* [1973] the time dependent coefficients, $W_{\ell m}(t)$ of (4), in the spherical harmonic expansion of the tidal potential are generated by summing a set of pure sinusoids of the specified frequencies and phases. The characteristic periods of the tidal components may be grouped according to the absolute value of the harmonic order m. For example, the $m = 2$ (or sectorial) components have a nearly semidiurnal period; the $m = 1$ (or tesseral) components have a nearly diurnal period; and the $m = 0$ (or zonal) components give rise to the long-period tides [*Melchior*, 1983]. (In the vast majority of applications, sufficient accuracy in (4) is obtained using degrees 2 and 3 only.) Adopting this representational

form for the time dependence in (4) gives

$$W_{\ell m}(t) = \sum_{n=1}^{N_{\ell m}} W^n_{\ell m} \sin\left(\omega^n_{\ell m} t + \xi^n_{\ell m}\right), \qquad (46)$$

where $\omega^n_{\ell m}$, $\xi^n_{\ell m}$, and $W^n_{\ell m}$ represent the angular frequency, phase, and amplitude, respectively, of the n^{th} frequency constituent (in a total of $N_{\ell m}$) of the degree ℓ and order m harmonic of the tidal potential.

In an analogous fashion, the time dependence of the spherical harmonic components of the surface mass load $L_{\ell m}$ can be expressed as

$$L_{\ell m}(t) = \sum_{n=1}^{N_{\ell m}} L^n_{\ell m} \sin\left(\omega^n_{\ell m} t + \xi'^n_{\ell m}\right), \qquad (47)$$

where $\xi'^n_{\ell m}$ is the phase associated with the nth frequency constituent of the degree ℓ and order m harmonic surface mass load. The $N_{\ell m}$ frequency components are included to incorporate all of the time dependence, at degree ℓ and order m, of both the tidal potential and the surface mass loads.

Using (45)–(47), together with (36), the spherical harmonic coefficients (42)–(43) in the spectral response expansions (40)–(41) may be generalized to

$$U_{\ell m}(t) = \sum_{n=1}^{N_{\ell m}} \left[h^{T,E}_{\ell}(\omega^n_{\ell m}) \frac{W^n_{\ell m}}{g} \sin\left(\omega^n_{\ell m} t + \xi^n_{\ell m}\right) + \frac{4\pi a^3}{(2\ell+1)M_e} h^{L,E}_{\ell}(\omega^n_{\ell m}) L^n_{\ell m} \sin\left(\omega^n_{\ell m} t + \xi'^n_{\ell m}\right) \right] \qquad (48)$$

and

$$\vec{V}_{\ell m}(t) = \sum_{\ell', m'} \left\{ \sum_{n=1}^{N_{\ell' m'}} \left[l^{T,E}_{\ell'}(\omega^n_{\ell' m'}) \frac{W^n_{\ell' m'}}{g} \sin\left(\omega^n_{\ell' m'} t + \xi^n_{\ell' m'}\right) + \frac{4\pi a^3}{(2\ell'+1)M_e} l^{L,E}_{\ell'}(\omega^n_{\ell' m'}) L^n_{\ell' m'} \sin\left(\omega^n_{\ell' m'} t + \xi'^n_{\ell' m'}\right) \right] \right\} \times \vec{D}_{\ell' m' \ell m}. \qquad (49)$$

As a final point in this section, we note that not all surface mass load components are conveniently expressed in terms of expansions of the form (47). One example would be atmospheric pressure loads with near-diurnal or near-annual periods. These periods are sufficiently close to the periods of the free core nutation and Chandler wobble eigenfunctions, respectively, that the Love numbers which characterize the response would be frequency dependent. In these cases the forcing is more conveniently expressed as an integral of periodic terms rather than

as a sum. To consider such a forcing, the summation over n which appears in (47) need only be replaced by an integral over frequency space and (48)–(49) altered accordingly. A second example of a forcing for which the form (47) is not particularly appropriate would be the present-day secular melting of land-based ice sheets and glaciers [*Meier*, 1984]. In this case the formalism outlined in the preceding section (see (40)–(44)) for the response to a surface mass load is most appropriate, with the load Love numbers chosen to reflect the long-period timescale of the forcing. (In this region of frequency space the Love numbers are very weakly dependent on frequency.)

Solving the Sea Level Equation

Equations (48)–(49), together with (40)–(41), provide expressions for the three-dimensional deformation arising from the tidal potential and an arbitrary surface load. Using (10) and the elastic component of the Green's function (18), together with (40) and (48), we can generate an analogous expression for the total gravitational potential perturbation at the deformed solid surface. It is

$$\Phi(\theta,\psi,t) = \sum_{n=1}^{N_{\ell m}} \Phi^n(\theta,\psi,t), \tag{50}$$

where

$$\begin{aligned}\Phi^n(\theta,\psi,t) = \sum_{\ell,m}\Bigg[&\left(1+k_\ell^{T,E}(\omega^n_{\ell m})-h_\ell^{T,E}(\omega^n_{\ell m})\right)\\ &\times W^n_{\ell m}\sin\left(\omega^n_{\ell m}t+\xi^n_{\ell m}\right)\\ &+\frac{4\pi a^3 g}{(2\ell+1)M_e}\left(1+k_\ell^{L,E}(\omega^n_{\ell m})-h_\ell^{L,E}(\omega^n_{\ell m})\right)\\ &\times\Big(L^{n,\mathrm{RES}}_{\ell m}\sin\left(\omega^n_{\ell m}t+\xi''^n_{\ell m}\right)\\ &+L^{n,\mathrm{EO}}_{\ell m}\sin\left(\omega^n_{\ell m}t+\xi'''^n_{\ell m}\right)\Big)\Bigg]Y_{\ell m}(\theta,\psi)\end{aligned} \tag{51}$$

is the nth space-time dependent frequency component of $\Phi(\theta,\psi,t)$. $L^{n,\mathrm{EO}}_{\ell m}$ and $\xi'''^n_{\ell m}$ represent the amplitude and the phase of the nth frequency component of the spherical harmonic coefficient (of degree ℓ and order m) of the equilibrium ocean load. The $L^{n,\mathrm{RES}}_{\ell m}$ and $\xi''^n_{\ell m}$ are analogous terms for the total of the surface mass load contributions other than the equilibrium ocean load. ("RES" denotes the residual surface mass load.) That is, the terms with the superscript RES represent parameters in the expansion (47) of the mass load $L(\theta,\psi,t) - L^{\mathrm{EO}}(\theta,\psi,t)$ (see (39)) and may therefore include contributions from, e.g., atmospheric pressure loads, ice loads, nonequilibrium ocean loads, etc. In this section we assume, regardless of their origin, that these contributions may be prescribed at the outset, and we will be concerned with

a solution for the parameters describing the equilibrium ocean load.

The discussion below will refer to $\Phi^n(\theta,\psi,t)$, rather than to the total perturbation $\Phi(\theta,\psi,t)$. To simplify the expressions used, we define the following quantities:

$$\begin{aligned} W^n_{\ell m}(t) &\equiv W^n_{\ell m}\sin\left(\omega^n_{\ell m}t+\xi^n_{\ell m}\right) \\ L^{n,\mathrm{RES}}_{\ell m}(t) &\equiv L^{n,\mathrm{RES}}_{\ell m}\sin\left(\omega^n_{\ell m}t+\xi''^n_{\ell m}\right) \\ L^{n,\mathrm{EO}}_{\ell m}(t) &\equiv L^{n,\mathrm{EO}}_{\ell m}\sin\left(\omega^n_{\ell m}t+\xi'''^n_{\ell m}\right). \end{aligned} \quad (52)$$

Using Brun's formula [*Heiskanen and Moritz*, 1967], we find that the perturbed position of the equipotential surface (originally located at the undeformed solid surface) with respect to the deformed solid surface, given the gravitational potential perturbation (51), is $\Phi^n(\theta,\psi,t)/g$. This is not, however, the location of the perturbed sea level, or geoidal, surface with respect to the deformed solid surface since that surface is not constrained to remain on the same equipotential. The location of the perturbed geoidal surface with respect to the deformed solid surface can be written as $\Phi^n(\theta,\psi,t)/g+\Delta\Phi^n(t)/g$, where $\Delta\Phi^n(t)$ is a time dependent quantity whose value is constant over the surface of the Earth. The perturbation in the ocean thickness, or bathymetry, is simply the projection of this field onto the region of the Earth covered by oceans.

Let us define the ocean function, $C(\theta,\psi)$, as a field equal to unity over the oceans, and zero elsewhere [*Munk and MacDonald*, 1960], and $C_{\ell m}$ as its set of spherical harmonic coefficients. Let us also define the equilibrium ocean load thickness by $S^{\mathrm{EO}}(\theta,\psi,t)$ and its associated coefficients by $S^{\mathrm{EO}}_{\ell m}(t)$. ($L^{\mathrm{EO}}(\theta,\psi,t)=\rho_w S^{\mathrm{EO}}(\theta,\psi,t)$, $L^{\mathrm{EO}}_{\ell m}(t)=\rho_w S^{\mathrm{EO}}_{\ell m}(t)$, and $L^{n,\mathrm{EO}}_{\ell m}(t)=\rho_w S^{n,\mathrm{EO}}_{\ell m}(t)$, where ρ_w is the density of sea water.) Then, using the arguments above, the equation which governs $S^{n,\mathrm{EO}}_{\ell m}(\theta,\psi,t)$ is

$$\sum_{\ell,m} S^{n,\mathrm{EO}}_{\ell m}(t)Y_{\ell m}(\theta,\psi)=\sum_{r,s}C_{rs}Y_{rs}(\theta,\psi)$$
$$\times\left[\sum_{\ell,m}\left(\frac{\Phi^n_{\ell m}(t)}{g}+\frac{\Delta\Phi^n(t)}{g}\delta_{\ell 0}\delta_{m0}\right)Y_{\ell m}(\theta,\psi)\right], \quad (53)$$

where the $\Phi^n_{\ell m}$ are the coefficients of the spherical harmonic expansion of the total gravitational potential perturbation $\Phi^n(\theta,\psi,t)$. These coefficients are provided in (51). They are

$$\Phi^n_{\ell m}(t)=\left(1+k^{T,E}_\ell(\omega^n_{\ell m})-h^{T,E}_\ell(\omega^n_{\ell m})\right)W^n_{\ell m}(t)$$
$$+\frac{4\pi a^3 g}{(2\ell+1)M_e}\left(1+k^{L,E}_\ell(\omega^n_{\ell m})-h^{L,E}_\ell(\omega^n_{\ell m})\right)$$
$$\times\left(L^{n,\mathrm{RES}}_{\ell m}(t)+\rho_w S^{n,\mathrm{EO}}_{\ell m}(t)\right). \quad (54)$$

Equation (53) is the sea level equation governing the equilibrium ocean load height on a spherically symmetric Earth with an elastic mantle rheology subject to external loading. The equation derives from an integral equation for the sea level response, manifested in the appearance of the coefficients $S_{\ell m}^{n,\mathrm{EO}}(t)$ on both sides of the equation via (54). Physically, this equation reflects the fact that the equilibrium ocean load perturbs the gravitational field of the planet and in turn is governed by this perturbed field, since the geoid is defined to be an equipotential surface.

An expression for the quantity $\Delta\Phi^n(t)$ in (53) may be obtained by imposing a conservation of mass constraint on the equilibrium ocean load. Integrating both sides of (53) over the surface area Ω yields (using the orthogonality property (5), and the fact that $Y_{00} = 1$ in our normalization),

$$\frac{\Delta\Phi^n(t)}{g} = \frac{S_{00}^{n,\mathrm{EO}}(t)}{C_{00}} - \frac{1}{4\pi}\frac{1}{C_{00}} \times \iint_{\Omega} \sum_{r,s} C_{rs} Y_{rs}(\theta,\psi) \sum_{\ell,m} \frac{\Phi_{\ell m}^n(t)}{g} Y_{\ell m}(\theta,\psi)\, d\Omega. \quad (55)$$

One may directly obtain an expression for $S_{00}^{n,\mathrm{EO}}(t)$ by considering all of the surface mass load contributions in (44) which are reflected in the mass balance of the global oceans. For example, if an application were being considered in which only $L^{\mathrm{ICE}}(\theta,\psi,t)$ affected this mass balance, then imposing a conservation of mass yields

$$S_{00}^{n,\mathrm{EO}}(t) = -\frac{1}{\rho_w} L_{00}^{n,\mathrm{ICE}}(t). \quad (56)$$

Dahlen [1976] has provided a purely spectral algorithm for solving a somewhat less general, but essentially equivalent equation of the form of (53). The algorithm involves multiplying (53) by a basis set $Y_{pq}^*(\theta,\psi)$, integrating over Ω, and making use of the orthogonality property (5). The procedure requires the determination of coupling coefficients between sets of surface spherical harmonics, and this severely limits the maximum degree and order (that is, truncation level) which can be feasibly considered. (*Mitrovica and Peltier* [1991a] have argued that a truncation at degree and order near 32 is now the maximum currently feasible.) A hybrid spectral technique is necessary to compute the equilibrium ocean load at the higher resolution required, for example, near continental margins. We outline below a straightforward pseudo-spectral approach which can be applied with high truncation levels. (We have found that consideration of degrees and orders up to 1024 is certainly feasible.)

Let us represent an approximate solution to the equilibrium ocean load height by $\{S_{\ell m}^{n,\mathrm{EO}}(t)\}^i$. We can use (53) iteratively to improve the estimate of $S_{\ell m}^{n,\mathrm{EO}}(t)$ by

substituting $\{S_{\ell m}^{n,\mathrm{EO}}(t)\}^i$ into the right-hand side of the equation. This substitution yields

$$\sum_{\ell,m}\{S_{\ell m}^{n,\mathrm{EO}}(t)\}^{i+1}Y_{\ell m}(\theta,\psi) = C(\theta,\psi) \times\left[\sum_{p,q}\left(\frac{\Phi_{pq}^{i,n}(t)}{g}+\frac{\Delta\Phi^{i,n}(t)}{g}\delta_{p0}\delta_{q0}\right)Y_{pq}(\theta,\psi)\right], \quad (57)$$

where the superscript $i+1$ denotes the improved estimate, and, using (54),

$$\Phi_{pq}^{i,n}(t) = \left[1+k_p^{T,E}(\omega_{pq}^n)-h_p^{T,E}(\omega_{pq}^n)\right]W_{pq}^n(t) + \frac{4\pi a^3 g}{(2p+1)M_e}\left[1+k_p^{L,E}(\omega_{pq}^n)-h_p^{L,E}(\omega_{pq}^n)\right] \times\left(L_{pq}^{n,\mathrm{RES}}(t)+\rho_w\{S_{pq}^{n,\mathrm{EO}}(t)\}^i\right). \quad (58)$$

Let us define

$$\Phi^{i,n}(\theta,\psi,t) = \sum_{p,q}\Phi_{pq}^{i,n}(t)Y_{pq}(\theta,\psi), \quad (59)$$

and, furthermore, the projection of this field onto the ocean regions as

$$\Phi_{\mathrm{OCE}}^{i,n}(\theta,\psi,t) = \Phi^{i,n}(\theta,\psi,t)C(\theta,\psi), \quad (60)$$

which has a spherical harmonic expansion given by

$$\Phi_{\mathrm{OCE}}^{i,n}(\theta,\psi,t) = \sum_{l,m}\left\{\Phi_{\mathrm{OCE}}^{i,n}(t)\right\}_{\ell m}Y_{\ell m}(\theta,\psi). \quad (61)$$

Using (60) and (61) in (57) yields, for each spherical harmonic coefficient,

$$\{S_{\ell m}^{n,\mathrm{EO}}(t)\}^{i+1} = \frac{\left\{\Phi_{\mathrm{OCE}}^{i,n}(t)\right\}_{\ell m}}{g}+\frac{\Delta\Phi^{i,n}(t)}{g}C_{\ell m}. \quad (62)$$

Isolating the degree and order zero term in (62) gives

$$\frac{\Delta\Phi^{i,n}(t)}{g} = \frac{1}{C_{00}}\left[S_{00}^{n,\mathrm{EO}}(t)-\frac{\left\{\Phi_{\mathrm{OCE}}^{i,n}(t)\right\}_{00}}{g}\right]. \quad (63)$$

Equation (63) can also be obtained by applying the improvement procedure to (55). The term $S_{00}^{n,EO}(t)$ does not need to be iteratively improved upon since it can be determined a priori from the spectral coefficients of the appropriate surface mass load contributions (as in (56), for example).

Equations (58)–(63) define the pseudo-spectral algorithm for computing the equilibrium ocean load height on an externally loaded spherically symmetric Earth with an elastic mantle rheology. The procedure begins with an

approximation to the spherical harmonic coefficients of the equilibrium ocean load, $\{S^{n,\mathrm{EO}}_{\ell m}(t)\}^i$. Using (58), the response coefficients $\Phi^{i,n}_{pq}(t)$ can then be determined, and the field $\Phi^{i,n}(\theta,\psi,t)$ of (59) can be synthesized at specific points on a latitude-longitude grid over the Earth's surface, with the grid spacing dependent on the spherical harmonic truncation level. These grid values are then multiplied by the associated value of the ocean function (that is, either 0 or 1; (60)), and the resultant grid decomposed to yield the $\{\Phi^{i,n}_{\mathrm{OCE}}(t)\}_{\ell m}$. These coefficients are used in (63) to determine $\Delta\Phi^{i,n}(t)$ and then, together with this value, in (62) to generate the next, or improved, estimate $\{S^{n,\mathrm{EO}}_{\ell m}(t)\}^{i+1}$. The procedure is termed pseudo-spectral because operations are performed in both the spectral and space domain, which is in contrast to the Galerkin approach of *Dahlen* [1976].

The starting value $\{S^{n,\mathrm{EO}}_{\ell m}(t)\}^{i=1}$ will depend on the particular application of the procedure (see below). As a convergence parameter one may compute

$$\xi^{i+1} = \sum_{\ell,m} \frac{\{S^{n,\mathrm{EO}}_{\ell m}(t)\}^{i+1} - \{S^{n,\mathrm{EO}}_{\ell m}(t)\}^{i}}{\{S^{n,\mathrm{EO}}_{\ell m}(t)\}^{i}}. \qquad (64)$$

We have found, in applications involving a variety of external forcings (including tidal forcings, atmospheric pressure loads and ice loads), that three iterations are sufficient to ensure that $\xi^{i+1} < 10^{-4}$.

The formalism outlined above is related to the pseudo-spectral approach of *Mitrovica and Peltier* [1991a] for computing the gravitationally self-consistent redistribution of ocean mass arising from the melting of late Pleistocene glaciers on a linear viscoelastic Earth model. The procedure described here, however, considers the elastic case and generalizes the formalism to include a gravitational potential forcing as well as a variety of surface mass loads, which may or may not affect the mass balance of the global oceans. The present formalism also incorporates frequency dependent Love numbers.

As derived above, the pseudo-spectral formalism is applied to each frequency component of the external forcing. In the event that a frequency range is being considered within which the Love numbers do not change appreciably, then the formalism can be applied once to generate the response over that frequency range. In this case, the governing equations can be derived by suppressing the frequency dependence of the Love numbers in the equations above, and by considering the "total" (rather than the frequency dependent) harmonics in the specified full frequency range. That is, all terms of the form $\mathcal{L}^n_{\ell m}(t)$ can be replaced by $\mathcal{L}_{\ell m}(t)$, where it is understood that the term $\mathcal{L}_{\ell m}(t)$ is equal to the sum of the $\mathcal{L}^n_{\ell m}(t)$ over the appropriate range of n. The same algorithm is appropriate when considering the equilibrium ocean response

arising from a surface mass and having a time dependence which is secular, rather than periodic, in nature. In this case the Love numbers are chosen as those appropriate to very low frequencies, and the response and load harmonics in the above equations refer to the total fields rather than any specific frequency constituent (or range of constituents).

Below, we briefly consider two special cases of the general formalism outlined above.

Self-Consistent Equilibrium Ocean Tides

Here we consider the equilibrium ocean load height arising solely from the application of a zonal (that is $m = 0$) tidal potential forcing of degree 2. Such a forcing gives rise to the zonal, or long-time scale, body tides [*Melchior*, 1983], and the general equation (4) for the tidal potential can be replaced by

$$W(\theta, \psi, t) = W_{20}(t) Y_{20}(\theta, \psi). \tag{65}$$

Using (46) and (52), we have

$$\begin{aligned} W_{20}(t) &= \sum_{n=1}^{N_{20}} W_{20}^n \sin(\omega_{20}^n t + \xi_{20}^n) \\ &= \sum_{n=1}^{N_{20}} W_{20}^n(t). \end{aligned} \tag{66}$$

In this case, the response coefficients $\Phi_{\ell m}^n(t)$ in the sea level (53), given by (54), are replaced by

$$\begin{aligned} \Phi_{\ell m}^n(t) = &\left(1 + k_\ell^{T,E}(\omega_{\ell m}^n) - h_\ell^{T,E}(\omega_{\ell m}^n)\right) W_{\ell m}^n(t) \delta_{\ell 2} \delta_{m0} \\ &+ \frac{4\pi a^3 g \rho_w}{(2\ell+1) M_e} \left(1 + k_\ell^{L,E}(\omega_{\ell m}^n) - h_\ell^{L,E}(\omega_{\ell m}^n)\right) \\ &\times S_{lm}^{n,\mathrm{EO}}(t). \end{aligned} \tag{67}$$

Equation (58) is changed accordingly. Furthermore, since the mass of the oceans remains constant in this case, $S_{00}^{n,\mathrm{EO}}(t) = 0$ in (55), and (63) becomes

$$\frac{\Delta\Phi^{i,n}(t)}{g} = -\frac{1}{g} \frac{\left\{\Phi_{\mathrm{OCE}}^{i,n}(t)\right\}_{00}}{C_{00}}. \tag{68}$$

The pseudo-spectral formalism proceeds as above (equations (58)–(62) and (68)) and can be initiated using $\{S_{lm}^{n,\mathrm{EO}}(t)\}^{i=1} = 0$.

Self-consistent equilibrium ocean tides induced by a zonal tidal potential have also been considered by *Merriam* [1973, 1980] and *Agnew and Farrell* [1978] in their analysis of the effect of such tides on the length of day. We have compared ocean tide results generated using the pseudo-spectral approach with results presented for a specific W_{20} amplitude by *Agnew and Farrell* [1978, Figure 1] and have found qualitative agreement.

Ocean Redistributions Due to Present-Day Ice Melting

Here we consider the equilibrium ocean mass redistribution arising from the melting of present-day land-based ice sheets and glaciers [*Meier*, 1984]. In this case, (54) and (58) reduce to

$$\Phi_{\ell m}(t) = \frac{4\pi a^3 g}{(2\ell+1)M_e}\left(1 + k_\ell^{L,E} - h_\ell^{L,E}\right) \times \left(\rho_I I_{\ell m}^{\mathrm{ICE}}(t) + \rho_w S_{\ell m}^{\mathrm{EO}}(t)\right) \quad (69)$$

and

$$\Phi_{\ell m}^{i}(t) = \frac{4\pi a^3 g}{(2\ell+1)M_e}\left(1 + k_\ell^{L,E} - h_\ell^{L,E}\right) \times \left(\rho_I I_{\ell m}^{\mathrm{ICE}}(t) + \rho_w \{S_{\ell m}^{\mathrm{EO}}(t)\}^{i}\right), \quad (70)$$

respectively, where ρ_I is the density of ice and where $\rho_I I_{\ell m}^{\mathrm{ICE}}(t) = L_{\ell m}^{\mathrm{ICE}}(t)$. $I_{\ell m}^{\mathrm{ICE}}(t)$ represent the time dependent spherical harmonic coefficients of global ice sheet thickness. Equation (56) thus becomes

$$S_{00}^{\mathrm{EO}}(t) = -\frac{\rho_I}{\rho_w} I_{00}^{\mathrm{ICE}}(t), \quad (71)$$

which can be applied to (63).

A good first guess to the ocean redistribution is the so-called eustatic redistribution. That is,

$$\{S_{lm}^{\mathrm{EO}}(t)\}^{i=1} = -\frac{\rho_I}{\rho_w}\frac{I_{00}^{\mathrm{ICE}}(t)}{C_{00}} C_{lm}. \quad (72)$$

Equation (72) represents the case of meltwater being redistributed in the oceans in a manner independent of geographic location.

As discussed above, in this case, where the time dependence of the surface mass load is secular, rather than periodic, the pseudo-spectral formalism is applied to compute the total response rather than a specific frequency of that response. (The superscript n has been dropped from the equations.) The Love numbers in (69) and (70) refer to those appropriate for a long-period surface loading.

Incorporating an Anelastic Component of Planetary Response

The Love numbers described above were associated with an Earth model having a purely elastic mantle rheology. The effects of mantle anelasticity on the Earth's response to relatively short timescale external forcings can be incorporated into these Love numbers using a straightforward numerical perturbation technique described in detail by *Wahr and Bergen* [1986]. The *Wahr and Bergen* [1986] approach yields complex Love numbers which replace the real coefficients (1)–(3) and (the elastic components of) (11)–(13), reflecting the fact that anelasticity perturbs the amplitude of the Love numbers and

introduces an out-of-phase component (or "lag") in the response.

Let us denote a complex Love number of arbitrary type (i.e., tidal or load, and h, k, or l) and degree as S, where

$$S = S^I + iS^O, \tag{73}$$

and I and O denote the in-phase and out-of-phase components, respectively, of the Love number. Let us also assume an external forcing (that is, an external potential or a surface mass load) of the form $F\cos(\omega t + \phi)$, and let us construct from this a generalized function of the form

$$\mathcal{F} = Fe^{i(\omega t+\phi)}. \tag{74}$$

The response of the planet to the forcing is given by

$$\begin{aligned} \mathcal{R} &= \mathrm{Re}\{S \cdot \mathcal{F}\} \\ &= S^I F\cos(\omega t + \phi) - S^O F\sin(\omega t + \phi), \end{aligned} \tag{75}$$

where Re denotes the real part of the complex quantity. The first term on the right-hand side of (75) is the in-phase component of the response, whereas the second term is the out-of-phase component of the response which arises solely in consequence of anelasticity. S^O can be computed for any particular model for mantle anelasticity using the technique of *Wahr and Bergen* [1986].

The form (75) is introduced to emphasize that the out-of-phase component of the generalized response, the sine term of (75), can be computed using the spectral formalism outlined above for the elastic response. One needs only to replace the external forcing terms by their out-of-phase analogues and the Love numbers by their imaginary components. The spectral calculations of three-dimensional crustal deformations, equilibrium sea level variations, etc., then proceeds in entirely the same fashion.

For external forcings on longer timescales (for example, the surface mass load associated with the melting of the late Pleistocene ice sheets), the nonelastic behavior of the planet is evident in a viscoelastic response of the planet [e.g., *Cathles,* 1971; *Peltier,* 1974]. In this case it is appropriate to consider a viscoelastic formalism for the Earth's response, as we do below.

Response to an Arbitrary Surface Load of a Spherically Symmetric Earth with a Viscoelastic Mantle Rheology

In this section we consider three-dimensional deformations associated with the surface loading of a spherically symmetric Earth having a linear viscoelastic mantle rheology. In this case we need only consider the response (32)

and (33) with the appropriate Green's functions. Using (12) and (15) in (32), with B_ℓ defined as in (26), yields

$$U(\theta,\psi,t) = \sum_{\ell,m}\left[\frac{4\pi a^3}{(2\ell+1)M_e}\left(L_{\ell m}(t)h_\ell^{L,E} + \sum_{k=1}^{K(\ell)} r1_k^{L,\ell}\beta_{\ell m}^k(t)\right)\right] \times Y_{\ell m}(\theta,\psi) \quad (76)$$

and

$$\vec{V}(\theta,\psi,t) = \sum_{\ell,m}\left[\frac{4\pi a^3}{(2\ell+1)M_e}\left(L_{\ell m}(t)l_\ell^{L,E} + \sum_{k=1}^{K(\ell)} r2_k^{L,\ell}\beta_{\ell m}^k(t)\right)\right] \times \vec{\nabla} Y_{\ell m}(\theta,\psi), \quad (77)$$

where

$$\beta_{\ell m}^k(t) = \int_{-\infty}^{t} L_{\ell m}(t')\exp\left[-s_k^\ell(t-t')\right]\,dt'. \quad (78)$$

The first terms in large parentheses on the right-hand sides of (76) and (77) represent the purely elastic components of the response, whereas the second terms represent the nonelastic response.

Predictions of present-day three-dimensional deformations associated with the melting of the massive late Pleistocene ice sheets represent an obvious application of the above theory. It has been common to model the time dependence of these ice sheets as a series of step-load increments [*Farrell and Clark*, 1976; *Wu and Peltier*, 1983]. This representation incurs no loss of generality since the time steps may be made arbitrarily small. If we apply the same discretization to our general surface load $L(\theta,\psi,t)$, we can write

$$\begin{aligned} L(\theta,\psi,t) &= \sum_{n=1}^{N}\delta L^n(\theta,\psi)H(t-t_n) \\ &= \sum_{n=1}^{N}\sum_{\ell,m}\delta L_{\ell m}^n Y_{\ell m}(\theta,\psi)H(t-t_n), \end{aligned} \quad (79)$$

where H represents the Heaviside step function and N is the total number of step load increments. Comparing (79) with (24) gives

$$L_{\ell m}(t) = \sum_{n=1}^{N}\delta L_{\ell m}^n H(t-t_n). \quad (80)$$

The form of (80) allows for an analytic evaluation of the integral in (78). Applying this form to (76) and (77)

yields, using (36), response equations of the form (40)–(41) with spherical harmonic coefficients given by

$$U_{\ell m}(t) = \frac{4\pi a^3}{(2\ell+1)M_e}\left(L_{\ell m}(t) h_\ell^{L,E} + \sum_{k=1}^{K(\ell)} \sum_{n=1}^{N(t)} \delta L_{\ell m}^n \frac{r1_k^{L,\ell}}{s_k^\ell} \left(1 - \exp\left[-s_k^\ell (t-t_n)\right]\right)\right) \quad (81)$$

and

$$\vec{V}_{\ell m}(t) = \sum_{\ell',m'} \left\{ \frac{4\pi a^3}{(2\ell'+1)M_e}\left(L_{\ell' m'}(t) l_{\ell'}^{L,E} + \sum_{k=1}^{K(\ell')} \sum_{n=1}^{N(t)} \delta L_{\ell' m'}^n \frac{r2_k^{L,\ell'}}{s_k^{\ell'}} \left(1 - \exp\left[-s_k^{\ell'} (t-t_n)\right]\right)\right)\right\} \times \vec{D}_{\ell' m' \ell m}. \quad (82)$$

The summations over n include all the load increments which have a time onset prior to the observation time t. That is, $N(t)$ represents the number of load increments, in the total of N, which satisfy $t_n \leq t$.

As above the surface mass load appearing in (81)–(82) can include contributions from a number of different geophysical loading phenomena acting on a broad range of timescales (see (39)). Following (39) and (44) we can separate the load into a contribution from a gravitationally self-consistent equilibrium ocean load and a residual ("RES") surface load which includes all other surface load contributions. That is, we can write

$$L_{\ell m}(t) = \rho_w S_{\ell m}^{\mathrm{EO}}(t) + L_{\ell m}^{\mathrm{RES}}(t) \quad (83)$$

and

$$\delta L_{\ell m}^n = \rho_w \delta S_{\ell m}^{n,\mathrm{EO}} + \delta L_{\ell m}^{n,\mathrm{RES}}, \quad (84)$$

where the $S_{\ell m}^{\mathrm{EO}}(t)$ are the spherical harmonic coefficients of the equilibrium ocean load height and the $\delta S_{\ell m}^{n,\mathrm{EO}}$ are the associated coefficients for the nth incremental change, as expressed in (80).

Mitrovica and Peltier [1991a] have outlined both a spectral and a pseudo-spectral formalism for computing gravitationally self-consistent equilibrium ocean load height increments associated with the surface loading of a spherically symmetric Earth with a viscoelastic mantle rheology. Both algorithms output the spherical harmonic coefficients of the equilibrium ocean load height (or sea level) increments, $\delta S_{\ell m}^{n,\mathrm{EO}}$ and are thus ideally suited (as a preliminary step) to the spectral formalism outlined here for computing the three-dimensional deformations associated with an arbitrary surface load.

Present-Day Deformations Associated With the Melting of the Late Pleistocene Ice Sheet

Predictions of present-day deformations associated with the melting of the late Pleistocene ice sheets can be based upon applications of (81)–(82) using quite specific forms for (83) and (84). These forms are

$$L_{\ell m}(t) = \rho_w S^{\rm EO}_{\ell m}(t) + \rho_I I^{\rm ICE}_{\ell m}(t) \tag{85}$$

and

$$\delta L^n_{\ell m} = \rho_w \delta S^{n,{\rm EO}}_{\ell m} + \rho_I \delta I^{n,{\rm ICE}}_{\ell m}, \tag{86}$$

where $I^{\rm ICE}_{\ell m}(t)$ are the spherical harmonic coefficients of the late Pleistocene ice sheet thickness, and $\delta I^{n,{\rm ICE}}_{\ell m}$ are the associated coefficients for the n^{th} incremental change (as expressed in (80)) in ice thickness. The coefficients for $I^{\rm ICE}_{\ell m}(t)$ and $\delta I^{n,{\rm ICE}}_{\ell m}$ can be generated from published late Pleistocene ice thickness reconstructions [e.g., *Tushingham and Peltier,* 1991], while the $S^{\rm EO}_{\ell m}(t)$ and $\delta S^{n,{\rm EO}}_{\ell m}$ can be determined using the pseudo-spectral algorithm developed by *Mitrovica and Peltier* [1991a].

Perturbations in the Center of Mass of the Deformed Planet: A Spectral Approach

Let us use the term "planet" to include the Earth model, whose undeformed state is used in the calculation of the Love numbers, but not in the calculation of the surface mass load. In this section we derive, using a spectral formalism, an expression for the perturbation in the center of mass of the planet, relative to the center of mass of the undeformed state, which arises as a consequence of a surface mass loading.

Cathles [1971] has recognized that the center of mass of the planet can be perturbed in the surface mass load problem, since the load may have a nonzero spherical harmonic degree one forcing. We will presume in this section that no other external forces (e.g., tidal) are acting on the system. Accordingly, perturbations in the center of mass of the planet and surface load are related by

$$\Delta \vec{r}^{\,\rm CM}_e = -\frac{M_{\rm SL}}{M_e} \Delta \vec{r}^{\,\rm CM}_{\rm SL}, \tag{87}$$

where $\vec{r}^{\,\rm CM}$ denotes vectors measured relative to the unperturbed center of mass of the system, e and SL denote the planet and surface load, respectively, $M_{\rm SL}$ is the mass of the surface load, and Δ denotes a perturbation. Since the surface load conserves mass, we can write

$$\Delta \vec{r}^{\,\rm CM}_{\rm SL} = \frac{1}{M_{\rm SL}} \iiint_V \Delta\varrho(r,\theta,\psi)\ \vec{r}\ dv, \tag{88}$$

where $\Delta\varrho$ is the position dependent density perturbation in the surface mass load and the integration is performed

over the volume of the load. The confinement of the surface mass load to a thin surface layer allows us to write

$$\Delta\varrho(r,\theta,\psi) = \Delta\sigma(\theta,\psi)\ \delta(r-a), \tag{89}$$

where δ is the delta function and $\Delta\sigma$ is the perturbation in the surface mass load, in units of mass per area in accord with our definition of the surface load used in previous sections. Using (89) in (88) yields

$$\Delta\vec{r}_{\rm SL}^{\rm CM} = \frac{a^3}{M_{\rm SL}} \iint_{\Omega} \Delta\sigma(\theta,\psi)\ \hat{r}\ \sin\theta\ d\theta\ d\psi, \tag{90}$$

where $\hat{r}$ is the unit radial vector. If we denote the spherical harmonic coefficients of the surface mass load perturbation $\Delta\sigma(\theta,\psi)$ by $\Delta\sigma_{\ell m}$, then the surface integration in (90) can be shown to be

$$\iint_{\Omega} \Delta\sigma(\theta,\psi)\ \hat{r}\ \sin\theta\ d\theta\ d\psi = \frac{4\pi}{\sqrt{3}} \sum_{m=-1}^{1} \hat{e}_m\ \Delta\sigma_{1m}, \tag{91}$$

where the $\hat{e}_m$ are the polarization unit vectors defined by *Edmonds* [1960] and given in the appendix, and $\Delta\sigma_{1m}$ are the coefficients in the spherical harmonic expansion of the surface mass load. Combining (87), (90), and (91) yields

$$\Delta\vec{r}_e^{\rm CM} = -\frac{4\pi a^3}{M_e\sqrt{3}} \sum_{m=-1}^{1} \hat{e}_m\ \Delta\sigma_{1m}. \tag{92}$$

If, instead of deformations, we are interested in deformation rates, then we can write

$$\Delta\dot{\vec{r}}_e^{\rm CM} = -\frac{4\pi a^3}{M_e\sqrt{3}} \sum_{m=-1}^{1} \hat{e}_m\ \Delta\dot{\sigma}_{1m}, \tag{93}$$

where the $\Delta\dot{\sigma}_{1m}$ are the degree one coefficients in the spherical harmonic expansion of the time rate of change of the surface mass load. The vector components of the center of mass perturbations given by (92) and (93) are, using the polarization unit vectors listed in the appendix, referenced to the geocentric Cartesian coordinate system.

The Love numbers for an Earth model are computed so that the Earth response generated from them is referred to an origin at the center of mass of the undeformed planet [*Farrell*, 1972]. Thus positions computed using the spectral response equations derived above will be referenced to this origin. Equations (92) and (93) provide the perturbation (or the rigid translation) of the center of mass of the deformed planet with respect to its undeformed state, and they may therefore be used in an a posteriori calculation to reference any computed changes in position to an origin at the center of mass of the deformed planet. In other words, (92) and (93) may be

used to remove the component of pure translation associated with position changes computed in reference to an origin at the center of mass of the undeformed planet. The positions thus corrected are more accurately termed "deformations."

Summary

We have outlined a complete spectral formalism for computing three-dimensional deformations of a spherically symmetric Earth due to an arbitrary surface mass loading. The appropriate spectral response equations have been derived for the case of Earth models with elastic, anelastic, and viscoelastic mantle rheologies. Methodologies required for computing the Love numbers appropriate for such Earth models are found in the literature; the required references are *Farrell* [1972], *Wahr and Bergen* [1986], and *Peltier* [1974, 1985], respectively. In the case of an elastic or anelastic mantle rheology, we have incorporated frequency dependent Love numbers into the formulation and have derived a pseudo-spectral algorithm for determining the ocean mass redistribution arising from the gravitational perturbation associated with the external loading. As a consequence of their definition, response predictions based on tidal and surface load Love numbers are generally referenced to an origin located at the center of mass of the undeformed planet. Coordinate position changes may thus incorporate a pure translation associated with the perturbation of the center of mass of the deformed planet from its location in the unperturbed state. Accordingly, we have derived a spectral formula for translating the origin to the center of mass of the deformed planet, and the position changes thus "corrected" are more accurately interpreted as "deformations."

In order to test numerical codes established to apply the theory described herein, we have compared our predictions of three-dimensional crustal deformations with published results based on the Green's function approach described in the introduction. Those tests indicate that the spectral formalism can be easily applied to spherical harmonic truncation levels in excess of degree 2048 using existing computer systems.

In a companion article [*Mitrovica et al.*, this issue] we generate predictions, up to degree 512, of present-day three-dimensional deformations associated with the glacial isostatic adjustment process. The deformation predictions are based on the spectral response equations derived above, and they incorporate both gravitationally self-consistent ocean redistributions (using the pseudo-spectral algorithm of *Mitrovica and Peltier* [1991a]) and realistic models of the space-time deglaciation history of the late Pleistocene ice sheets.

Appendix: An Analytic Form for $\vec{\nabla}\mathbf{Y}_{\ell\mathbf{m}}(\theta,\psi)$

Forte and Peltier [1994] have derived the following identity for $\vec{\nabla}Y_{\ell m}(\theta,\psi)$ where the two-dimensional gradient operator $\vec{\nabla}$ is defined as in (9) and the surface spherical harmonics are normalized as in (5):

$$\vec{\nabla}Y_{\ell m}(\theta,\psi) =$$
$$\frac{\hat{e}_{-1}}{\sqrt{2}}\left[Y_{\ell+1,m+1}(\theta,\psi)\ \ell\ \left(\frac{(\ell+m+2)(\ell+m+1)}{(2\ell+1)(2\ell+3)}\right)^{\frac{1}{2}}\right.$$
$$\left.+\,Y_{\ell-1,m+1}(\theta,\psi)\ (\ell+1)\ \left(\frac{(\ell-m-1)(\ell-m)}{(2\ell+1)(2\ell-1)}\right)^{\frac{1}{2}}\right]$$
$$-\,\hat{e}_0\left[Y_{\ell+1,m}(\theta,\psi)\ \ell\ \left(\frac{(\ell-m+1)(\ell+m+1)}{(2\ell+1)(2\ell+3)}\right)^{\frac{1}{2}}\right.$$
$$\left.-\,Y_{\ell-1,m}(\theta,\psi)\ (\ell+1)\ \left(\frac{(\ell-m)(\ell+m)}{(2\ell+1)(2\ell-1)}\right)^{\frac{1}{2}}\right]$$
$$+\,\frac{\hat{e}_1}{\sqrt{2}}\left[Y_{\ell+1,m-1}(\theta,\psi)\ \ell\ \left(\frac{(\ell-m+1)(\ell-m+2)}{(2\ell+1)(2\ell+3)}\right)^{\frac{1}{2}}\right.$$
$$\left.+\,Y_{\ell-1,m-1}(\theta,\psi)\ (\ell+1)\ \left(\frac{(\ell+m-1)(\ell+m)}{(2\ell+1)(2\ell-1)}\right)^{\frac{1}{2}}\right] \quad \text{(A1)}$$

where $\hat{e}_{-1}$, $\hat{e}_0$, and $\hat{e}_1$ are the polarization unit vectors defined by *Edmonds* [1960] as

$$\hat{e}_{-1} = \frac{1}{\sqrt{2}}(\hat{x} - i\hat{y}) \quad \text{(A2)}$$

$$\hat{e}_0 = \hat{z} \quad \text{(A3)}$$

and

$$\hat{e}_1 = -\frac{1}{\sqrt{2}}(\hat{x} + i\hat{y}). \quad \text{(A4)}$$

The vectors $\hat{x}$, $\hat{y}$ and $\hat{z}$ represent the basis unit vectors in the geocentric Cartesian coordinate system. The vector $\vec{\nabla}Y_{\ell m}(\theta,\psi)$ can, of course, also be written in the form

$$\vec{\nabla}Y_{\ell m}(\theta,\psi) = \hat{x}X + \hat{y}Y + \hat{z}Z, \quad \text{(A5)}$$

where the components X, Y, and Z can be determined by substitution of (A2)–(A4) into (A1). It will be useful to generalize (A1) by writing it as

$$\vec{\nabla}Y_{\ell m}(\theta,\psi) = \sum_{\ell'=0}^{\infty}\sum_{m'=-\ell'}^{\ell'} \vec{D}_{\ell m\ell' m'}Y_{\ell' m'}(\theta,\psi). \quad \text{(A6)}$$

In order to express $\vec{\nabla}Y_{\ell m}(\theta,\psi)$ in terms of a particular basis set, it is necessary only to determine the vector coefficients $\vec{D}_{\ell m\ell' m'}$, which, using (A1)–(A4), amounts

to determining expressions for the basis set of interest in terms of the $(\hat{e}_{-1}, \hat{e}_0, \hat{e}_1)$ or the $(\hat{x}, \hat{y}, \hat{z})$. It is clear from (A1) that, for a given ℓ, m pair, only a very small number of $\vec{D}_{\ell m \ell' m'}$ are nonzero.

The surface spherical harmonics $Y_{\ell m}(\theta, \psi)$ have the following property:

$$Y_{\ell,-m}(\theta, \psi) = (-1)^m Y^*_{\ell m}(\theta, \psi), \tag{A7}$$

where the asterisk denotes the complex conjugate. One can show, using (A7) in (A1)–(A4), that the vector components of $\vec{\nabla} Y_{\ell m}(\theta, \psi)$ have the analogous property:

$$\vec{\nabla} Y_{\ell,-m}(\theta, \psi) = (-1)^m \left[\vec{\nabla} Y_{\ell m}(\theta, \psi)\right]^*. \tag{A8}$$

Let us consider a vector $\vec{T}(\theta, \psi)$ defined such that

$$\vec{T}(\theta, \psi) = \sum_{\ell=0}^{\infty} \sum_{m=-\ell}^{\ell} T_{\ell m} \vec{\nabla} Y_{\ell m}(\theta, \psi). \tag{A9}$$

If the components of $\vec{T}(\theta, \psi)$ are real, then one can show, using (A8), that

$$T^*_{\ell,-m} = (-1)^m T_{\ell m}, \tag{A10}$$

and that the summation (A9) may be written as

$$\vec{T}(\theta, \psi) = \sum_{\ell=0}^{\infty} \sum_{m=1}^{\ell} 2\mathrm{Re}\left[T_{\ell m} \vec{\nabla} Y_{\ell m}(\theta, \phi)\right] + \sum_{\ell=0}^{\infty} T_{\ell 0} \vec{\nabla} Y_{\ell 0}(\theta, \phi), \tag{A11}$$

where Re denotes the real part of the complex quantity.

Acknowledgments. We would like to thank P.M. Mathews and A.M. Forte for their valuable advice regarding this manuscript, as well as John Wahr, Paul Morgan, and an anonymous reviewer, for their constructive comments. This work was supported in part by a Natural Sciences and Engineering Research Council of Canada research grant (J.X.M.), NASA grant NAG5-1930, and the Smithsonian Institution.

References

Agnew, D.C., and W.E. Farrell, Self-consistent equilibrium ocean tides, *Geophys. J. R. Astron. Soc.*, *55*, 171–181, 1978.

Biot, M.A., Theory of stress-strain relations in anisotropic visco-elasticity and relaxation phenomena, *J. Appl. Phys.*, *25*, 1385–1391, 1954.

Broecker, W.S., and J. Van Donk, Insolation changes, ice volumes, and the O^{18} record in deep sea cores, *Rev. Geophys.*, *8*, 169–198, 1970.

Cartwright, D.E. and A.C. Edden, Corrected tables of tidal harmonics, *Geophys. J. R. Astron. Soc.*, *33*, 253–264, 1973.

Cartwright, D.E. and R.S. Tayler, New computations of the tide-generating potential, *Geophys. J. R. Astron. Soc.*, *23*, 45–74, 1971.

Cathles, L.M., The viscosity of the Earth's mantle, Ph.D. thesis, Princeton Univ., Princeton, 1971.

Christodoulidis, D.C., D.E. Smith, R.E. Williamson, and S.M. Klosko, Observed tidal breaking in the Earth/Moon/ Sun system, *J. Geophys. Res.*, *93*, 6216–6236, 1988.

Clark, J.A., W.E. Farrell and W R. Peltier, Global changes in postglacial sea level: A numerical calculation, *Quat. Res.*, *9*, 265–287, 1978.

Dahlen, F.A., The passive influence of the oceans upon the rotation of the Earth, *Geophys. J. R. Astron. Soc.*, *46*, 363–406, 1976.

Dickman, S.R., A complete spherical harmonic approach to luni-solar tides, *Geophys. J. Int.*, *99*, 457–468, 1989.

Edmonds, A.R., *Angular Momentum in Quantum Mechanics*, 2nd edition, Princeton University Press, Princeton, 1960.

Farrell, W.E., Deformation of the Earth by surface loads, *Rev. Geophys.*, *10*, 761–797, 1972.

Farrell, W.E., and J.A. Clark, On postglacial sea level, *Geophys. J. R. Astron. Soc.*, *46*, 647–667, 1976.

Forte, A.M., and W.R. Peltier, The kinematics and dynamics of poloidal-toroidal coupling in mantle flow: The importance of surface plates and lateral viscosity variations, *Adv. in Geophys.*, in press, 1994.

Francis, O., and V. Dehant, Recomputation of the Green's functions for tidal loading estimations, *Bull. Inf. Marees Terr.*, *100*, 6962–6986, 1987.

Goad, C.C., Gravimetric tidal loading computed from integrated Green's functions, *J. Geophys. Res.*, *85*, 2679–2683, 1980.

Heiskanen, W.A., and H. Moritz, *Physical Geodesy*, Freeman, Cooper, San Fransisco, Calif., 1967.

Jackson, *Classical Electrodynamics*, Wiley, New York, 848 pp., 1975.

James, T.S., and W.J. Morgan, Horizontal motions due to postglacial rebound, *Geophys. Res. Lett.*, *17*, 957–960, 1990.

James, T.S., and A. Lambert, A comparison of VLBI data with the ICE-3G glacial rebound model, *Geophys. Res. Lett.*, *20*, 871–874, 1993.

Jentzcsh, G., The influence of grid structure on the results of loading calculations, *Bull. Inf. Marees Terr.*, *94*, 6382-6368, 1985.

Longman, I.M., A Green's function for determining the deformation of the Earth under surface mass loads, 1, Theory, *J. Geophys. Res.*, *67*, 845–850, 1962.

Longman, I.M., A Green's function for determining the de-

formation of the Earth under surface mass loads, 2, Computations and numerical results, *J. Geophys. Res.*, *68*, 485–496, 1963.

Love, A.E.H., The yielding of the Earth to disturbing forces, *Proc. R. Soc., London*, *82*, 73–88, 1909.

Meier, M.F., Contribution of small glaciers to global sea level, *Science*, *26*, 1418–1421, 1984.

Melchior, P., *The Tides of the Planet Earth*, Pergamon, New York, 1983.

Merriam, J.B., *Equilibrium Tidal Response of a Non-global Self-gravitating Ocean on a Yielding Earth*, M.Sc. thesis, Mem. Univ. of Newfoundland, St. John's, 1973.

Merriam, J.B., Zonal tides and changes in the length of day, *Geophys. J. R. Astron. Soc.*, *62*, 551–556, 1980.

Mitrovica, J.X., and W.R. Peltier, Pleistocene deglaciation and the global gravity field, *J. Geophys. Res.*, *94*, 13,651–13,671, 1989.

Mitrovica, J.X., and W.R. Peltier, On post-glacial geoid relaxation over the equatorial oceans, *J. Geophys. Res.*, *96*, 20,053–20,071, 1991a.

Mitrovica, J.X., and W.R. Peltier, A complete formalism for the inversion of post-glacial rebound data: Resolving power analysis, *Geophys. J. Int.*, *104*, 267–288, 1991b.

Mitrovica, J.X., J.L. Davis, and I.I. Shapiro, A spectral formalism for computing three-dimensional deformations due to surface loads, 2, Present-day glacial isostatic adjustment, *J. Geophys. Res.*, this issue.

Müller, T., and W. Zürn, Observation of gravity changes during the passage of cold fronts, *J. Geophys.*, *53*, 155–162, 1983.

Munk, W.H., and G.J.F. MacDonald, *The Rotation of the Earth*, Cambridge University Press, London, 1960.

Nakada, M., and K. Lambeck, Glacial rebound and relative sea level variations: A new appraisal, *Geophys. J. R. Astron. Soc.*, *90*, 171–224, 1987.

Pagiatakis, S.D., The response of a realistic Earth to ocean tide loading, *Geophys. J. Int.*, *103*, 541–560, 1990.

Peltier, W.R., The impulse response of a Maxwell Earth, *Rev. Geophys.*, *12*, 649–669, 1974.

Peltier, W.R., Glacial isostatic adjustment, II, The inverse problem, *Geophys. J. R. Astron. Soc.*, *46*, 669–706, 1976.

Peltier, W.R., The LAGEOS constraint on deep mantle viscosity: Results from a new normal mode method for the inversion of viscoelastic relaxation spectra, *J. Geophys. Res.*, *90*, 9411–9421, 1985.

Peltier, W.R., and J.T. Andrews, Glacial isostatic adjustment, I, The forward problem, *Geophys. J. R. Astron. Soc.*, *46*, 605–646, 1976.

Peltier, W.R., W.E. Farrell, and J.A. Clark, Glacial isostasy and relative sea level: A global finite element model, *Tectonophysics*, *51*, 81–110, 1978.

Pertsev, B.P., On the effects of ocean tides on tidal variations of gravity, *Izv. Acad. Sci. USSR Phys. Solid Earth*, *10*, 25–29, 1966.

Rabbel, W., and J. Zschau, Static deformations and gravity changes at the Earth's surface due to atmospheric loading, *J. Geophys.*, *56*, 81–99, 1985.

Scherneck, H.-G., A parametrized solid Earth tide model and ocean tide loading effects for global geodetic baseline measurements, *Geophys. J. Int.*, *106*, 677–694, 1991.

Schwiderski, E.W., Global ocean tides, I, A detailed hydrodynamical interpolation model, Nav. Surface Weapons

Cent., Dahlgren, Va., 1978.
Shackleton, N.J., Oxygen isotope analyses and Pleistocene temperatures re-addressed, *Nature*, *215*, 15–17, 1967.
Shida, T., and M. Matsuyama, Note on Hecker's observations of horizontal pendulums, *Memoirs of the College of Science and Engineering, Kyoto Imperial Univ.*, *4*, 187–224, 1912.
Spada, G., R. Sabadini, D.A. Yuen, and Y. Ricard, Effects on post-glacial rebound from the hard rheology in the transition zone, *Geophys. J. Int.*, *109*, 683–700, 1992.
Trenberth, K.E., Seasonal variations in global sea level pressure and the total mass of the atmosphere, *J. Geophys. Res.*, *86*, 5238–5246, 1981.
Tushingham, A.M., Potential effects of ongoing postglacial adjustment on very long baseline interferometry measurements, *Geophys. Res. Lett.*, *18*, 1281–1284, 1991.
Tushingham, A.M., and W.R. Peltier, ICE-3G: A new global model of late Pleistocene deglaciation based upon geophysical predictions of postglacial relative sea level change, *J. Geophys. Res.*, *96*, 4497–4523, 1991.
van Dam, T.M., and J M. Wahr, Displacements of the earth's surface due to atmospheric loading: Effects on gravity and baseline results, *J. Geophys. Res.*, *92*, 1281–1286, 1987.
van Dam, T. M., Atmospheric Loading Response of the Solid Earth and Oceans, Ph.D. thesis, 135 pp., Univ. of Colo., Boulder, 1991.
Wahr, J.M., A normal mode expansion for the forced response of a rotating Earth, *Geophys. J. R. Astron. Soc.*, *64*, 651–675, 1981a.
Wahr, J.M., Body tides on an elliptical, rotating, elastic and oceanless Earth, *Geophys. J. R. Astron. Soc.*, *64*, 677–703, 1981b.
Wahr, J.M., and Z. Bergen, The effects of mantle anelasticity on nutations, Earth tides, and tidal variations in rotation rate, *Geophys. J. R. Astron. Soc.*, *87*, 633–668, 1986.
Wang, R., Das viskelastiche Verhalten der Erde auf langfristige Gezeitenterme, diploma thesis, Mat.-Nat. Fak., Univ. Kiel, 1986.
Wu, P., and W.R. Peltier, Glacial isostatic adjustment and the free air gravity anomaly as a constraint on deep mantle viscosity, *Geophys. J. R. Astron. Soc.*, *74*, 377–450, 1983.
Zwally, H.J., Growth of Greenland ice sheet: Interpretation, *Science*, *246*, 1589–1591, 1989.

J. L. Davis and I. I. Shapiro, Harvard-Smithsonian Center for Astrophysics, 60 Garden Street, Cambridge, MA 02138 (e-mail: jdavis@cfa.harvard.edu; shapiro@cfa.harvard.edu).
J. X. Mitrovica, Department of Physics, University of Toronto, 60 St. George Street, Toronto, Ontario, Canada, M5S 1A7 (e-mail: jxm@physics.utoronto.ca).

(Received April 29, 1993; revised October 19, 1993;
accepted October 29, 1993.)

MITROVICA ET AL.: SPECTRAL THEORY FOR THREE-DIMENSIONAL DEFORMATIONS

MITROVICA ET AL.: SPECTRAL THEORY FOR THREE-DIMENSIONAL DEFORMATIONS
MITROVICA ET AL.: SPECTRAL THEORY FOR THREE-DIMENSIONAL DEFORMATIONS
MITROVICA ET AL.: SPECTRAL THEORY FOR THREE-DIMENSIONAL DEFORMATIONS
MITROVICA ET AL.: SPECTRAL THEORY FOR THREE-DIMENSIONAL DEFORMATIONS
MITROVICA ET AL.: SPECTRAL THEORY FOR THREE-DIMENSIONAL DEFORMATIONS
MITROVICA ET AL.: SPECTRAL THEORY FOR THREE-DIMENSIONAL DEFORMATIONS
MITROVICA ET AL.: SPECTRAL THEORY FOR THREE-DIMENSIONAL DEFORMATIONS
MITROVICA ET AL.: SPECTRAL THEORY FOR THREE-DIMENSIONAL DEFORMATIONS
MITROVICA ET AL.: SPECTRAL THEORY FOR THREE-DIMENSIONAL DEFORMATIONS
MITROVICA ET AL.: SPECTRAL THEORY FOR THREE-DIMENSIONAL DEFORMATIONS
MITROVICA ET AL.: SPECTRAL THEORY FOR THREE-DIMENSIONAL DEFORMATIONS
MITROVICA ET AL.: SPECTRAL THEORY FOR THREE-DIMENSIONAL DEFORMATIONS
MITROVICA ET AL.: SPECTRAL THEORY FOR THREE-DIMENSIONAL DEFORMATIONS
MITROVICA ET AL.: SPECTRAL THEORY FOR THREE-DIMENSIONAL DEFORMATIONS
MITROVICA ET AL.: SPECTRAL THEORY FOR THREE-DIMENSIONAL DEFORMATIONS
MITROVICA ET AL.: SPECTRAL THEORY FOR THREE-DIMENSIONAL DEFORMATIONS
MITROVICA ET AL.: SPECTRAL THEORY FOR THREE-DIMENSIONAL DEFORMATIONS
MITROVICA ET AL.: SPECTRAL THEORY FOR THREE-DIMENSIONAL DEFORMATIONS
MITROVICA ET AL.: SPECTRAL THEORY FOR THREE-DIMENSIONAL DEFORMATIONS
MITROVICA ET AL.: SPECTRAL THEORY FOR THREE-DIMENSIONAL DEFORMATIONS
MITROVICA ET AL.: SPECTRAL THEORY FOR THREE-DIMENSIONAL DEFORMATIONS
MITROVICA ET AL.: SPECTRAL THEORY FOR THREE-DIMENSIONAL DEFORMATIONS
MITROVICA ET AL.: SPECTRAL THEORY FOR THREE-DIMENSIONAL DEFORMATIONS
MITROVICA ET AL.: SPECTRAL THEORY FOR THREE-DIMENSIONAL DEFORMATIONS
MITROVICA ET AL.: SPECTRAL THEORY FOR THREE-DIMENSIONAL DEFORMATIONS
MITROVICA ET AL.: SPECTRAL THEORY FOR THREE-DIMENSIONAL DEFORMATIONS
MITROVICA ET AL.: SPECTRAL THEORY FOR THREE-DIMENSIONAL DEFORMATIONS
MITROVICA ET AL.: SPECTRAL THEORY FOR THREE-DIMENSIONAL DEFORMATIONS
MITROVICA ET AL.: SPECTRAL THEORY FOR THREE-DIMENSIONAL DEFORMATIONS
MITROVICA ET AL.: SPECTRAL THEORY FOR THREE-DIMENSIONAL DEFORMATIONS
MITROVICA ET AL.: SPECTRAL THEORY FOR THREE-DIMENSIONAL DEFORMATIONS

MITROVICA ET AL.: SPECTRAL THEORY FOR THREE-DIMENSIONAL DEFORMATIONS
MITROVICA ET AL.: SPECTRAL THEORY FOR THREE-DIMENSIONAL DEFORMATIONS
MITROVICA ET AL.: SPECTRAL THEORY FOR THREE-DIMENSIONAL DEFORMATIONS
MITROVICA ET AL.: SPECTRAL THEORY FOR THREE-DIMENSIONAL DEFORMATIONS

N15

AGU JGR galley style, v3.0, 29 Oct 93

A spectral formalism for computing three-dimensional deformations due to surface loads
2. Present-day glacial isostatic adjustment

J. X. Mitrovica
Department of Physics, University of Toronto, Toronto, Ontario, Canada

J. L. Davis and I. I. Shapiro
Harvard-Smithsonian Center for Astrophysics, Cambridge, Massachusetts

Abstract. Using a spherically symmetric, self-gravitating, linear viscoelastic Earth model, we predict present-day three-dimensional surface deformation rates and baseline evolutions arising as a consequence of the late Pleistocene glacial cycles. In general, we use realistic models for the space-time geometry of the final late Pleistocene deglaciation event and incorporate a gravitationally self-consistent ocean meltwater redistribution. The predictions of horizontal velocity presented herein differ significantly, in both their amplitude and their spatial variation, from those presented in an earlier analysis of others which adopted simplified models of both the late Pleistocene ice history and the Earth rheology. An important characteristic of our predicted velocity fields is that the melting of the Laurentide ice sheet over Canada is capable of contributing appreciably to the adjustment in Europe. The sensitivity of the predictions to variations in mantle rheology is investigated by considering a number of different Earth models, and by computing appropriate Frechet kernels. These calculations suggest that the sensitivity of the deformations to the Earth's rheology is significant and strongly dependent on the location of the site relative to the ancient ice sheet. The effects on the predictions of three-dimensional deformation rates of altering the ice history or adopting approximate models for the ocean meltwater redistribution have also been considered and found to be important (the former especially so). Finally, for a suite of Earth models we provide predictions of the velocity of a number of baselines in North America and Europe. We find that, in general, both radial and tangential motions contribute significantly to baseline length changes, and that these contributions are a strong function of the Earth model. We have, furthermore, found a set of Earth models which, together with the ICE-3G deglaciation chronology, produce predictions of baseline length changes that are consistent with very long baseline interferometry measurements of baselines within Europe.

Introduction

The last late Pleistocene deglaciation event of the current ice age was sufficiently massive and recent that the Earth remains in a state of appreciable isostatic disequilibrium. This disequilibrium is manifest in a variety of geophysical observables, but none more direct

Paper number 93JB03401.
0148-0227/94/93JB-03401$05.00

than the associated three-dimensional crustal deformations and velocities. In this regard, radial deformations have received the most consideration, mainly because of their important contribution to apparent sea level variations in both the near field and the far field of the late Pleistocene ice sheets [*Cathles*, 1975; *Peltier*, 1986; *Mitrovica and Peltier*, 1991]. In spite of this interest, however, a number of fundamental questions regarding radial crustal deformations remain unanswered. In particular, changes in the depth-dependent sensitivity of the radial velocity field to variations in the mantle viscosity profile, as one proceeds from sites in the near field of the late Pleistocene ice sheets, through the peripheral bulge, and on to the far field, has not been investigated. A small set of forward calculations, based on spherically symmetric Earth models having isoviscous upper and lower mantle regions [e.g., *Cathles*, 1975; *Peltier*, 1986], suggests that these changes must be significant.

The study of *James and Morgan* [1990] represents the first to consider horizontal motions associated with the glacial isostatic adjustment phenomenon. *James and Morgan* [1990] considered, in particular, present-day horizontal deformations and velocities arising from the melting of a Laurentide scale ice sheet; their analysis included a number of significant approximations. The Laurentide ice sheet was modeled as a single ice disk having a fixed basal radius and a mass which varied, in time, with a simple saw-tooth pattern. The Earth model adopted in the calculations was characterized by a five-layer, incompressible rheology. The tangential velocity profiles computed by *James and Morgan* [1990] were characterized by a broad region, extending from the center of the ice sheet to well into the far field, in which tangential motions were directed inward (i.e., toward the disk center). A recent investigation by *James and Lambert* [1993] suggests that the *James and Morgan* [1990] predictions do not closely approximate those obtained using more realistic models of the late Pleistocene surface mass load and the Earth's rheology.

Current and future space geodetic measurements of relative three-dimensional crustal deformation rates are, and will continue to be, of sufficient accuracy to require a comprehensive examination of present-day three-dimensional deformation rates associated with the glacial isostatic adjustment phenomenon. This paper provides such an analysis. As a preliminary, we examine predictions generated using simplified disk models of the late Pleistocene ice sheets, our goal being to isolate some of the basic characteristics and sensitivities of the postglacial velocity field. Our main predictions will, however, be based on a surface mass load composed of more realistic ice and ocean load components.

The sensitivity of the predictions to the radial profile of mantle viscosity will be examined by using a suite of

forward calculations and by computing Frechet kernels. In particular, we compute the kernels for predictions of present-day radial and tangential velocities at a number of sites in North America and Fennoscandia which are chosen to sample the near, intermediate, and far field glacial isostatic adjustment process. In general, the calculations will be performed by adopting the ICE-3G model of the late Pleistocene deglaciation event; however, we consider the sensitivity of the forward predictions to variations in the ice model.

Finally, we also present predictions of the evolution of a number of North American and European baselines included in a recent analysis of Mark III geodetic very long baseline interferometry (VLBI) data [*Ryan et al.*, 1993]. We have several goals: (1) to obtain values for the potential range of signals in the baseline evolution from the glacial isostatic adjustment process, (2) to consider the sensitivity of the predictions to variations in the mantle viscosity profile, (3) to investigate the relative contributions to the components of the evolution associated with radial and tangential motions of the sites defining the baselines, and (4) to use the predictions to investigate whether the VLBI-determined European baseline rates may be fit by deformations associated with any of a number of "reasonable" combinations of ice history and Earth rheology.

Results

Mitrovica et al. [this issue] outline a spectral formalism for computing three-dimensional deformation rates on a spherically symmetric, self-gravitating, Maxwell viscoelastic planetary model due to an arbitrary surface load. We have adopted this formalism to predict glacial isostatic adjustment rates using a truncation at spherical harmonic degree and order 512. The redistribution of mass in the global oceans, when it is incorporated in the loading calculations, is computed using the gravitationally self-consistent pseudo-spectral algorithm of *Mitrovica and Peltier* [1991]. In the following two sections we consider the three components of velocity in the local cartesian reference frame, $\dot{U}_\psi$ (local east), $\dot{U}_\theta$ (local south), and $\dot{U}_r$ (local up, or radial). The three-dimensional baseline velocity vectors described in the final section are expressed in terms of components in an Earth-centered baseline-oriented coordinate system defined by the baseline component axes. The three baseline component axes are defined by the unit vectors $\hat{l}$ ("length"), $\hat{t}$ ("transverse"), and $\hat{v}$ ("vertical"), specified by

$$\begin{aligned} \hat{l} &= \frac{\vec{r}_2 - \vec{r}_1}{|\vec{r}_2 - \vec{r}_1|} \\ \hat{t} &= \frac{\vec{r}_2 \times \vec{r}_1}{|\vec{r}_2 \times \vec{r}_1|} \\ \hat{v} &= \hat{l} \times \hat{t} \end{aligned} \tag{1}$$

where $\vec{r}_1$ and $\vec{r}_2$ are the a priori site position vectors. The length, transverse, and vertical velocity components will often be referred to below as L, T, and V, respectively. Radial site motions contribute only to the L and V components of baseline changes, whereas tangential motions will contribute to all three components.

The numerical algorithm used to determine Frechet kernels is described by *Mitrovica and Peltier* [1993a]. These kernels relate arbitrary perturbations in the radial viscosity profile to the consequent perturbation in a particular observable. If we denote the observable by U, and its perturbation by δU, then these kernels, which we denote by $F(\nu(r), r)$, are defined via the following relationship:

$$\delta U = \int_{r_{\rm CMB}}^{1} F(\nu(r), r)\ \delta \log \nu(r)\ dr \tag{2}$$

where r denotes the nondimensional radius (i.e., normalized by the radius of the Earth), $\nu(r)$ is the radial viscosity profile, and $r_{\rm CMB}$ is the (normalized) radius of the core-mantle boundary (CMB).

Finally, all calculations will use an Earth model characterized by an elastic structure given by the seismically determined Preliminary Reference Earth Model (PREM) [*Dziewonski and Anderson*, 1981], an inviscid core, an elastic lithosphere (of thickness denoted by LT), and isoviscous upper and lower mantle regions (with viscosities denoted by ν_{UM} and ν_{LM}, respectively).

Calculations Using Simplified Disk Load Models

In this section we present calculations of present-day three-dimensional deformation rates obtained using two simplified models of ice loading. No ocean load will be included. The ice models consist of single disks having parabolic vertical cross section and circular horizontal cross section. At glacial maximum the two disks have basal radii of 16° and 8° and provide a rough approximation to the maximum geographic extent of the Laurentide and Fennoscandian ice sheets, respectively. The time dependence of the disk mass is a simple sawtooth function with a 90-kyr growth phase followed immediately by a 10-kyr deglaciation phase. Within each cycle the radius and height of the ice disk are varied in order to maintain plastic equilibrium [*Paterson*, 1981]. The final deglaciation event for the ice disk models will be assumed

to have ended 6 kyr B.P. The Fennoscandian ice sheet disappeared earlier than this date; however, we will be most concerned in this section with isolating the influence of the horizontal scale of the ice sheet on the numerical predictions. The maximum height of the ice disk is chosen to yield a peak present-day uplift rate of 10 mm yr^{-1} when we use the "test" Earth model described below.

In Figure 1 we show results obtained using the two ice disk models and a suite of Earth models. In this and subsequent sections we will refer to a "test" Earth model. This model is defined by LT = 120 km, $\nu_{UM} = 10^{21}$ Pa s, and $\nu_{LM} = 2 \times 10^{21}$ Pa s and has been proposed by *Tushingham and Peltier* [1992] on the basis of an analysis of a globally distributed database of relative sea level (RSL) curves. The Earth models considered on Figure 1 include the test model and others identical to it except that one of either LT, ν_{UM}, or ν_{LM} has been varied.

To begin, let us consider the results for the Laurentide scale ice sheet. As is well known, the radial velocity field is characterized by a region of uplift, or rebound, over the bulk of the previously glaciated region, encircled by a peripheral region undergoing subsidence. The pattern of radial motions associated with the deglaciation is relatively insensitive to variations in lithospheric thickness. Within the central region the uplift rates diminish as either ν_{LM} or ν_{UM} is reduced: a reduction in the viscosity (over the range considered in Figure 1) leads to Earth models with shorter characteristic relaxation times; hence these models will have adjusted, by the present, to a state closer to their final equilibrium position. As ν_{LM} is increased, the position of maximum subsidence within the peripheral bulge migrates away from the previously glaciated region. Within the bulge region the most pronounced effect of increasing ν_{UM} is to increase the subsidence rate.

Next, consider the tangential velocity profile associated with the test model. In the region extending from the center of the now vanished disk to the location of maximum present-day peripheral subsidence rate, the tangential velocities are directed away from the disk center. Beyond this central region the "test" profile indicates a very extensive region in which the tangential velocity is directed toward the previously glaciated region. Indeed, one must move approximately 70° from the disk load center before the amplitude of this negative velocity component is reduced by 50% of its peak value of -0.3 mm yr^{-1}. This result suggests that the melting of the Laurentide ice sheet has the potential to produce appreciable present-day tangential velocities in regions as distant as Fennoscandia (displaced only about 45° from Hudson Bay) and, indeed, well beyond.

The tangential velocity field is sensitive to variations in the lithospheric thickness. The velocity profile essentially shifts downward as LT is reduced. This shift arises, in part, as a consequence of differences in the response

of the lithosphere to shear stresses acting at the base of the region. The net effect of these shear stresses is a motion of the lithosphere toward the center of the previously glaciated region. (This motion is not evident at all locations in Figure 1 because of obscuring contributions to tangential motion from other mechanisms.) The thinner the lithosphere, the less the resistance to the stress field, and thus the higher the tangential velocity toward the center of the disk which is contributed by the basal shear. As ν_{LM} is increased to 5×10^{21} Pa s, the outward horizontal speeds in the central region are increased. In the far field of the disk center, beyond the main peripheral bulge region, the computed tangential velocity (directed toward the disk center) increases significantly in amplitude as the lower mantle is stiffened. The net effect is that relative tangential velocities along the computed profiles are particularly sensitive to variations in ν_{LM}. In contrast, the relative tangential velocities are insensitive to variations in LT. Finally, reducing ν_{UM} leads to a significantly broader region in which present-day tangential velocities are directed away from the center of the disk. Indeed, for the Earth model with $\nu_{UM} = 3 \times 10^{20}$ Pa s, positive tangential velocities extend to a point over 50° from the disk center, compared to the corresponding value of 16° for the test model.

Comparing the results of Figures 1a and 1b with those obtained using the disk load of maximum radius 8° indicates that present-day deformation rates of significant magnitudes become more concentrated in the central region as the length scale of the ice disk is decreased. In the case of the test Earth model and the 16° disk load the maximum tangential velocities away from and toward the disk center are approximately 0.6 and 0.3 mm yr^{-1}, respectively, and the maximum peripheral subsidence is 1.6 mm yr^{-1}. The corresponding values for the 8° disk load are 1.0, 0.1, and 1.0 mm yr^{-1}. This result indicates that the deglaciation event over Fennoscandia will not have a significant impact on the present-day tangential velocity field over, say, North America.

The computed present-day tangential velocities are less sensitive to variations in the lithospheric thickness in the case of the 8° disk load than they are in the case of the 16° disk load. In contrast, the computed radial velocity results show greater sensitivity to variations in LT as the length scale of the surface mass load is reduced. The sensitivity of the computed velocities to variations in ν_{LM} is much less pronounced for the Fennoscandia scale ice sheet since the smaller disk is obviously less efficient in driving lower mantle flow than the larger.

James and Morgan [1990] have computed tangential deformation rates using a fixed-radius disk load model of the ancient Laurentide ice sheet, a simplified ocean load (extending from 65° to the antipole of the disk), and a small number of Earth models. The radial dependencies

of the elastic parameters in their Earth models were discretized using only five layers, and the model was assumed to be elastically incompressible. One consequence of their discretization is that the density jump at 670 km depth was 1100 kg m^{-3}, which is almost 3 times the PREM derived value. The assumption of elastic incompressibility is also rather suspect, and, accordingly, we have performed calculations, using our Laurentide scale ice disk, which explicitly consider this aspect of the *James and Morgan* [1990] models. The solid and dashed lines on Figure 2 were obtained using the test Earth model; however, in the latter case the Earth is assumed to be elastically incompressible. Clearly, the errors incurred by assuming an incompressible elastic response, in calculations of present-day tangential velocities, can be very large. These errors, for the case of the test model, exceed 50% in the central region and 35% in the periphery. The errors are smaller in the computed peak central uplift rates (about 5%); however, they reach 20% in predictions of the peak peripheral subsidence.

James and Morgan [1990] adopted assumptions which lead to features in their computed tangential deformation rates that are significantly different from those obtained in the present analysis. For example, the tangential velocity profiles computed by *James and Morgan* [1990, Figure 4] do not generally exhibit motion away from the center of the ice disk, within the central region, which is characteristic of all of the Earth models considered in this section. Indeed, the dominant characteristic of the profiles computed by *James and Morgan* [1990] is a broad, high-amplitude, region of negative (i.e., toward the disk center) velocity which extends from the load center to a position near 70° from this point. The peak amplitude of the negative tangential velocities they obtained ranged between -2.5 and -4.2 mm yr^{-1}. (The peak uplift rates for the same models were 1.1–1.5 mm yr^{-1}.) These tangential rates are substantially larger in magnitude than the negative velocities presented in this section, regardless of the Earth model used, even taking into account the slightly higher radial uplift rates. Indeed, our own test calculations (not shown here) using the ice disk of maximum radius 16° and *James and Morgan's* [1990] "reference" Earth model, predicted a tangential velocity profile with a maximum positive velocity of approximately 1.0 mm yr^{-1} and a peak negative velocity of -0.5 mm yr^{-1}. We conclude that the very large tangential deformation rates directed toward the disk center and the absence of central regions of substantial outward tangential motions, which characterize the *James and Morgan* [1990] results, are artifacts of the simplifications adopted in that study. (The calculations performed in subsequent sections of this paper support this conclusion.) The assumption of a time-independent ice disk radius (in addition to that of elastic incompressibility) is particularly suspect, and no doubt

has a profound influence on the profile of tangential velocity, especially near the maximum perimeter of the ice disk. *James and Lambert* [1993] have recently suggested that the adoption of an incompressible lithosphere in the study of *James and Morgan* [1990] was responsible for the prediction of inwardly directed tangential velocities in the near field. The results in Figure 2 suggest that other assumptions adopted by *James and Morgan* [1990] must also contribute significantly in this regard.

Calculations Using Realistic Ice Models: Three Dimensional Deformation Rates

In Figure 3 we show maps of the predicted present-day radial and tangential velocity fields over North America and Europe generated using the test Earth model. The surface mass load incorporated a gravitationally self-consistent ocean meltwater component and the ICE-3G model for the final late Pleistocene deglaciation event [*Tushingham and Peltier*, 1991]. (Independently derived maps, based on the same load and Earth model, were recently published by *James and Lambert* [1993].) The ICE-3G model has been adapted in order to incorporate three full glacial cycles [*Mitrovica and Peltier*, 1993a]. In North America, peak radial velocities are obtained on the east coast of James Bay (approximately 13 mm yr^{-1}) and also near the west coast of Hudson Bay. These locations coincide with the two areas in which the (ICE-3G model) Laurentide ice sheet thickness exceeded 3 km during the last glacial maximum. The main uplift region extends over all of Canada and a portion of northeastern United States. The secondary uplift peak over the west coast of Canada is associated with the disappearance of the Cordilleran ice sheet, whereas the deflection of the uplift contours toward the north is due to the melting of Arctic ice. The peak uplift rate over the main Fennoscandian deglaciation center reaches in excess of 12 mm yr^{-1}. Other regions of uplift are associated with melting over Spitzbergen (Svalbard), the Barents and Kara Seas, Iceland, Greenland, and the northern tip of the British Isles. Encircling the main regions of uplift are the subsiding peripheral bulges. In general, the North American subsidence rates are somewhat higher than those in Europe, as one would expect from the disk load calculations. Significantly, there are several areas in which the subsidence rates exceed a few millimeters per year, and these coincide with locations at the periphery of more than one ice sheet. Examples are the Davis Strait/Baffin Bay region and northwest of Fennoscandia, both of which have subsidence rates which reach $\sim$5 mm yr^{-1}.

The combination of the ICE-3G ice history and the test Earth model has produced peak uplift and subsidence rates over North America and Fennoscandia which are comparable, even though the ice sheet which covered the latter was much smaller and melted away much faster

than the Laurentide ice sheet. The reason for this near equality is that the characteristic decay time associated with the response of the test Earth model increases as the spatial scale of the load is reduced (to a limit of about 700 km). Thus the smaller Fennoscandian ice sheet will maintain a relatively greater level of present-day disequilibrium.

Next, consider the tangential velocity fields. Any area which is characterized by a local peak in the radial velocity field, that is a deglaciation center, is subject to relatively small tangential deformation rates and encircled by a region in which the tangential motion is directed outward (as in Figure 1). In North America the pattern is evident near the southern tip of James Bay, in Labrador, off the western edge of Hudson Bay, and in the Canadian Cordillera. Maximum tangential motions of just over 2.0 mm yr^{-1} are obtained on the northeast coast of Labrador, and rates of 1.5 mm yr^{-1} are evident on Baffin Island. In Europe this pattern exists over the Gulf of Bothnia, the Barents and Kara seas, Iceland, Greenland, and the northern reaches of the United Kingdom. The peak tangential motions reach $\sim$2 mm yr^{-1} on the coast of Norway and in the Norwegian Sea. Comparable tangential velocities are also predicted on the western edge of the Barents Sea, in the vicinity of Spitzbergen. Encircling the whole of Canada, and to the south of the previously glaciated areas in Europe, are broad regions in which the tangential deformation rates are directed toward the associated uplifting regions. These rates are $\sim$0.5 mm yr^{-1} in the former region and only slightly less in the latter. These amplitudes are significantly larger (approximately a factor of two or more) than those recently presented by *James and Lambert* [1993] using an identical Earth model along with the ICE-3G deglaciation event. The origin of these differences is not known.

As observed in Figure 1, the melting episode over Laurentia produces, for predictions based on the test Earth model, an appreciable tangential adjustment at very large angular distances from Hudson Bay. For the European region considered in Figure 3, this contribution should be characterized by a roughly uniform tangential motion toward the northwest. Thus the tangential motions predicted for continental Europe ($\sim$0.4 mm yr^{-1} to the northwest) arise from the adjustment associated with both the local melting events and the melting over Laurentia. Indeed, the disk calculations indicate that velocities of this amplitude could not arise solely from the melting of the ice sheets in northern Europe. As a final point in this regard, the Fennoscandian adjustment associated with the local melting event will tend to be reinforced, on the northwest side, by the contribution from the Laurentide melting episode, and partially cancelled on the southeast side for the same reason. As a consequence, Norway is experiencing relatively large tangential defor-

mation rates of $\sim$2 mm yr^{-1}, whereas tangential rates in Finland and the Baltic Sea (directed to the southeast) are about 40% smaller than this value.

The predicted tangential motions shown in Figure 3 are a complicated superposition of adjustments associated with a number of ice domes. For example, the corridor formed by the proglacial system extending from Great Bear Lake to Lake Winnipeg is characterized by rather weak tangential motions because the eastward and westward motions associated with the melting of the Cordilleran and Laurentian ice sheets, respectively, almost cancel each other. A similar cancellation is evident in Baffin Bay and Davis Strait. In the latter case, large gradients ($\sim$3 mm yr^{-1} across a distance of only $\sim$500 km) occur in the predicted tangential velocity field.

In the investigations described below we often focus on predictions of velocity components along two specific great circle profiles; the first extends from Fort Rupert, just west of James Bay, to Richmond, Florida; the second extends from Luleå, Sweden to Wettzell, Germany (see Figure 3). Fort Rupert and Luleå are near areas of peak uplift, while both Richmond and Wettzell are in the far field, well south of regions of maximum peripheral subsidence. Figure 4 (solid lines) provides the velocity components along these profiles for the calculations given in Figure 3. (The $\dot{U}_\psi$ values along the Fort Rupert-Richmond profile are close to zero because the profile is oriented nearly north-south, and the ancient Laurentide ice sheet was roughly symmetrical across it. This result does not apply to the European profile since that profile is neither an approximate symmetry axis for the uplifting Fennoscandian region, nor is it oriented north-south.)

We now investigate the sensitivity of the results in Figures 3 and 4 (solid lines) to variations in both the surface mass load and the Earth model. Figure 5 shows predictions (analogous to those presented on Figure 3) generated using an ice load adapted, as described above, from the ICE-1 deglaciation history [*Peltier and Andrews*, 1976]. Comparing Figures 3 and 5, we see a marked similarity in the general form of the radial and tangential velocity fields predicted on the basis of the two ice models. (As we have observed the same is not necessarily true of predictions based on Earth models with different mantle viscosity profiles.) Important differences are, however, apparent. For example, the peak uplift rates over Hudson Bay and Fennoscandia are larger (by about 20%) for predictions based on the ICE-1 model. In the case of the ICE-1 results the region of peak uplift in Canada extends east-west over a broad area which encompasses southern Hudson Bay (and which is somewhat north of the peak uplift, at Fort Rupert, on Figure 3). Furthermore, in Fennoscandia, the major axis of the uplift field predicted using the ICE-1 model is, in contrast to Figure 3, aligned roughly parallel to the Baltic Sea and the Luleå–Wettzell

profile. These differences, due to variations in the ice sheet geometry, are also evident on the tangential velocity maps. In the case of predictions generated using the ICE-1 model the central region in which tangential velocities are very small (and from which the velocity vectors emanate outward) is located slightly northward (~300 km) in the Hudson Bay region and slightly southward (~200 km) in the Baltic Sea area of the corresponding locations for the ICE-3G predictions. Differences between Figures 3 and 5 are also significant over Greenland, where the ICE-1 model adopts a relatively insignificant deglaciation event, and over the Arctic region north of Europe. In the latter area the ICE-3G model includes a Barents Sea ice complex, whereas the ICE-1 history does not.

The velocity components along the Fort Rupert to Richmond and Luleå to Wettzell profiles, generated using the ICE-1 and ICE-3G models (Figure 4), reflect the variations described above. (Notice, for example, the relative shift between the U_θ component of velocity computed using the two ice models; the slight oscillation evident in the velocity profiles computed using the ICE-1 model is due to the very coarse spatial discretization which characterizes that model; see *Peltier and Andrews* [1976].) The results indicate that predictions of three-dimensional velocities at specific geographic sites are sensitive to variations in the ice mass history. This sensitivity may not be surprising since we have already observed (in the context of Figure 3) that velocity predictions at a particular site are strongly dependent on the location of the site relative to the spatial geometry of the ice load. (The location of the two great circle profiles was based on an inspection of the ICE-3G based results in Figure 3.) Clearly, analyses based on a comparison of predicted three-dimensional velocities with observational constraints (for example, to infer mantle rheology) must recognize this sensitivity.

In Figure 6 we investigate the sensitivity of the predictions in Figure 3 to errors in the ocean loading model. The solid lines denote velocity components generated using a gravitationally self-consistent ocean load. The dashed and dotted lines represent results generated using simplified models of the ocean mass redistribution. The dashed line is computed by adopting the so-called eustatic approximation. That is, it is assumed that the ocean mass load, which complements the mass fluctuation in the late Pleistocene ice sheets, is independent of position [e.g., *Mitrovica and Peltier,* 1991]. The dotted lines represent results generated by assuming no ocean load component.

We conclude that radial velocities can be computed accurately using the eustatic approximation, except in regions within, or in the vicinity of, oceans. The largest errors in the Fort Rupert-Richmond profile (~0.5 mm yr^{-1}) occur at the edges of the profile, that is, in the vicinity of Hudson Bay and the Atlantic Ocean. Even more pro-

nounced errors ($\sim$2.0 mm yr^{-1}) are evident on the first 1000 km of the profile between Luleå and Wettzell, which skirts and sometimes enters the western coasts of the Gulf of Bothnia and the Baltic Sea. These errors are due to the neglect of hydroisostatic effects. In a gravitationally self-consistent calculation of the ocean redistribution the on-going removal of ocean mass in the region of post-glacial uplift, as a consequence of this uplift, represents a continuously increasing negative mass load on the system. This load will tend to increase the present-day radial velocity in the region and its vicinity. The eustatic approximation does not incorporate this effect since, in this case, the ocean load at any particular time represents some globally averaged distribution of the complement of the total ice mass. Indeed, since the ICE-3G deglaciation event ends at 5 kyr B.P., the eustatic approximation implies no change in the ocean load subsequent to this time.

The influence of hydroisostasy on the computed present-day tangential velocities is not insignificant. Along the profiles the amplitude of the error which results from using the eustatic approximation can be as large as 0.1–0.2 mm yr^{-1}, with the peak obtained at the point of maximum tangential speed on the profiles ($\sim$1 mm yr^{-1}). The sign of the error is opposite for the two profiles. For the Fort Rupert to Richmond profiles, hydroisostatic effects diminish the tangential speed by as much as 0.1 mm yr^{-1} in this region ($\sim$500 km south of Fort Rupert), while the same effects add approximately 0.2 mm yr^{-1} to the tangential speed of the 750 km point on the Luleå-Wettzell profile. The reason for this difference is that the position of the ocean load relative to the profile is different in the two cases. The 500-km point on the Fort Rupert to Richmond profile is well outside the Hudson Bay area. Therefore a negative mass load on Hudson Bay will tend to produce (using the test Earth model) an incremental tangential motion toward Hudson Bay. The 750-km point on the Luleå to Wettzell profile is, in contrast, essentially in the very midst of the ocean load. Thus the negative mass load will produce incremental tangential velocities away from the region.

Assumptions made concerning the modeling of the ocean load are important when considering tangential velocities associated with specific coastal sites (see Figure 7). At some coastal sites the eustatic approximation is accurate (e.g., sites 5–7, on the east coast of the United States), whereas at some others (e.g., site 16, Helsinki) it is no more accurate than the assumption of no ocean load. The errors incurred using either a nonexistent or gravitationally inconsistent ocean load component are evident in both the amplitude and direction of the predicted tangential motions.

In Figure 8 we consider results generated by varying the lithospheric thickness of the test model. The con-

clusions based upon the simple disk load calculations are valid for the interpretation of the sensitivities evident on Figure 8. For example, the computed radial velocity profiles in Fennoscandia are more sensitive to variations in LT than are the corresponding North American profiles. The effect of increasing LT on the computed radial velocity profiles is to reduce the present-day peak uplift and subsidence rates. Indeed, the peak relative radial velocities on the European and North American profiles are reduced, respectively, by 3.5 and 1.5 mm yr^{-1}, as LT is increased from 96 to 145 km. Increasing the lithospheric thickness tends to smooth the three-dimensional velocity profiles. Increasing LT also results in a relatively uniform positive perturbation in the tangential velocity field. Relative tangential velocities are clearly not strongly affected by variations in LT.

In Figures 9 and 10 we consider the sensitivity of the three-dimensional velocity predictions to variations of ν_{LM} and ν_{UM}, respectively. As in Figure 1, increasing ν_{LM} leads to an increase in the peak present-day uplift rate and an outward migration of the position of maximum subsidence on the peripheral bulge. Decreasing ν_{UM} results in predictions with lower peak uplift and subsidence rates. Since the ice sheet which existed over Laurentia was much larger than that which existed over Fennoscandia, the computed radial uplift rates along the Fort Rupert-Richmond profile tend to be more sensitive to variations in ν_{LM} and less sensitive to variations in ν_{UM} than are the uplift rates for Luleå-Wettzell.

It is difficult to compare directly the tangential velocity profiles of Figures 9 and 10 with corresponding results obtained using simplified disk load models. The realistic ICE-3G ice sheets exhibit profound asymmetries, both on local and global length scales. As a result, the specific profiles we are considering may be affected in a complicated manner; certainly, the profiles are not constrained to have zero tangential velocities at their starting points. Furthermore, the influence of asymmetries in the surface mass load on the computed profiles will be model dependent since tangential motions are sensitive to variations in the Earth model characteristics, even at great distances from the load. Similarities between the tangential velocity predictions shown in Figures 9 and 10, and the corresponding predictions from disk load models, are more obvious when one considers relative tangential velocities.

Figure 11 shows the present-day values for $\dot{U}_\theta$ along each of the Fort Rupert–Richmond and Luleå–Wettzell profiles relative to the rate at the starting point of each, for the Earth models considered in Figure 9. Increasing ν_{LM} produces an increase in the (relative) outward tangential velocity in the near field and, in the case of the larger ice sheet, a significant increase in the (relative) tangential velocity toward the previously glaciated area in the far field. (In the case of $\nu_{LM} = 10^{21}$ Pa s, Rich-

mond is, in contrast to the test Earth model results, predicted to be moving away from the previously glaciated region.) The relative tangential velocities in the far field for the European profiles exhibit only weak sensitivity to variations in ν_{LM}, whereas the absolute velocities (Figure 9b) are much more sensitive to these variations. This difference is due to the adjustment in Fennoscandia, associated with the melting of the Laurentide ice sheet, being sensitive to variations in ν_{LM}.

The adjustment due to Laurentide deglaciation must also be influencing the tangential velocity results in Figure 10b, in which the sensitivity to variations in ν_{UM} of the computed profiles is explored. However, this influence is not as apparent in Figure 10b, as it was in Figure 9b, mainly because the adjustment associated with the melting of the (local) Fennoscandian ice complex is also sensitive to variations in ν_{UM}. Relative tangential velocities along the profiles of Figure 10b arise mainly from local melting events. Once again, an important observation is that a reduction in ν_{UM} leads to a significant enlargement of the region characterized by tangential motions directed outward toward the far field.

To gain insight into the sensitivity of a particular observable to the detailed radial variation of rheology requires the calculation of Frechet kernels (equation (2)). Frechet kernels for predictions of present-day three-dimensional deformation rates at nine different sites on both the Fort Rupert-Richmond and Luleå-Wettzell profiles are shown on Figure 12. The kernels were computed using the test Earth model, the ICE-3G adapted ice history, and a gravitationally self-consistent ocean load.

Consider the kernels for site A, situated at Fort Rupert, which is near the location of maximum uplift rate. The kernel for the radial velocity indicates that the velocity has a nonnegligible sensitivity to variations in viscosity at depths extending down to the CMB, although the maximum sensitivity is clearly located in the top half of the lower mantle and in the upper mantle. This suggests that the sensitivity of the predictions of $\dot{U}_r$ at Fort Rupert to variations in ν_{LM} (Figure 9a) should be ascribed mainly to a sensitivity to variations in rheology above 1600 km depth. In contrast, the sensitivity of the same radial velocity prediction to variations in ν_{UM} (see Figure 10a) reflects a sensitivity which is more or less constant over the entire upper mantle region. The ratio of the area under the radial velocity kernel for Fort Rupert in the lower mantle to the corresponding area in the upper mantle is approximately 2:1. This ratio remains relatively constant for the sites B and C, which are also situated in the central uplift region of Laurentia. Indeed, the main difference in the radial velocity kernels as one moves from site A to site C is a progressive and rather uniform reduction in amplitude. This indicates that radial velocity data obtained at such sites will not provide independent

information regarding the mantle viscosity profile.

The $\dot{U}_\theta$ kernels indicate that the predicted $\dot{U}_\theta$ values for sites A–C are much less sensitive to variations in the rheology of the lower mantle than to variations in the rheology of the upper mantle. (See also Figures 9 and 10.) Indeed, the sensitivity to variations in viscosity within the lower mantle is limited to the very shallowest portions of this region. Furthermore, a comparison of these kernels with those for the radial velocity predictions indicates that uplift rate data from central regions will provide substantially more information regarding deep mantle rheology than tangential velocity data from the same area.

The Frechet kernels in Figure 12, sites D–I, suggest that the detailed depth-dependent sensitivity of the three-dimensional velocity components varies significantly as one moves from the edge of the uplift region, through the peripheral bulge, and on to the far field. Three-dimensional velocity data obtained from each of these regions will provide independent constraints on the radial profile of mantle viscosity.

As one proceeds from a site just inside the edge of the uplift region (site C), to one just outside the edge (site D), the radial velocity kernels continue to trend toward less positive values. This trend is most evident in the shallowest regions of the mantle, and it leads, for site D, to negative values of the kernel within the upper mantle. This suggests that at some point between the sites C and D, near the very edge of the predicted uplift region, the area under the associated $\dot{U}_r$ kernel in the upper mantle will vanish. Thus the radial velocity computed at this point using the test Earth model should be insensitive to variations in ν_{UM}. This location coincides with the "hinge point," 900 km from Fort Rupert, in the bottom frame of Figure 10a. The radial velocity kernel in Figure 12, site D, indicates that the $\dot{U}_r$ prediction at site D using the test Earth model will have a nearly uniform sensitivity to variations in viscosity anywhere in the lower mantle. Thus the migration of the perimeter of the uplift region, observed in numerical studies of glacial isostatic adjustment in North America in which ν_{LM} is varied [e.g., *Cathles,* 1975; *Peltier and Andrews,* 1976], is sensitive to variations in the rheology of the entire lower mantle.

Continuing from outside the edge of the uplift region (site D) to a point somewhat beyond the location of maximum peripheral subsidence rate (site E), the emergence of negative values on the radial velocity kernels continues and extends through the top half of the lower mantle. Within this range of sites the prediction of radial velocity becomes increasingly sensitive to variations in the upper mantle viscosity. Between sites D and E the Frechet kernel in the lower mantle evolves from being nearly uniform and positive to being mostly negative and peaking at the top of the region. At some point between sites D and E,

but closer to site E and, very close to the position of maximum subsidence on the peripheral bulge, the area under the radial velocity kernels in the lower mantle vanishes. As one proceeds from site E through to the outer flank of the peripheral bulge (site F) and then on to the far-field (sites G–I), the region exhibiting the peak sensitivity to variations in rheology migrates to greater depths in the mantle. In the outer regions of the peripheral bulge (sites E to F) the predicted radial velocity is similarly sensitive to variations in the viscosity of the top half of the lower mantle and in the viscosity of the upper mantle. In the far field, however, the predictions are almost totally insensitive to variations in viscosity anywhere in the upper mantle. The sensitivity of the radial velocity prediction at Richmond to variations in ν_{LM}, evident in the bottom frame of Figure 9a, may be ascribed to a sensitivity which peaks in the lower mantle between depths of 800 and 2200 km.

The change in the radial velocity kernels between sites D and I provides a detailed picture of the sensitivity of the dynamics of the peripheral bulge to variations in lower mantle rheology. The predicted migration of the peripheral bulge with variations in ν_{LM} is a consequence of the reversal in the area under the radial velocity kernels, within the lower mantle, as one proceeds from sites on the near field side of the point of maximum peripheral subsidence (site D) to sites on the far-field side of that point (sites E–G). The reversal is associated with significant changes in the sensitivity of the predicted radial velocity to variations of rheology at the top of the lower mantle, as one moves along the profile. This evolving sensitivity produces a "twisting" of the predicted profile, within the periphery, as ν_{LM} is varied (clockwise for positive variations) and, consequently, the migration of the peripheral bulge. This migration is evident in the results described herein (Figure 9a) and in a number of classic analyses [e.g., *Cathles*, 1975; *Peltier and Andrews*, 1976].

The evolution of the Frechet kernels for $\dot{U}_\theta$ along the North American profile is less complicated than the evolution in the radial velocity kernels. As one proceeds from sites B and C, which straddle the point on the profile characterized by the maximum positive tangential velocity, through the peripheral bulge and the far field, the peak amplitude of the kernel diminishes at the same time as the deep mantle sensitivity of the tangential velocity increases. For example, predictions at sites within the main peripheral bulge region (D–F) are sensitive to variations in the lower mantle rheology only in the top 500–700 km or so of that region, whereas the associated calculations at far-field sites (G–I) are sensitive to variations in viscosity throughout the lower mantle. This trend is evident on the middle frame of Figure 9a, where the discrepancy between the three profiles generally increases as one moves toward Richmond in the far field. One of the

main results of the forward calculations described above was the prediction of extensive regions in the far field of the Laurentide ice sheet which are characterized by motions toward the previously glaciated region. The striking sensitivity of this computed motion to variations in ν_{LM} can therefore be ascribed to a sensitivity which persists over the entire lower mantle. Indeed, an examination of the kernel for the $\dot{U}_\theta$ prediction for Richmond indicates that variations in the rheology of the top half of the mantle are only a factor of 2 more efficient at perturbing the tangential velocity computed using the test Earth model than variations in the viscosity in the bottom half of the mantle.

The Frechet kernels for the tangential velocity components in Figure 12, sites A–I, are characterized by uniformly negative values in the upper mantle. This negativity indicates that a reduction in ν_{UM} should produce a positive shift in the tangential velocity components predicted for the Fort Rupert-Richmond profile (or a broadening of the central zone of outward tangential motions, Figure 10a) relative to predictions generated using the test Earth model. This shift will be particularly significant for the case of the $\dot{U}_\theta$ component, and it will be most pronounced in the near field, where the amplitudes of the kernels within the upper mantle peak (sites A–F). Figure 12 (sites A–F) indicates that the broadening is particularly sensitive to variations in rheology in progressively shallower regions of the upper mantle.

The evolution of the Frechet kernels in Figure 12, sites J–R, is reminiscent of the trends evident along the North American profile; however, the kernels for the European sites tend to be "scaled" toward the surface in comparison to the corresponding kernels for North America. This result is not surprising given the difference in the spatial scales of the Laurentian and Fennoscandian ice complexes, and it has several interesting implications. First, in contrast to the North American edge site D, the radial velocity kernel for the edge site M indicates a sensitivity to lower mantle viscosity which is mainly ascribable to the top half of that region. Second, a migration to greater depths of the peak value of the radial velocity kernels as one proceeds through the far field, evident in the North American results, is not nearly as pronounced in the European results. The amplitude of the radial velocity kernel for Wettzell (Figure 12, site R) is largest over depths in the range 400–1300 km, in contrast to the corresponding range of 800–2200 km for the Richmond site. Third, as one proceeds from the central to far-field sites, the region of peak sensitivity exhibited by the kernels for the tangential velocity $\dot{U}_\theta$ in Europe never extends below the top 300 km of the lower mantle.

The tangential motions predicted for the North American profile tend to be more sensitive to variations in ν_{UM} than the corresponding predictions over Europe (see Fig-

ure 10). The kernels shown in Figure 12 indicate that this difference is due not only to the difference in the peak sensitivities evident on the kernels for sites at corresponding points on the two profiles (sites D and M, for example), but also to the different depth-dependent sensitivities which characterize these kernels within the upper mantle.

The Frechet kernels for tangential velocity in Europe exhibit nonzero sensitivity to variations in the viscosity in the deep mantle extending to the CMB. This is a consequence of the contribution to the predicted tangential velocities in Europe from the melting of the Laurentide ice sheet over Canada. The deep mantle sensitivity evident in Fennoscandia should be partitioned into θ and ψ components since the great circle arc extending from Fennoscandia to Laurentia is roughly in a northwest direction, viewed from Fennoscandia. The results of Figure 12, sites J–R, reflect this partitioning.

Calculations Using Realistic Ice Models: Comparison with VLBI Results

Ryan et al. [1993] have analyzed Mark III geodetic VLBI data obtained from 1979 to 1991 to determine the evolutions of a large number of baselines. Their "global" solution (GLB868) included 864,359 group delay measurements obtained in 1648 observing sessions. In this section we consider predictions of velocity vectors (equation (1)) generated using a suite of Earth models (see Table 1) for a subset of the baselines included in the GLB868 solution. The subset is chosen to satisfy the following criteria: (1) At least one of the sites defining each baseline is situated within the region enclosed by the outer edge of the peripheral bulge associated with the melting of either the Laurentian or Fennoscandian ice complexes. (2) The sites defining the baseline are both located on the North American plate or, alternatively, both on the European plate. This restriction ensures that we do not have to correct the baseline velocity results for relative plate motions or to consider the errors in this correction. (3) The baselines do not include sites (e.g., Penticton) near the North American-Pacific plate boundary, which may be subject to significant deformations. These criteria are satisfied by 28 baselines, 23 of which are located in North America. The location of the baselines are given in Figure 13.

Tushingham [1991] has computed baseline rates associated with glacial isostatic adjustment under the assumption that the sites defining the baseline experience only radial motions. In Table 2 we present calculations using the ICE-3G adapted ice history and a gravitationally self-consistent ocean load intended to assess the validity of this assumption (see also *James and Lambert* [1993] and *Mitrovica et al.* [1993]). The format of Table 2a is as follows: The columns are separated into three triplets, each of which refers to results obtained with a different

Earth model. The three columns associated with each Earth model, labelled TOT, RAD and TAN, represent the total predicted baseline velocity component and its contribution from radial and tangential site velocities, respectively. Table 2a includes two representative baselines, Algonquin Park-Gilmore Creek and Onsala-Wettzell. In both cases, three rows corresponding to the L, T, and V components of the predicted baseline velocity components are included (as labeled). Table 2b provides the three components of present-day site velocity for the four sites represented on the two baselines, for each of the Earth models.

The analysis of *Tushingham* [1991] was limited to baselines within North America and (radial) velocity predictions based on the test Earth model only. In the case of the test model results the tangential motions contribute 15% of the predicted length component of the Algonquin Park-Gilmore Creek baseline velocity. However, the results in Table 2a indicate that the Algonquin Park-Gilmore Creek baseline length rates are not dominated by radial site motions for Earth models other than the test model. Furthermore, the rate of change of the Onsala-Wettzell baseline length is dominated by the contribution from tangential motions regardless of the Earth model considered. (The results of *James and Lambert* [1993] also indicate the importance of rebound-related tangential motions to baseline vector velocity.) The *Tushingham* [1991] approximation is therefore not generally valid.

The relatively small contribution from tangential motions to the length component of the Algonquin Park-Gilmore Creek baseline velocity, in the case of the test Earth model, is a result of a relatively rare match between the tangential velocities along the direction of the baseline at the two end sites. In this case, both sites are moving in the same direction along the baseline, with approximately the same velocity (see Figure 3). For computations using model 1, which has a weak upper mantle viscosity, these velocities were both significant and directed oppositely (see Table 2b). For model 5 which has a stiff lower mantle, the velocity components were in the same direction but of very different magnitude.

Tangential velocities always contribute a dominant portion of the predicted length rate of the Onsala-Wettzell baseline for two reasons. First, since the baseline is relatively short (920 km), radial motions at the end sites project weakly onto the baseline direction. Second, both Onsala and Wettzell are located in regions which are not characterized by large radial motions (Figure 13). This is in contrast, for example, to the Algonquin Park site.

The results summarized in Table 2a have important implications for the sensitivity of the baseline velocity components to variations in rheology. For regional baselines the vertical component of baseline velocity tends to be dominated by the radial motions of the end sites. Thus

the sensitivity of this component to variations in mantle viscosity at depth should be approximately proportional to the difference between the Frechet kernels for the radial velocity at the two sites. The Frechet kernel for the transverse component of baseline velocity is a weighted sum of the Frechet kernels for the tangential components of velocity at each of the two sites. Finally, the Frechet kernels for the length component of the baseline velocity will incorporate (i.e., "mix") the sensitivities associated with both radial and tangential motions at the two sites. The results in Table 2a suggest that this mix will generally be dominated by the sensitivity associated with tangential motions for the European baselines. The same is true, although to a lesser extent, for the Algonquin Park-Gilmore Creek baseline.

To illustrate these points, in Figure 14 we show Frechet kernels for a characteristic subset of the North American baselines and for all of the European baselines. The kernels for the vertical component of baseline velocity indicate that this component has a depth-dependent rheological sensitivity reflective of the sensitivities inherent to the radial motions associated with the two sites defining the baseline. For example, Algonquin Park and Gilmore Creek are positioned with respect to the velocity field at sites corresponding closely to sites C and G on Figure 9. The difference between the radial velocity kernels on Figure 12, sites C and G, yields a kernel with essentially the same form as the dashed line on Figure 14 for the Algonquin Park-Gilmore Creek baseline. The Frechet kernel for the vertical component of the Algonquin Park-Gilmore Creek baseline velocity indicates that this component will be about twice as sensitive to a variation in ν_{LM} from the test model value than to an analogous variation in ν_{UM} (see also Table 2a). Furthermore, the kernel indicates a sensitivity which becomes progressively stronger as one proceeds from deeper to shallower regions of the lower mantle.

The Frechet kernel for the length component of the Algonquin Park-Gilmore Creek baseline velocity indicates that this component is progressively more sensitive to variations in rheology as one proceeds from deeper to shallower regions of the lower mantle and relatively insensitive to variations in the rheology of the lower mantle. A comparison of this kernel with those in Figure 12, sites C and G, indicates that the sensitivity of the baseline length rate is associated mainly with the sensitivity inherent to the tangential motions at the end sites. The same conclusion generally applies to the other baselines considered in Figure 14.

It is difficult to identify universally valid trends in the Frechet kernels shown in Figure 14. The baseline components, though not necessarily insensitive to variations in the rheology of the test Earth model in the deepest regions of the mantle, are clearly more sensitive to such

variations in the top half of the mantle. Perhaps the most significant aspect of the results in Figure 14 is that the set of baseline data exhibit significant differences in their sensitivity to depth-dependent variations in rheology. These differences indicate that the ensemble of baseline velocity data, given sufficiently accurate information regarding the ice loading history, has the potential to provide significant constraints on the rheology of various regions within the upper mantle and the top half of the lower mantle.

Table 3 provides the L, T, and V components of the baseline evolution computed using the Earth models listed in Table 1, the ICE-3G adapted ice history and a gravitationally self-consistent ocean load. (Independently derived predictions, for 10 baselines, for the specific case of the test Earth model, have also recently been published by *James and Lambert* [1993].) It is clear from both Table 3 and Figure 14 that the predicted baseline velocity components are a strong function of the radial viscosity profile of the Earth model adopted in the calculations. The results of the last section indicate that these velocities will also be sensitive to variations in the adopted ice model. Accordingly, it may be possible to discriminate between specific combinations of ice history and Earth rheology on the basis of the fit between the predicted baseline velocity components and the components estimated from the analysis of the VLBI data set. In the remainder of this section we perform such an analysis using predictions of the length rate of the five European baselines (Table 3). An analogous study which focuses on the North American baselines is given by *Mitrovica et al.* [1993].

Figure 15 is a plot of the χ^2 residual per degree-of-freedom (henceforth "reduced χ^2") of the VLBI determined length rates for the European baselines relative to the predictions obtained using the indicated Earth model. (The uncertainties of the baseline rate estimates used for the χ^2 calculations and presented below are those given by *Ryan et al.*, [1993], i.e., the statistical standard deviations of the rates scaled by the square-root of the reduced χ^2 residual of the series of baseline length estimates from the best-fit line.) The reduced χ^2 computed assuming that there is no influence on baseline rates due to glacial isostatic adjustment (henceforth "reduced χ^2 of the null hypothesis") is $\sim$2.4. The dominant contributor to the reduced χ^2 for the null hypothesis is the length rate for the rather precisely determined (-0.6 ± 0.2 mm yr^{-1}) Onsala-Wettzell baseline. The Onsala-Medicina baseline, with an observed shortening of 2.1 ± 1.3 mm yr^{-1}, also contributes importantly to the χ^2 residual for the null hypothesis. Clearly, corrections to the VLBI observations of baseline length changes in Europe, for the predicted signature of glacial isostatic adjustment, will lower the χ^2 residual only if these predictions account for some of the shortening evident on the Onsala-Wettzell baseline and, to a lesser extent, on the Onsala-Medicina baseline. It is

clear from Figure 15 (and also Table 3) that predictions based on a number of Earth models, together with the ICE-3G adapted ice loading history, are successful in this respect.

Model 2, for example, which is characterized by LT = 120 km, $\nu_{UM} = 5 \times 10^{20}$ Pa s, and $\nu_{LM} = 2 \times 10^{21}$ Pa s, yields (in combination with the ICE-3G model) predictions of length changes for both the Onsala-Wettzell and Onsala-Medicina baselines of -0.7 mm yr^{-1}. If we use these values to "correct" the observed VLBI baseline length rates, we obtain residual values of -0.1 ± 0.2 mm yr^{-1} for Onsala-Wettzell and -1.4 ± 1.3 mm yr^{-1} for Onsala-Medicina. Neither residual is significantly different from zero; the associated reduced χ^2 for the European baseline length changes is only 0.4. It is perhaps significant that Model 2 is consistent with the inference of *Mitrovica and Peltier* [1993b] based on an inversion of the Fennoscandian relaxation spectrum. These authors found, in the case of LT = 120 km, that their preferred two-layer model consisted of $\nu_{UM} = 4 \times 10^{20}$ Pa s and $\nu_{LM} = 2 \times 10^{21}$ Pa s.

Model 2 does not, however, uniquely "fit" the VLBI estimates. Within the limited class of models considered in Figure 15 there are several which yield predictions of baseline length changes in Europe which are consistent with the VLBI values. Indeed, reduced χ^2 values below 1.0 are obtained for models derived from the test model either by reducing ν_{LM} to 10^{21} Pa s or below, by reducing ν_{UM} to a value between 3 and 7 $\times 10^{20}$ Pa s, or by increasing LT above about 150 km. Of course, the nonuniqueness is even more severe when one takes into account the uncertainty in the ice history. A formal geophysical inversion is required to identify the non-uniqueness inherent to the inference; however the results in Figure 15 represent the solution of the more basic existence problem. That is, we have identified at least one Earth model/ice model combination and, in fact, several such combinations, which fit to the VLBI-determined baseline length rates for the five European baselines. Given that none of the VLBI baseline rate estimates represent a "detection" at the level of greater than 3-σ (and most are less than 2-σ), a more rigorous inversion, or a more labored interpretation, would not be warranted.

Summary and Final Remarks

We have applied the spectral formalism outlined by *Mitrovica et al.*, [this issue] to predict present-day three-dimensional deformation rates and baseline rates driven by the ice and ocean loads associated with the late Pleistocene glacial cycles. One of the main conclusions of the analysis is that the predictions are sensitive to variations in both the viscosity profile of the Earth model and the

details of the late Pleistocene deglaciation event. This sensitivity suggests that "standard" corrections for the signal associated with glacial isostatic adjustment should not be applied to geodetic data in an attempt to remove the signal. Rather, one must consider the potentially large range of signals associated with the phenomenon (see, e.g., Table 3), or simultaneously estimate the glacial isostatic adjustment signal. If the latter is possible then the sensitivities indicated by the present results suggest that attempts may be made to refine constraints on either the ice load history or the Earth rheology, or, more likely, combinations of the two.

James and Lambert [1993] have recently stated that predictions of tangential motions are much more sensitive to details of the viscoelastic Earth models than are radial motions. This generalization is not supported by the results of the present study, which suggest that the sensitivities are a strong function of the geographic location of the site and the specific parameter of the Earth model being varied. Consider, for example, Figure 9, site A. Increasing ν_{LM} by a factor of 5 alters the predicted radial velocity by 9.7 mm yr^{-1} and the horizontal velocity by only 0.6 mm yr^{-1}.

We did not consider transcontinental baselines in the present analysis since those baselines will also be sensitive to plate motions. The contributions to the velocities of sites in North America and Europe due to glacial isostatic adjustment are nonnegligible, and should be taken into account in an analysis of the time behavior of transcontinental baselines. It is important to point out, however, that the continuity of the tangential deformation field associated with melting of Laurentide scale ice sheets was based on spherically symmetric Earth models. Discontinuities in lithospheric strength associated with, e.g., plate boundaries, may well influence this trend.

Acknowledgments. We would like to thank P.M. Mathews, Paul Morgan, and Bruce G. Bills for their constructive comments on this manuscript. We also thank Dazhong Han for providing a viscoelastic impulse-response solution with which to compare our results. This work was supported in part by an NSERC of Canada research grant (J.X.M.), NASA grant NAG5-1930, and the Smithsonian Institution. This study is part of an ongoing effort, funded by the NASA Dynamics of the Solid Earth (DOSE) program, to use three-dimensional space geodetic data to infer rheological properties of the Earth.

References

Cathles, L.M., *The Viscosity of the Earth's Mantle*, Princeton University Press, Princeton, N.J., 1975.

Dziewonski, A.M., and D.L. Anderson, Preliminary reference Earth model (PREM), *Phys. Earth Planet. Inter.*, *25*, 297–356, 1981.

James, T.S., and W.J. Morgan, Horizontal motions due to postglacial rebound, *Geophys. Res. Lett.*, *17*, 957–960, 1990.

James, T.S., and A. Lambert, A comparison of VLBI data with the ICE-3G glacial rebound model, *Geophys. Res. Lett.*, *20*, 871–874, 1993.

Mitrovica, J.X., and W.R. Peltier, On postglacial geoid subsidence over the equatorial oceans, *J. Geophys. Res.*, *96*, 20,053–20,071, 1991.

Mitrovica, J.X., and W.R. Peltier, Present-day secular variations in the zonal harmonics of the Earth's geopotential, *J. Geophys. Res.*, *98*, 4509–4526, 1993a.

Mitrovica, J.X., and W.R. Peltier, The inference of mantle viscosity from an inversion of the Fennoscandian relaxation spectrum, *Geophys. J. Int.*, *114*, 45–62, 1993b.

Mitrovica, J.X., J.L. Davis, and I.I. Shapiro, A spectral formalism for computing three-dimensional deformations due to surface loads, 1, Theory, *J. Geophys. Res.*, this issue.

Mitrovica, J.X., J.L. Davis, and I.I. Shapiro, Constraining proposed combinations of ice history and Earth rheology using VLBI-determined baseline length rates in North America, *Geophys. Res. Lett.*, *20*, 2387–2390, 1993.

Paterson, W.S.B., *The Physics of Glaciers*, Pergamon, New York, 1981.

Peltier, W.R., Deglaciation-induced vertical motion of the North American continent and transient lower mantle rheology, *J. Geophys. Res.*, *91*, 9099-9123, 1986.

Peltier, W.R., and J.T. Andrews, Glacial Isostatic Adjustment I. The forward problem, *Geophys. J. R. Astron. Soc.*, *46*, 605-646, 1976.

Ryan, J.W., C. Ma, and D.S. Caprette, NASA Space Geodesy Program–GSFC Data Analysis—1992, *NASA Tech. Memo. 104572*, 471 pp., 1993.

Tushingham, A.M., Potential effects of ongoing postglacial adjustment on very long baseline interferometry measurements, *Geophys. Res. Lett.*, *18*, 1281-1284, 1991.

Tushingham, A.M. and W.R. Peltier, ICE-3G: A new global model of late Pleistocene deglaciation based upon geophysical predictions of postglacial relative sea level change, *J. Geophys. Res.*, *96*, 4497-4523, 1991.

Tushingham, A.M. and W.R. Peltier, Validation of the ICE-3G model of Wurm-Wisconsin deglaciation using a global data base of relative sea level histories, *J. Geophys. Res.*, *97*, 3285-3304, 1992.

J. L. Davis and I. I. Shapiro, Harvard-Smithsonian Center for Astrophysics, 60 Garden Street, Cambridge, MA 02138.

J. X. Mitrovica, Department of Physics, University of Toronto, 60 St. George Street, Toronto, Ontario, Canada, M5S 1A7.

(Received April 29, 1993; revised November 5, 1993; accepted November 30, 1993.)

MITROVICA ET AL.: THREE-DIMENSIONAL GLACIAL ISOSTATIC ADJUSTMENT
MITROVICA ET AL.: THREE-DIMENSIONAL GLACIAL ISOSTATIC ADJUSTMENT
MITROVICA ET AL.: THREE-DIMENSIONAL GLACIAL ISOSTATIC ADJUSTMENT
MITROVICA ET AL.: THREE-DIMENSIONAL GLACIAL ISOSTATIC ADJUSTMENT
MITROVICA ET AL.: THREE-DIMENSIONAL GLACIAL ISOSTATIC ADJUSTMENT
MITROVICA ET AL.: THREE-DIMENSIONAL GLACIAL ISOSTATIC ADJUSTMENT
MITROVICA ET AL.: THREE-DIMENSIONAL GLACIAL ISOSTATIC ADJUSTMENT
MITROVICA ET AL.: THREE-DIMENSIONAL GLACIAL ISOSTATIC ADJUSTMENT
MITROVICA ET AL.: THREE-DIMENSIONAL GLACIAL ISOSTATIC ADJUSTMENT
MITROVICA ET AL.: THREE-DIMENSIONAL GLACIAL ISOSTATIC ADJUSTMENT
MITROVICA ET AL.: THREE-DIMENSIONAL GLACIAL ISOSTATIC ADJUSTMENT
MITROVICA ET AL.: THREE-DIMENSIONAL GLACIAL ISOSTATIC ADJUSTMENT
MITROVICA ET AL.: THREE-DIMENSIONAL GLACIAL ISOSTATIC ADJUSTMENT
MITROVICA ET AL.: THREE-DIMENSIONAL GLACIAL ISOSTATIC ADJUSTMENT
MITROVICA ET AL.: THREE-DIMENSIONAL GLACIAL ISOSTATIC ADJUSTMENT
MITROVICA ET AL.: THREE-DIMENSIONAL GLACIAL ISOSTATIC ADJUSTMENT
MITROVICA ET AL.: THREE-DIMENSIONAL GLACIAL ISOSTATIC ADJUSTMENT
MITROVICA ET AL.: THREE-DIMENSIONAL GLACIAL ISOSTATIC ADJUSTMENT
MITROVICA ET AL.: THREE-DIMENSIONAL GLACIAL ISOSTATIC ADJUSTMENT
MITROVICA ET AL.: THREE-DIMENSIONAL GLACIAL ISOSTATIC ADJUSTMENT
MITROVICA ET AL.: THREE-DIMENSIONAL GLACIAL ISOSTATIC ADJUSTMENT
MITROVICA ET AL.: THREE-DIMENSIONAL GLACIAL ISOSTATIC ADJUSTMENT
MITROVICA ET AL.: THREE-DIMENSIONAL GLACIAL ISOSTATIC ADJUSTMENT
MITROVICA ET AL.: THREE-DIMENSIONAL GLACIAL ISOSTATIC ADJUSTMENT

Figure 1. Present-day deformation rates computed using the ice disk models with maximum radius (a) and (b) 16° and (c) and (d) 8°. The solid line on each frame is generated using the test Earth model. The remaining lines are generated using an Earth model constructed by varying a single parameter of the test model: LT=96 km (dashed line); $\nu_{UM} = 3 \times 10^{20}$ Pa s (dashed-dotted line); and $\nu_{LM} = 5 \times 10^{21}$ Pa s (dotted line). As a consequence of symmetry, the tangential velocity is identically zero at the center of the disk location and at the antipole. A positive tangential velocity refers to motion directed away from the center of the disk load.

Figure 2. As in Figures 1a and 1b, except that the dashed line was computed using the test Earth model with an elastically incompressible rheology. A positive tangential velocity refers to motion directed away from the center of the disk load.

Figure 3. Plots of the predicted (bottom) present-day radial and (top) tangential velocity over North America and Europe computed using the test Earth model and a surface mass load composed of the ICE-3G adapted ice history and a gravitationally self-consistent ocean load. The solid dots (top frames) refer to the sites: Gilmore Creek, Alaska (G); Fort Rupert, Quebec (F); Algonquin Park, Ontario (A); Richmond, Florida (R); Onsala, Sweden (O); Luleå, Sweden (L); and Wettzell, Germany (W).

Figure 4. (a) The present-day three-dimensional velocities computed along the profile from Fort Rupert to Richmond using the test Earth model and a gravitationally self-consistent ocean mass redistribution. The solid and dashed lines were computed using ice loads adapted from, respectively, the ICE-3G and ICE-1 deglaciation histories. (b) As in Figure 4a, except for the profile extending from Luleå to Wettzell.

Figure 5. As in Figure 3, except for an ice load adapted from the ICE-1 deglaciation history.

Figure 6. As in Figure 4, except all calculations use an ice load adapted from the ICE-3G deglaciation history and the test Earth model. The solid, dashed and dotted lines were generated by assuming a gravitationally self-consistent ocean mass redistribution, a eustatic ocean mass redistribution, and no ocean load component, respectively.

Figure 7. Vector plots of present-day tangential velocities at selected coastal sites in (a) eastern North America and (b) Europe, computed using the test Earth model and the ICE-3G adapted ice loading history. The vectors whose heads are given by solid triangles, open triangles, or two lines, refer to results generated using a gravitationally self-consistent, eustatic, or no ocean load. The numbers refer to the sites: 1, Fort George, Quebec; 2, Indian Harbour, Newfoundland; 3, Ille d'Anticosti, Quebec; 4, Quebec City, Quebec; 5, Boston, Massachusetts; 6, Philadelphia, Pennsylvania; 7, Charleston, South Carolina; 8, Bodo, Norway; 9, Bergen, Norway; 10, Egersund, Norway; 11, Thurso, Scotland; 12, The Hague, The Netherlands; 13, Göteborg, Sweden; 14, Karlskrona, Sweden; 15, Visby, Sweden; 16, Helsinki, Finland.

Figure 8. As in Figure 4, except that the lines on each frame are distinguished by the Earth model used in the calculations. The solid line was computed using the test Earth model (LT = 120 km). The dashed and dotted lines are computed by changing LT to 95 and 145 km, respectively. The surface load was composed of the ICE-3G adapted ice history and a gravitationally self-consistent ocean redistribution.

Figure 9. As in Figure 8, except that the dashed and dotted lines were computed by changing ν_{LM} from the test model value (2×10^{21} Pa s) to 10^{21} and 5×10^{21} Pa s, respectively. The arrows labeled A to R indicate the location of 18 specific sites on the profiles for which Frechet kernels are presented on Figure 12.

Figure 10. As in Figure 8, except that the dashed and dotted lines were computed by changing ν_{UM} from the test model value (10^{21} Pa s) to 5×10^{20} and 3×10^{20} Pa s, respectively.

Figure 11. (top) The present-day $\dot{U}_\theta$ component of tangential velocities along the great circle profile from Fort Rupert to Richmond, relative to the value obtained at Fort Rupert, computed using the results in Figure 9. (bottom) As in top, except for the European profile and Luleå.

Figure 12. Frechet kernels for the components of present-day velocities computed using the test Earth model. The solid, dashed, and dotted lines refer to the kernels for $\dot{U}_r$, $\dot{U}_\psi$ and $\dot{U}_\theta$, respectively. Each frame provides the kernels for a different site (see Figure 9) on either the Fort Rupert-Richmond profile (A to I), or the Luleå-Wettzell profile (J to R).

Figure 12. (continued)

Figure 13. The VLBI baselines included in this study (see Table 3). The letters denote specific VLBI sites: (A) Algonquin Park; (B) Beltsville; (E) Effelsberg; (F) Ft. Davis; (G) Gilmore Creek; (H) Haystack; (M) Maryland Point; (Ma) Madrid; (Me) Medicina; (N) Green Bank; (No) Noto; (O) Onsala; (P) Platteville; (R) Richmond; (W) Westford; (We) Wettzell; and (Wh) Whitehorse. The shaded region in each frame shows the geographic extent of the North American and Fennoscandian ice cover during the last glacial maximum according to the ICE-3G model [*Tushingham and Peltier*, 1991].

Figure 14. Frechet kernels for a subset of the North American baselines and all the European baselines generated using the test Earth model. The solid, dashed, and dotted lines refer to the kernels for the L, V, and T components, respectively, of the baseline rates of change.

Figure 14. (continued)

Figure 15. The reduced χ^2 for the European VLBI baseline rate determinations relative to predictions based on three families of Earth models. The solid, dashed, and dotted lines join results based on varying the value of ν_{UM}, ν_{LM}, and LT, respectively, in the test model.

Figure 1. Present-day deformation rates computed using the ice disk models with maximum radius (a) and (b) 16° and (c) and (d) 8°. The solid line on each frame is generated using the test Earth model. The remaining lines are generated using an Earth model constructed by varying a single parameter of the test model: LT=96 km (dashed line); $\nu_{UM} = 3 \times 10^{20}$ Pa s (dashed-dotted line); and $\nu_{LM} = 5 \times 10^{21}$ Pa s (dotted line). As a consequence of symmetry, the tangential velocity is identically zero at the center of the disk location and at the antipole. A positive tangential velocity refers to motion directed away from the center of the disk load.

Figure 2. As in Figures 1a and 1b, except that the dashed line was computed using the test Earth model with an elastically incompressible rheology. A positive tangential velocity refers to motion directed away from the center of the disk load.

Figure 3. Plots of the predicted (bottom) present-day radial and (top) tangential velocity over North America and Europe computed using the test Earth model and a surface mass load composed of the ICE-3G adapted ice history and a gravitationally self-consistent ocean load. The solid dots (top frames) refer to the sites: Gilmore Creek, Alaska (G); Fort Rupert, Quebec (F); Algonquin Park, Ontario (A); Richmond, Florida (R); Onsala, Sweden (O); Luleå, Sweden (L); and Wettzell, Germany (W).

Figure 4. (a) The present-day three-dimensional velocities computed along the profile from Fort Rupert to Richmond using the test Earth model and a gravitationally self-consistent ocean mass redistribution. The solid and dashed lines were computed using ice loads adapted from, respectively, the ICE-3G and ICE-1 deglaciation histories. (b) As in Figure 4a, except for the profile extending from Luleå to Wettzell.

Figure 5. As in Figure 3, except for an ice load adapted from the ICE-1 deglaciation history.

Figure 6. As in Figure 4, except all calculations use an ice load adapted from the ICE-3G deglaciation history and the test Earth model. The solid, dashed and dotted lines were generated by assuming a gravitationally self-consistent ocean mass redistribution, a eustatic ocean mass redistribution, and no ocean load component, respectively.

Figure 7. Vector plots of present-day tangential velocities at selected coastal sites in (a) eastern North America and (b) Europe, computed using the test Earth model and the ICE-3G adapted ice loading history. The vectors whose heads are given by solid triangles, open triangles, or two lines, refer to results generated using a gravitationally self-consistent, eustatic, or no ocean load. The numbers refer to the sites: 1, Fort George, Quebec; 2, Indian Harbour, Newfoundland; 3, Ille d'Anticosti, Quebec; 4, Quebec City, Quebec; 5, Boston, Massachusetts; 6, Philadelphia, Pennsylvania; 7, Charleston, South Carolina; 8, Bodo, Norway; 9, Bergen, Norway; 10, Egersund, Norway; 11, Thurso, Scotland; 12, The Hague, The Netherlands; 13, Göteborg, Sweden; 14, Karlskrona, Sweden; 15, Visby, Sweden; 16, Helsinki, Finland.

Figure 8. As in Figure 4, except that the lines on each frame are distinguished by the Earth model used in the calculations. The solid line was computed using the test Earth model (LT = 120 km). The dashed and dotted lines are computed by changing LT to 95 and 145 km, respectively. The surface load was composed of the ICE-3G adapted ice history and a gravitationally self-consistent ocean redistribution.

Figure 9. As in Figure 8, except that the dashed and dotted lines were computed by changing ν_{LM} from the test model value (2×10^{21} Pa s) to 10^{21} and 5×10^{21} Pa s, respectively. The arrows labeled A to R indicate the location of 18 specific sites on the profiles for which Frechet kernels are presented on Figure 12.

Figure 10. As in Figure 8, except that the dashed and dotted lines were computed by changing ν_{UM} from the test model value (10^{21} Pa s) to 5×10^{20} and 3×10^{20} Pa s, respectively.

Figure 11. (top) The present-day $\dot{U}_\theta$ component of tangential velocities along the great circle profile from Fort Rupert to Richmond, relative to the value obtained at Fort Rupert, computed using the results in Figure 9. (bottom) As in top, except for the European profile and Luleå.

Figure 12. Frechet kernels for the components of present-day velocities computed using the test Earth model. The solid, dashed, and dotted lines refer to the kernels for $\dot{U}_r$, $\dot{U}_\psi$ and $\dot{U}_\theta$, respectively. Each frame provides the kernels for a different site (see Figure 9) on either the Fort Rupert-Richmond profile (A to I), or the Luleå-Wettzell profile (J to R).

Figure 12. (continued)

Figure 13. The VLBI baselines included in this study (see Table 3). The letters denote specific VLBI sites: (A) Algonquin Park; (B) Beltsville; (E) Effelsberg; (F) Ft. Davis; (G) Gilmore Creek; (H) Haystack; (M) Maryland Point; (Ma) Madrid; (Me) Medicina; (N) Green Bank; (No) Noto; (O) Onsala; (P) Platteville; (R) Richmond; (W) Westford; (We) Wettzell; and (Wh) Whitehorse. The shaded region in each frame shows the geographic extent of the North American and Fennoscandian ice cover during the last glacial maximum according to the ICE-3G model [*Tushingham and Peltier*, 1991].

Figure 14. Frechet kernels for a subset of the North American baselines and all the European baselines generated using the test Earth model. The solid, dashed, and dotted lines refer to the kernels for the L, V, and T components, respectively, of the baseline rates of change.

Figure 14. (continued)

Figure 15. The reduced χ^2 for the European VLBI baseline rate determinations relative to predictions based on three families of Earth models. The solid, dashed, and dotted lines join results based on varying the value of ν_{UM}, ν_{LM}, and LT, respectively, in the test model.

Figure 1. Present-day deformation rates computed using the ice disk models with maximum radius (a) and (b) 16° and (c) and (d) 8°. The solid line on each frame is generated using the test Earth model. The remaining lines are generated using an Earth model constructed by varying a single parameter of the test model: LT=96 km (dashed line); $\nu_{UM} = 3 \times 10^{20}$ Pa s (dashed-dotted line); and $\nu_{LM} = 5 \times 10^{21}$ Pa s (dotted line). As a consequence of symmetry, the tangential velocity is identically zero at the center of the disk location and at the antipole. A positive tangential velocity refers to motion directed away from the center of the disk load.

Figure 2. As in Figures 1a and 1b, except that the dashed line was computed using the test Earth model with an elastically incompressible rheology. A positive tangential velocity refers to motion directed away from the center of the disk load.

Figure 3. Plots of the predicted (bottom) present-day radial and (top) tangential velocity over North America and Europe computed using the test Earth model and a surface mass load composed of the ICE-3G adapted ice history and a gravitationally self-consistent ocean load. The solid dots (top frames) refer to the sites: Gilmore Creek, Alaska (G); Fort Rupert, Quebec (F); Algonquin Park, Ontario (A); Richmond, Florida (R); Onsala, Sweden (O); Luleå, Sweden (L); and Wettzell, Germany (W).

Figure 4. (a) The present-day three-dimensional velocities computed along the profile from Fort Rupert to Richmond using the test Earth model and a gravitationally self-consistent ocean mass redistribution. The solid and dashed lines were computed using ice loads adapted from, respectively, the ICE-3G and ICE-1 deglaciation histories. (b) As in Figure 4a, except for the profile extending from Luleå to Wettzell.

Figure 5. As in Figure 3, except for an ice load adapted from the ICE-1 deglaciation history.

Figure 6. As in Figure 4, except all calculations use an ice load adapted from the ICE-3G deglaciation history and the test Earth model. The solid, dashed and dotted lines were generated by assuming a gravitationally self-consistent ocean mass redistribution, a eustatic ocean mass redistribution, and no ocean load component, respectively.

Figure 7. Vector plots of present-day tangential velocities at selected coastal sites in (a) eastern North America and (b) Europe, computed using the test Earth model and the ICE-3G adapted ice loading history. The vectors whose heads are given by solid triangles, open triangles, or two lines, refer to results generated using a gravitationally self-consistent, eustatic, or no ocean load. The numbers refer to the sites: 1, Fort George, Quebec; 2, Indian Harbour, Newfoundland; 3, Ille d'Anticosti, Quebec; 4, Quebec City, Quebec; 5, Boston, Massachusetts; 6, Philadelphia, Pennsylvania; 7, Charleston, South Carolina; 8, Bodo, Norway; 9, Bergen, Norway; 10, Egersund, Norway; 11, Thurso, Scotland; 12, The Hague, The Netherlands; 13, Göteborg, Sweden; 14, Karlskrona, Sweden; 15, Visby, Sweden; 16, Helsinki, Finland.

Figure 8. As in Figure 4, except that the lines on each frame are distinguished by the Earth model used in the calculations. The solid line was computed using the test Earth model (LT = 120 km). The dashed and dotted lines are computed by changing LT to 95 and 145 km, respectively. The surface load was composed of the ICE-3G adapted ice history and a gravitationally self-consistent ocean redistribution.

Figure 9. As in Figure 8, except that the dashed and dotted lines were computed by changing ν_{LM} from the test model value (2×10^{21} Pa s) to 10^{21} and 5×10^{21} Pa s, respectively. The arrows labeled A to R indicate the location of 18 specific sites on the profiles for which Frechet kernels are presented on Figure 12.

Figure 10. As in Figure 8, except that the dashed and dotted lines were computed by changing ν_{UM} from the test model value (10^{21} Pa s) to 5×10^{20} and 3×10^{20} Pa s, respectively.

Figure 11. (top) The present-day $\dot{U}_\theta$ component of tangential velocities along the great circle profile from Fort Rupert to Richmond, relative to the value obtained at Fort Rupert, computed using the results in Figure 9. (bottom) As in top, except for the European profile and Luleå.

Figure 12. Frechet kernels for the components of present-day velocities computed using the test Earth model. The solid, dashed, and dotted lines refer to the kernels for $\dot{U}_r$, $\dot{U}_\psi$ and $\dot{U}_\theta$, respectively. Each frame provides the kernels for a different site (see Figure 9) on either the Fort Rupert-Richmond profile (A to I), or the Luleå-Wettzell profile (J to R).

Figure 12. (continued)

Figure 13. The VLBI baselines included in this study (see Table 3). The letters denote specific VLBI sites: (A) Algonquin Park; (B) Beltsville; (E) Effelsberg; (F) Ft. Davis; (G) Gilmore Creek; (H) Haystack; (M) Maryland Point; (Ma) Madrid; (Me) Medicina; (N) Green Bank; (No) Noto; (O) Onsala; (P) Platteville; (R) Richmond; (W) Westford; (We) Wettzell; and (Wh) Whitehorse. The shaded region in each frame shows the geographic extent of the North American and Fennoscandian ice cover during the last glacial maximum according to the ICE-3G model [*Tushingham and Peltier,* 1991].

Figure 14. Frechet kernels for a subset of the North American baselines and all the European baselines generated using the test Earth model. The solid, dashed, and dotted lines refer to the kernels for the L, V, and T components, respectively, of the baseline rates of change.

Figure 14. (continued)

Figure 15. The reduced χ^2 for the European VLBI baseline rate determinations relative to predictions based on three families of Earth models. The solid, dashed, and dotted lines join results based on varying the value of ν_{UM}, ν_{LM}, and LT, respectively, in the test model.

Table 1. Models Used in Numerical Calculations

Model	Lithospheric Thickness, km	Upper Mantle Viscosity, 10^{21} Pa s	Lower Mantle Viscosity, 10^{21} Pa s
Test	120	1.0	2.0
1	120	0.3	2.0
2	120	0.5	2.0
3	120	1.0	0.5
4	120	1.0	1.0
5	120	1.0	5.0
6	71	1.0	2.0
7	96	1.0	2.0
8	145	1.0	2.0

All models have an elastic structure given by the seismically determined model PREM [*Dziewonski and Anderson*, 1981].

Table 2a. Contributions to Baseline Velocity Predictions of Radial and Tangential Site Velocities

	Test Model			Model 1			Model 5		
L/T/V	TOT	RAD	TAN	TOT	RAD	TAN	TOT	RAD	TAN
				Algonquin Park-Gilmore Creek					
L	1.2	1.1	0.2	3.3	0.7	2.7	0.9	1.9	−1.0
T	0.7	0.0	0.7	0.5	0.0	0.5	1.3	0.0	1.3
V	4.7	5.1	−0.4	2.0	2.3	−0.3	8.3	8.9	−0.6
				Onsala-Wettzell					
L	−1.1	0.1	−1.2	−0.3	−0.1	−0.4	−1.3	0.1	−1.4
T	−0.4	0.0	−0.4	−0.1	0.0	−0.1	−0.8	0.0	−0.8
V	1.3	1.3	0.0	1.0	0.9	0.1	2.1	2.2	−0.1

All rates expressed in millimeters per year. *L*, *T*, and *V* indicate the length, transverse, and vertical baseline rate vector components, respectively. TOT, RAD, and TAN indicate contributions from the total, radial, and tangential site velocities, respectively.

Table 2b. Predicted Site Velocities

Site	Test Model			Model 1			Model 5		
	$\dot{U}_r$	$\dot{U}_\theta$	$\dot{U}_\psi$	$\dot{U}_r$	$\dot{U}_\theta$	$\dot{U}_\psi$	$\dot{U}_r$	$\dot{U}_\theta$	$\dot{U}_\psi$
Algonquin Park	4.2	0.8	0.1	2.2	1.9	0.4	7.5	0.3	0.1
Gilmore Creek	−1.2	−0.4	0.4	−0.2	0.5	−1.0	−2.0	−1.4	1.2
Onsala	1.2	0.9	−0.5	0.8	1.1	−0.1	1.7	0.1	−1.1
Wettzell	−0.1	−0.3	−0.1	−0.0	0.7	0.0	−0.4	−1.4	−0.4

All rates expressed in millimeters per year.

Table 3. Velocities for North American and European Baselines

Baseline		Model 1	2	T	3	4	T	5	6	7	T	8	Baseline Rate(s)
Algonquin Park-	L	3.3	3.0	1.2	0.4	1.0	1.2	0.9	−0.9	0.4	1.2	1.7	3.3 ± 0.8
Gilmore Creek	T	0.5	0.8	0.7	−0.3	0.0	0.7	1.3	0.8	0.7	0.7	0.7	
	V	2.0	2.8	4.7	0.7	1.8	4.7	8.3	4.4	4.6	4.7	4.8	
Algonquin Park-	L	0.3	0.1	−0.1	−0.1	0.0	−0.1	−0.1	0.0	0.0	−0.1	−0.1	−0.7 ± 0.5 (b)
Westford	T	−0.5	−0.7	−0.6	−0.2	−0.4	−0.6	−0.8	−0.4	−0.5	−0.6	−0.8	
	V	2.6	4.0	5.8	2.4	3.7	5.8	7.8	5.2	5.5	5.8	6.0	
Beltsville-	L	0.2	0.1	−0.1	0.0	0.0	−0.1	−0.1	−0.2	−0.1	−0.1	0.0	3.4 ± 1.3 (a)
Green Bank	T	0.1	0.1	0.1	0.0	0.1	0.1	0.1	0.1	0.1	0.1	0.1	
	V	−0.1	−0.2	−0.2	−0.3	−0.3	−0.2	0.0	0.0	−0.1	−0.2	−0.2	
Beltsville-	L	−0.7	−0.8	−0.5	0.4	0.2	−0.5	−1.2	−0.4	−0.5	−0.5	−0.5	6.9 ± 2.5
Richmond	T	0.4	0.4	0.1	−0.1	0.0	0.1	0.1	−0.3	−0.1	0.1	0.1	
	V	0.1	−0.7	−1.9	−1.1	−1.7	−1.9	−1.0	−2.1	−2.0	−1.9	−1.7	
Beltsville-	L	0.1	0.0	−0.2	−0.1	−0.1	−0.2	−0.2	−0.3	−0.3	−0.2	−0.1	0.0 ± 3.0 (b)
Westford	T	0.4	0.4	0.4	0.0	0.1	0.4	0.5	0.3	0.4	0.4	0.4	
	V	−0.3	−0.2	−0.5	0.6	0.4	−0.5	−1.4	−0.6	−0.6	−0.5	−0.4	
Ft. Davis-	L	1.2	0.6	−0.8	0.2	0.3	−0.8	−2.8	−2.0	−1.3	−0.8	−0.5	2.7 ± 1.7
Gilmore Creek	T	0.4	0.3	−0.2	0.0	0.0	−0.2	−0.4	−0.4	−0.3	−0.2	−0.1	
	V	−0.2	−0.7	−1.6	0.3	−0.6	−1.6	−1.8	−1.6	−1.6	−1.6	−1.5	
Ft. Davis-	L	0.4	0.0	−0.6	0.2	0.2	−0.6	−1.7	−1.3	−0.9	−0.6	−0.4	−1.0 ± 1.0 (c)
Green Bank	T	0.7	0.6	0.0	−0.4	−0.3	0.0	0.3	−0.2	−0.1	0.0	0.1	
	V	0.3	1.0	2.3	0.6	1.6	2.3	1.5	2.5	2.4	2.3	2.1	
Ft. Davis-	L	0.8	0.4	−0.4	0.0	0.1	−0.4	−1.4	−1.4	−0.8	−0.4	−0.2	−1.1 ± 0.3 (b)
Westford	T	1.1	1.1	0.5	−0.3	−0.1	0.5	0.8	0.0	0.3	0.5	0.5	0.9 ± 0.9 (d)
	V	0.2	1.2	2.1	1.5	2.3	2.1	0.3	2.0	2.0	2.1	2.0	
Gilmore Creek-	L	1.9	0.8	−1.8	−0.3	−0.5	−1.8	−3.6	−3.6	−2.5	−1.8	−1.4	−0.5 ± 1.4 (a)
Green Bank	T	0.1	0.2	0.2	−0.4	−0.3	0.2	0.9	0.4	0.3	0.2	0.2	
	V	0.3	0.5	0.6	0.7	0.8	0.6	−0.2	0.8	0.7	0.6	0.5	
Gilmore Creek-	L	1.2	0.5	−1.2	0.3	0.1	−1.2	−2.7	−2.3	−1.6	−1.2	−1.0	5.6 ± 2.3
Platteville	T	0.0	0.0	0.0	−0.2	−0.1	0.0	0.4	0.1	0.1	0.0	0.0	
	V	0.5	0.3	−0.1	−0.4	−0.5	−0.1	−0.1	−0.2	−0.3	−0.1	0.0	
Gilmore Creek-	L	1.2	0.4	−1.3	0.5	0.4	−1.3	−3.9	−2.7	−1.9	−1.3	−1.0	1.1 ± 1.2
Richmond	T	−0.4	−0.2	0.2	−0.1	−0.1	0.2	0.7	0.6	0.3	0.2	0.2	
	V	0.1	−0.3	−0.9	0.2	−0.3	−0.9	−1.1	−0.8	−0.9	−0.9	−0.8	
Gilmore Creek-	L	2.4	1.3	−1.3	−0.6	−0.5	−1.3	−2.6	−3.1	−2.0	−1.3	−0.9	−0.4 ± 0.5 (b)
Westford	T	0.1	0.1	0.1	−0.4	−0.3	0.1	0.6	0.3	0.2	0.1	0.1	−2.3 ± 2.2 (d)
	V	0.3	0.8	0.6	1.6	1.5	0.6	−1.1	0.4	0.5	0.6	0.6	
Gilmore Creek-	L	0.1	−0.1	−0.5	−0.1	−0.1	−0.5	−0.9	−0.7	−0.6	−0.5	−0.4	−3.8 ± 3.8
Whitehorse	T	0.3	0.4	0.2	−0.2	−0.1	0.2	0.5	−0.2	0.1	0.2	0.3	
	V	−1.1	−2.2	−4.3	−2.4	−3.0	−4.3	−6.1	−6.5	−5.5	−4.3	−3.5	

Green Bank-	L	−0.7	−0.7	−0.3	0.5	0.3	−0.3	−1.0	−0.2	−0.3	−0.3	−0.4	2.2 ± 0.9 (a)
Richmond	T	0.1	0.1	0.0	−0.1	0.0	0.0	−0.1	−0.2	−0.1	0.0	0.0	
	V	0.2	−0.5	−1.7	−0.8	−1.4	−1.7	−1.0	−2.1	−1.9	−1.7	−1.5	
Green Bank-	L	0.3	0.2	−0.2	−0.1	−0.1	−0.2	−0.2	−0.5	−0.3	−0.2	−0.1	4.0 ± 2.0 (a,b)
Westford	T	0.5	0.6	0.5	0.0	0.2	0.5	0.7	0.3	0.5	0.5	0.5	0.5 ± 0.3 (a,d)
	V	−0.2	0.1	−0.3	0.9	0.7	−0.3	−1.3	−0.5	−0.4	−0.3	−0.1	1.4 ± 2.0 (c,d)
Maryland Pt.-	L	−0.6	−0.7	−0.4	0.4	0.3	−0.4	−1.1	−0.3	−0.4	−0.4	−0.4	0.6 ± 4.4
Richmond	T	0.4	0.3	0.1	−0.1	0.0	0.1	0.1	−0.2	−0.1	0.1	0.1	
	V	0.1	−0.7	−1.9	−0.9	−1.5	−1.9	−1.2	−2.2	−2.0	−1.9	−1.7	
Maryland Pt.-	L	0.1	0.0	−0.3	−0.1	−0.2	−0.3	−0.3	−0.4	−0.3	−0.3	−0.2	1.4 ± 1.5 (b)
Westford	T	0.4	0.5	0.4	0.0	0.1	0.4	0.6	0.3	0.4	0.4	0.4	
	V	−0.4	−0.2	−0.5	0.8	0.5	−0.5	−1.5	−0.6	−0.6	−0.5	−0.4	
Platteville-	L	1.2	0.7	−0.6	−0.1	−0.1	−0.6	−1.4	−1.7	−1.0	−0.6	−0.4	3.3 ± 2.2 (b)
Westford	T	0.6	0.7	0.4	−0.3	0.0	0.4	0.7	0.3	0.4	0.4	0.5	
	V	−0.4	0.2	0.6	2.2	2.1	0.6	−1.3	0.6	0.6	0.6	0.5	
Richmond-	L	−0.6	−0.8	−0.6	0.3	0.1	−0.6	−1.3	−0.7	−0.7	−0.6	−0.6	-0.2 ± 0.1 (b)
Westford	T	0.9	0.9	0.4	−0.2	0.1	0.4	0.7	−0.1	0.3	0.4	0.5	
	V	−0.4	0.6	1.4	1.7	2.0	1.4	−0.4	1.5	1.4	1.4	1.3	
Effelsberg-	L	−0.3	−0.8	−1.3	−0.7	−0.9	−1.3	−1.7	−1.3	−1.3	−1.3	−1.2	0.2 ± 2.1
Onsala	T	0.1	0.2	0.3	0.4	0.4	0.3	0.1	0.2	0.3	0.3	0.2	
	V	−1.0	−1.2	−1.5	0.1	−0.5	−1.5	−2.4	−0.5	−1.1	−1.5	−1.8	
Madrid-	L	−0.3	−0.7	−0.9	−0.2	−0.4	−0.9	−1.6	−1.1	−1.0	−0.9	−0.7	0.0 ± 2.7
Onsala	T	0.3	0.4	0.4	0.4	0.5	0.4	0.2	0.2	0.4	0.4	0.4	
	V	−1.0	−0.8	−0.8	0.3	0.0	−0.8	−1.5	0.4	−0.3	−0.8	−1.0	
Medicina-	L	−0.4	−0.7	−1.0	−0.5	−0.7	−1.0	−1.2	−1.0	−1.0	−1.0	−0.8	-2.1 ± 1.3
Onsala	T	−0.1	−0.2	−0.3	0.1	0.0	−0.3	−0.8	−0.4	−0.4	−0.3	−0.3	
	V	−1.2	−1.2	−1.3	0.2	−0.3	−1.3	−2.0	−0.2	−0.9	−1.3	−1.5	
Noto-	L	−0.6	−0.9	−1.0	−0.6	−0.8	−1.0	−1.0	−0.9	−1.0	−1.0	−0.9	-3.4 ± 4.3
Onsala	T	−0.2	−0.4	−0.5	0.0	−0.1	−0.5	−1.0	−0.6	−0.6	−0.5	−0.5	
	V	−1.6	−1.7	−2.0	−0.6	−1.1	−2.0	−2.4	−0.8	−1.6	−2.0	−2.3	
Onsala-	L	−0.3	−0.7	−1.1	−0.7	−0.9	−1.1	−1.3	−1.1	−1.1	−1.1	−1.0	-0.6 ± 0.2
Wettzell	T	−0.1	−0.3	−0.4	−0.1	−0.2	−0.4	−0.8	−0.5	−0.4	−0.4	−0.4	
	V	1.0	1.0	1.3	−0.3	0.3	1.3	2.0	0.4	0.9	1.3	1.6	

The model "T" refers to the test Earth model (see text). All rates expressed in millimeters per year. Letters in last column are used to indicate which of two antennas at a site (or sites) was involved in obtaining the results shown, according to the following scheme: (a) NRAO 85' antenna, Green Bank; (b) Westford antenna, Westford; (c) NRAO 140' antenna, Green Bank; (d) Haystack antenna, Westford.

Table 3. Velocities for North American and European Baselines (continued)

Baseline	Model											Baseline Rate(s)
	1	2	T	3	4	T	5	6	7	T	8	

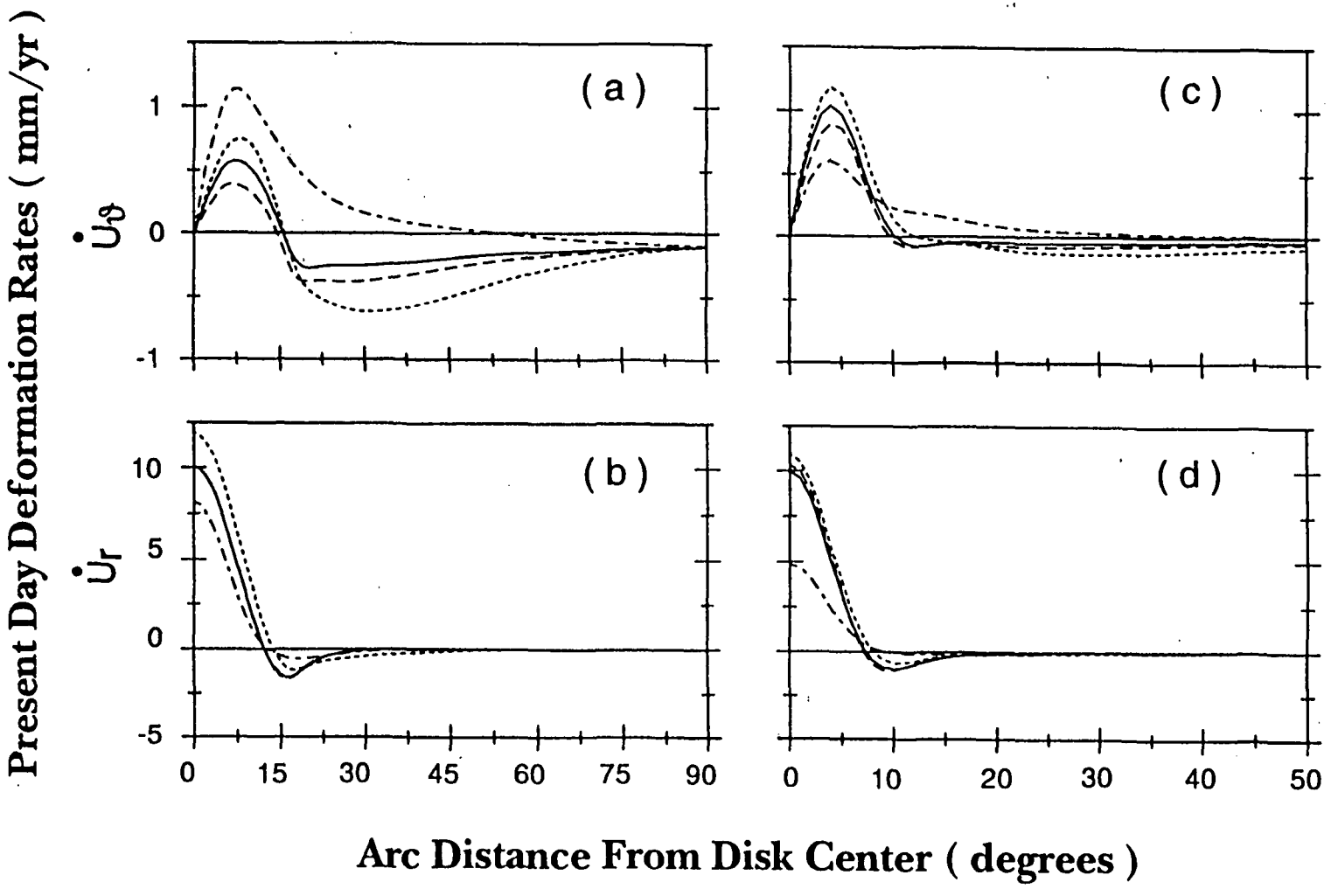
Present Day Deformation Rates (mm/yr)
$\dot{U}_\vartheta$
$\dot{U}_r$
(a)
(b)
(c)
(d)
1
0
-1
10
5
0
-5
0
15
30
45
60
75
90
0
10
20
30
40
50
Arc Distance From Disk Center (degrees)

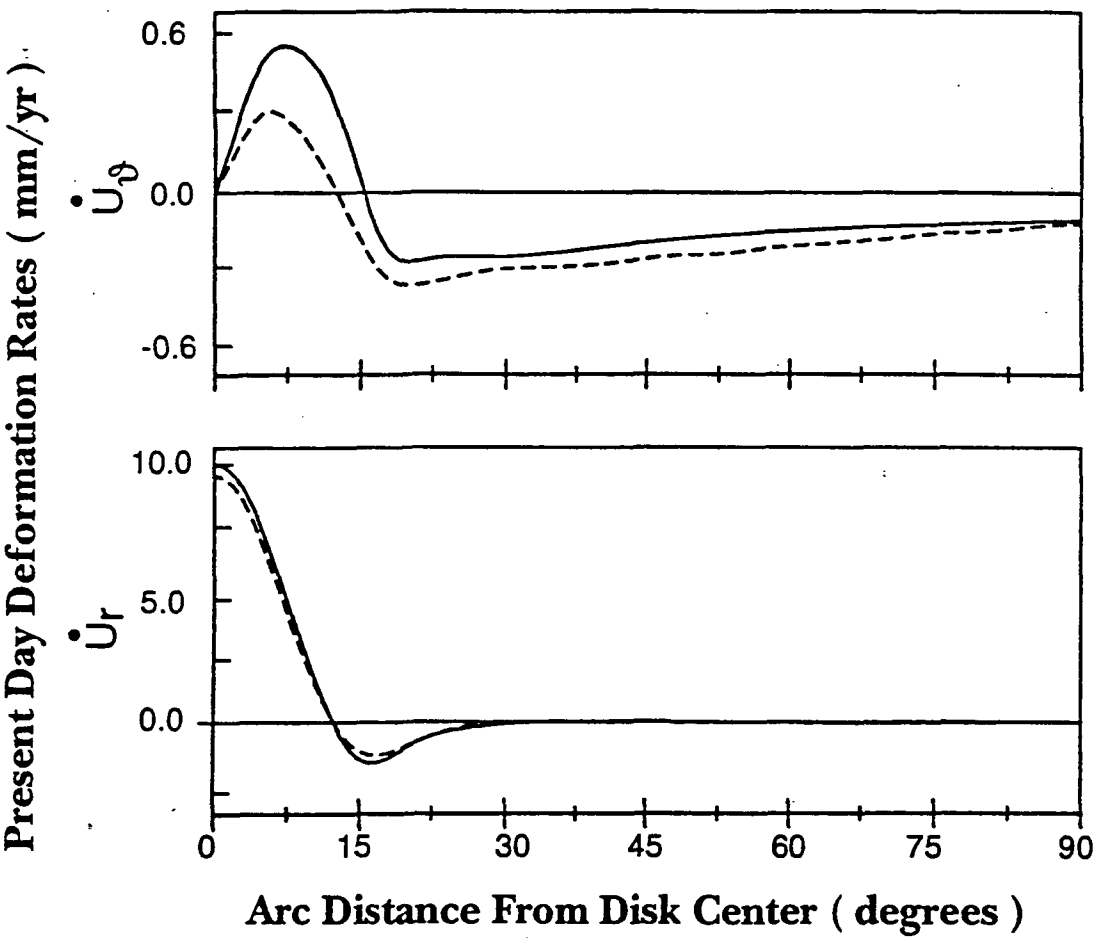
Present Day Deformation Rates (mm/yr)
$\dot{U}_\vartheta$
0.6
0.0
-0.6
$\dot{U}_r$
10.0
5.0
0.0
0
15
30
45
60
75
90
Arc Distance From Disk Center (degrees)

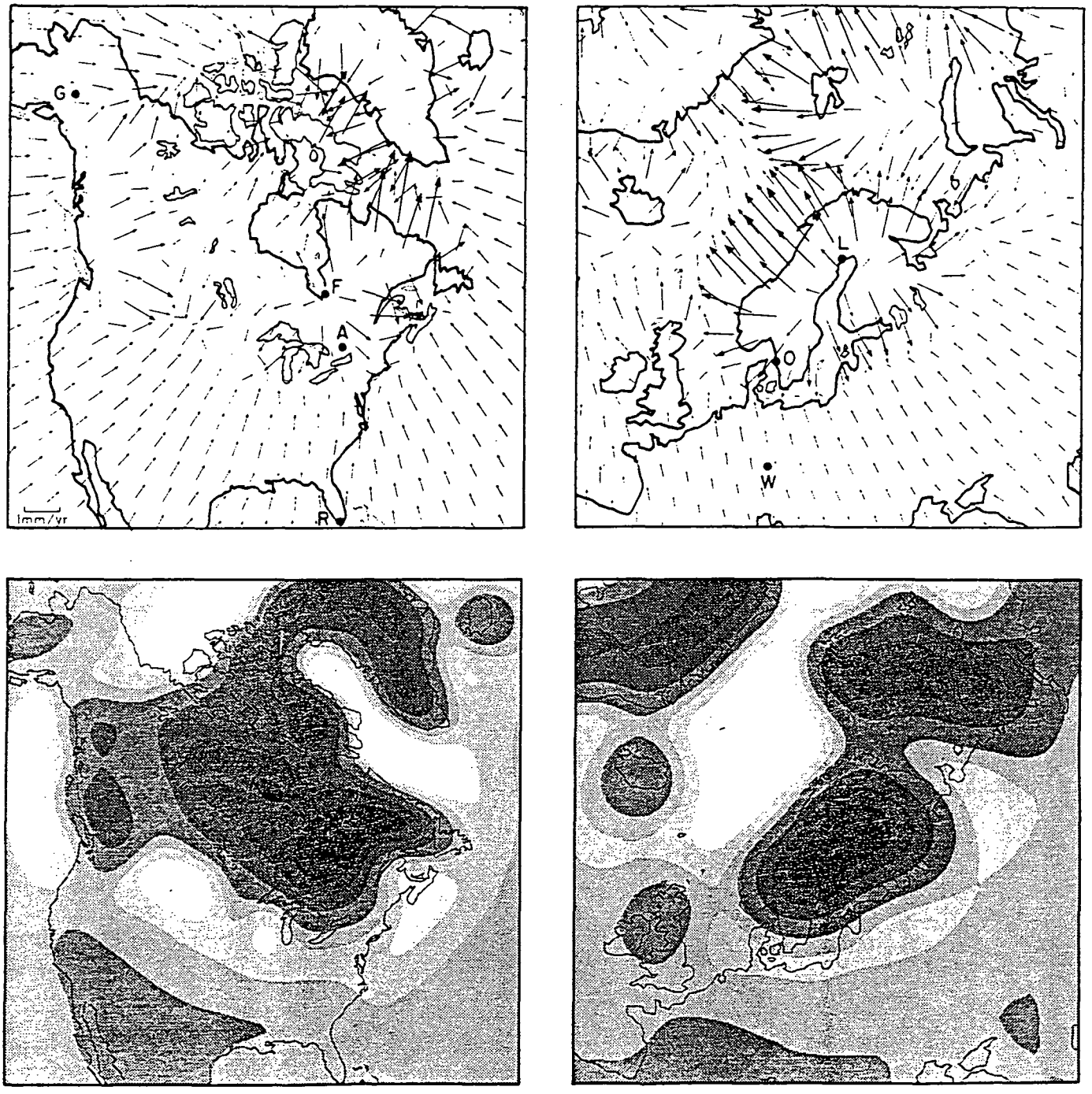
G
F
A
R
1mm/yr
L
W
-4.5 -3.0 -1.5 0.0 1.5 3.0 4.5 6.0 7.5 9.0 10.5 12.0
mm/yr

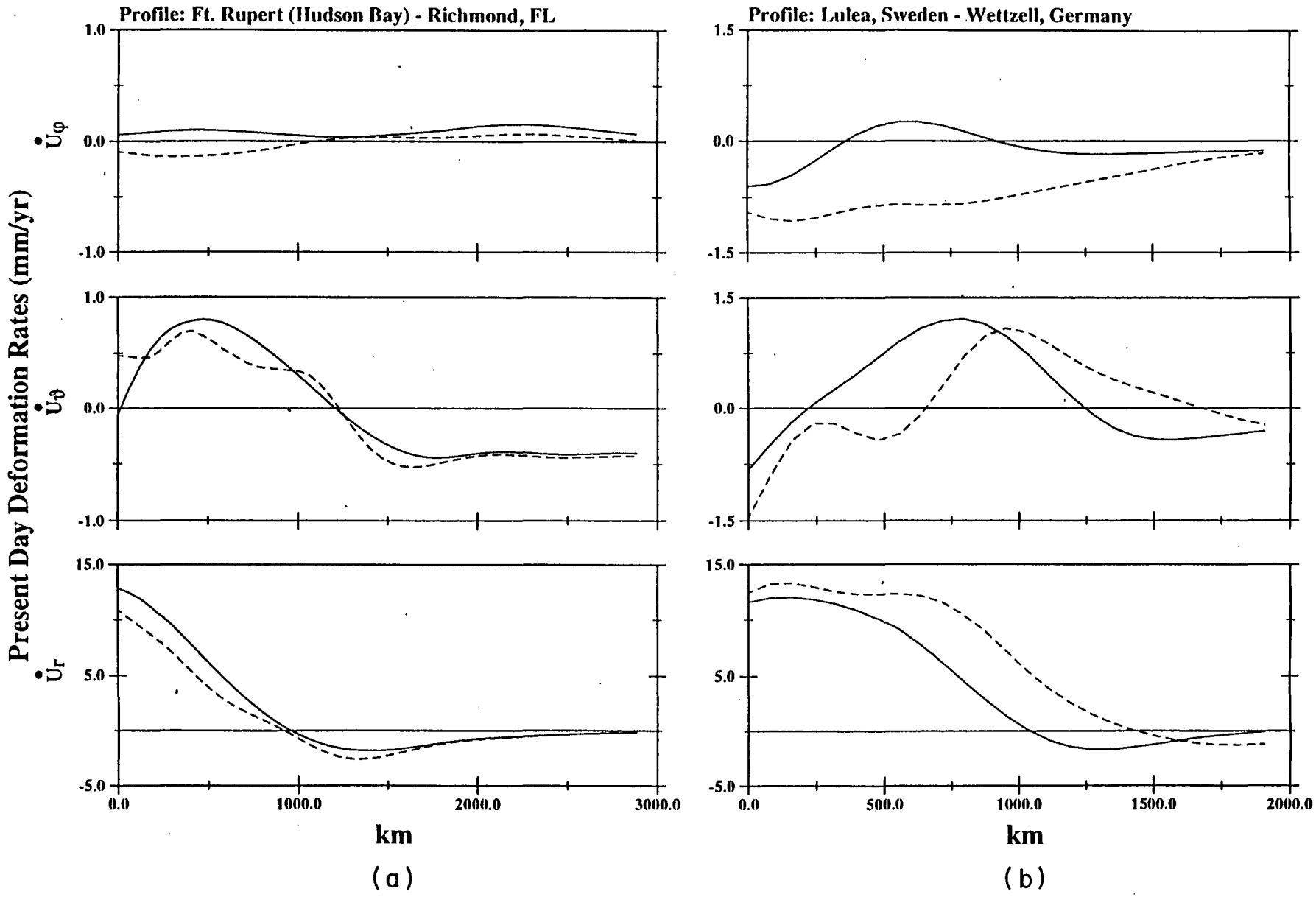
Profile: Ft. Rupert (Hudson Bay) - Richmond, FL
Profile: Lulea, Sweden - Wettzell, Germany
Present Day Deformation Rates (mm/yr)
$\dot{U}_\varphi$
$\dot{U}_\vartheta$
$\dot{U}_r$
1.0
0.0
-1.0
1.5
-1.5
15.0
5.0
-5.0
0.0
500.0
1000.0
1500.0
2000.0
3000.0
km
(a)
(b)

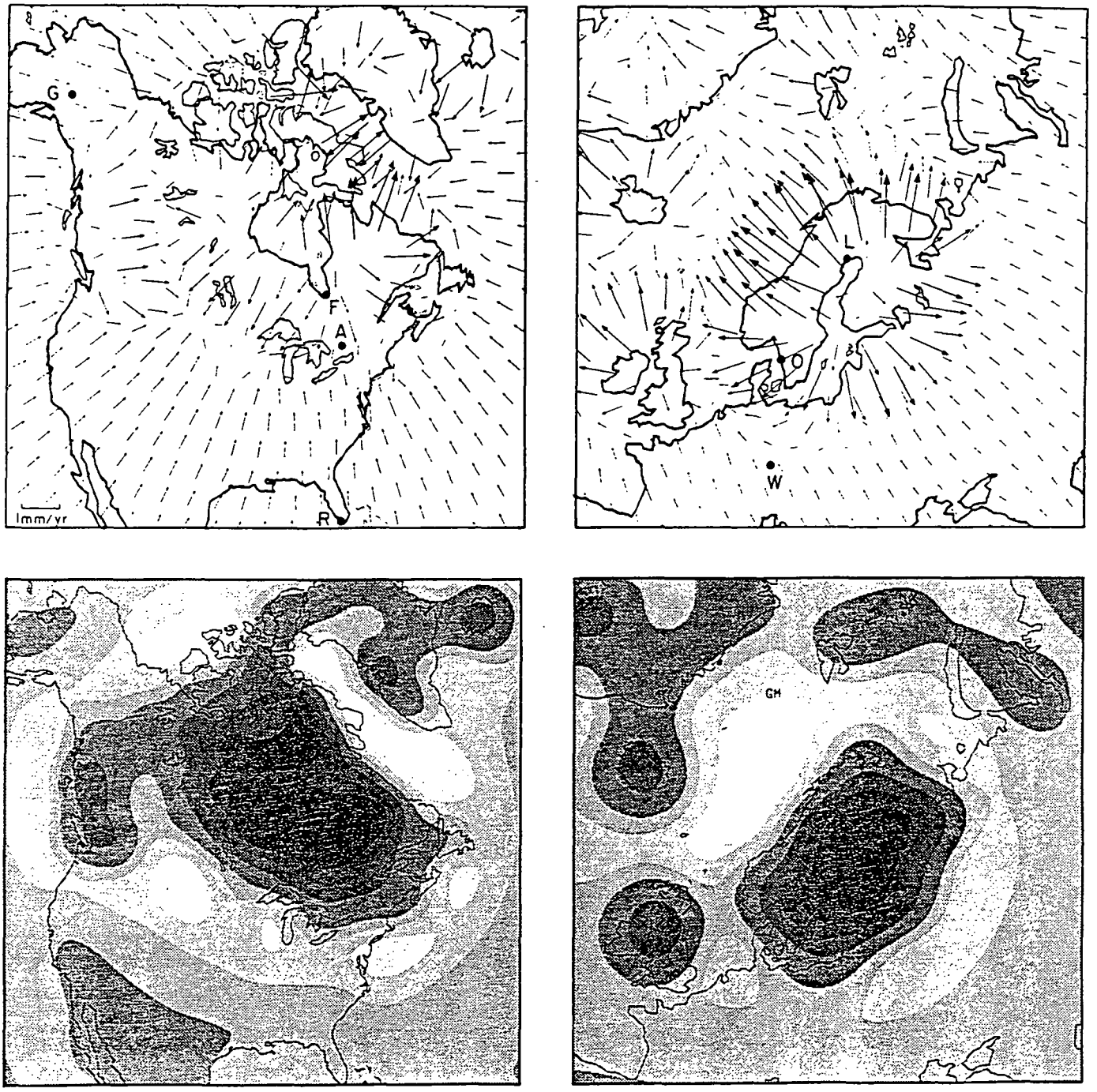
G
F
A
R
1mm/yr
L
W
GH
−4.5 −3.0 −1.5 0.0 1.5 3.0 4.5 6.0 7.5 9.0 10.5 12.0
mm/yr

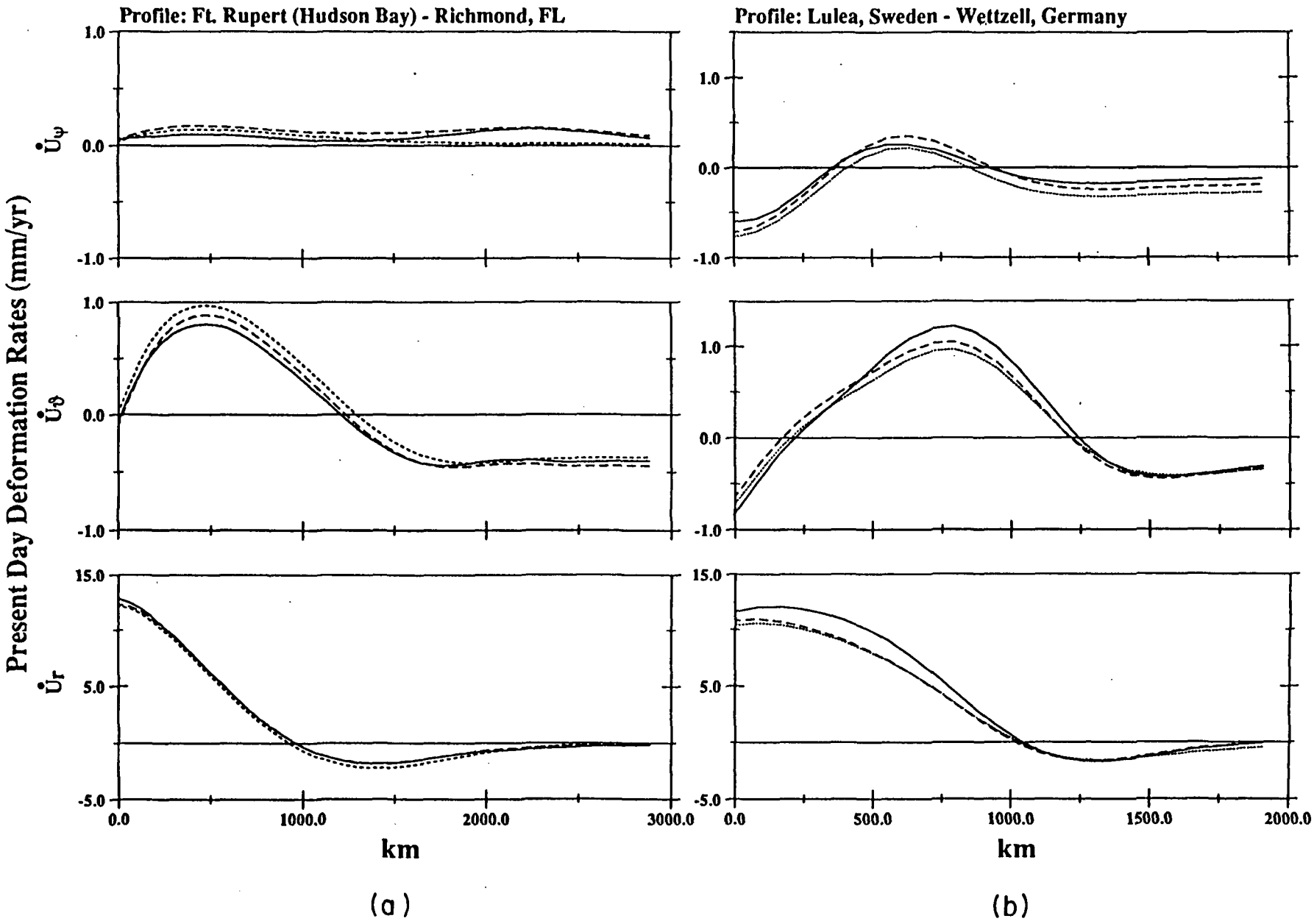
Profile: Ft. Rupert (Hudson Bay) - Richmond, FL
Profile: Lulea, Sweden - Wettzell, Germany
Present Day Deformation Rates (mm/yr)
$\dot{U}_\psi$
$\dot{U}_\vartheta$
$\dot{U}_r$
1.0
0.0
-1.0
15.0
5.0
-5.0
0.0
1000.0
2000.0
3000.0
500.0
1500.0
km
(a)
(b)

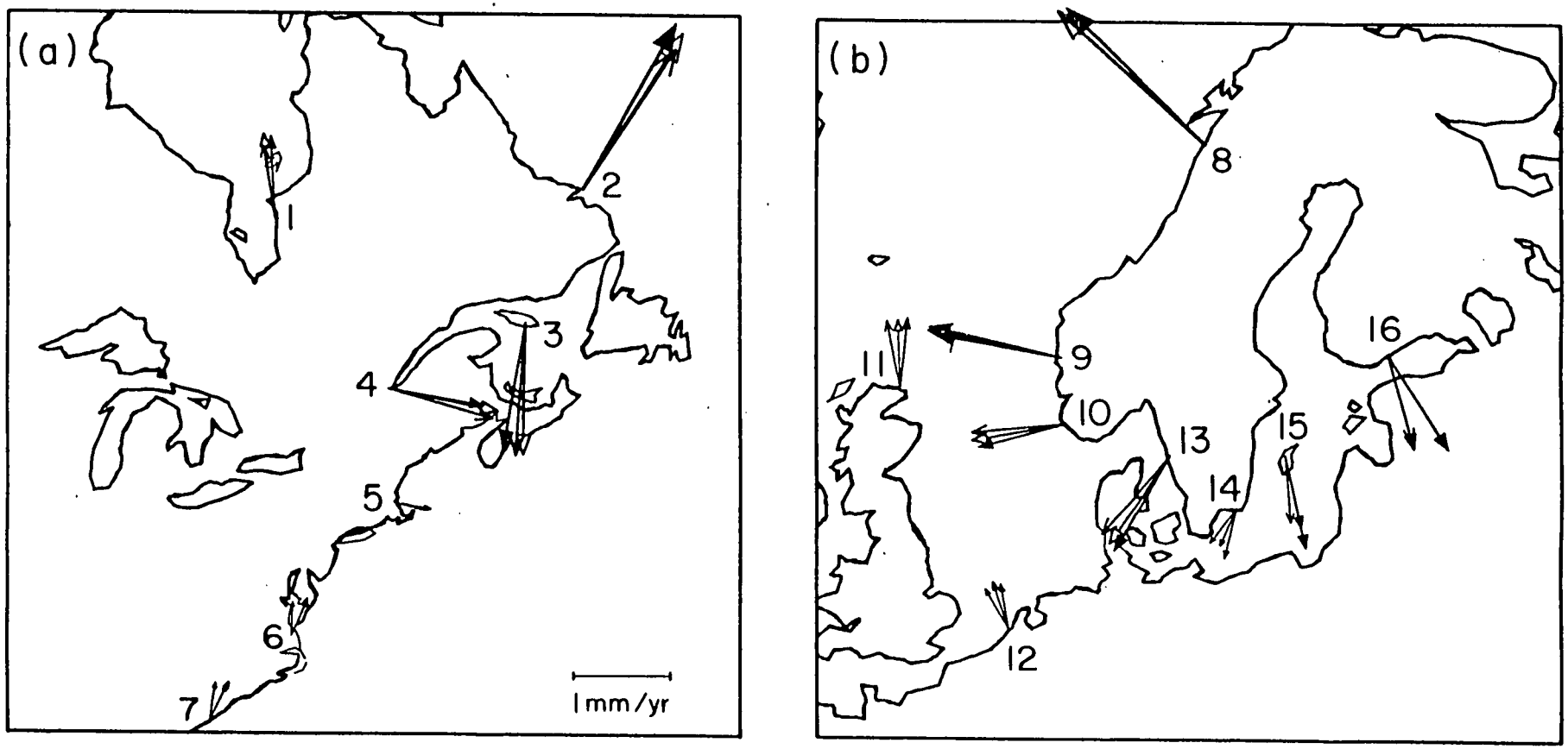
(a)
1
2
3
4
5
6
7
1 mm/yr
(b)
8
9
10
11
12
13
14
15
16

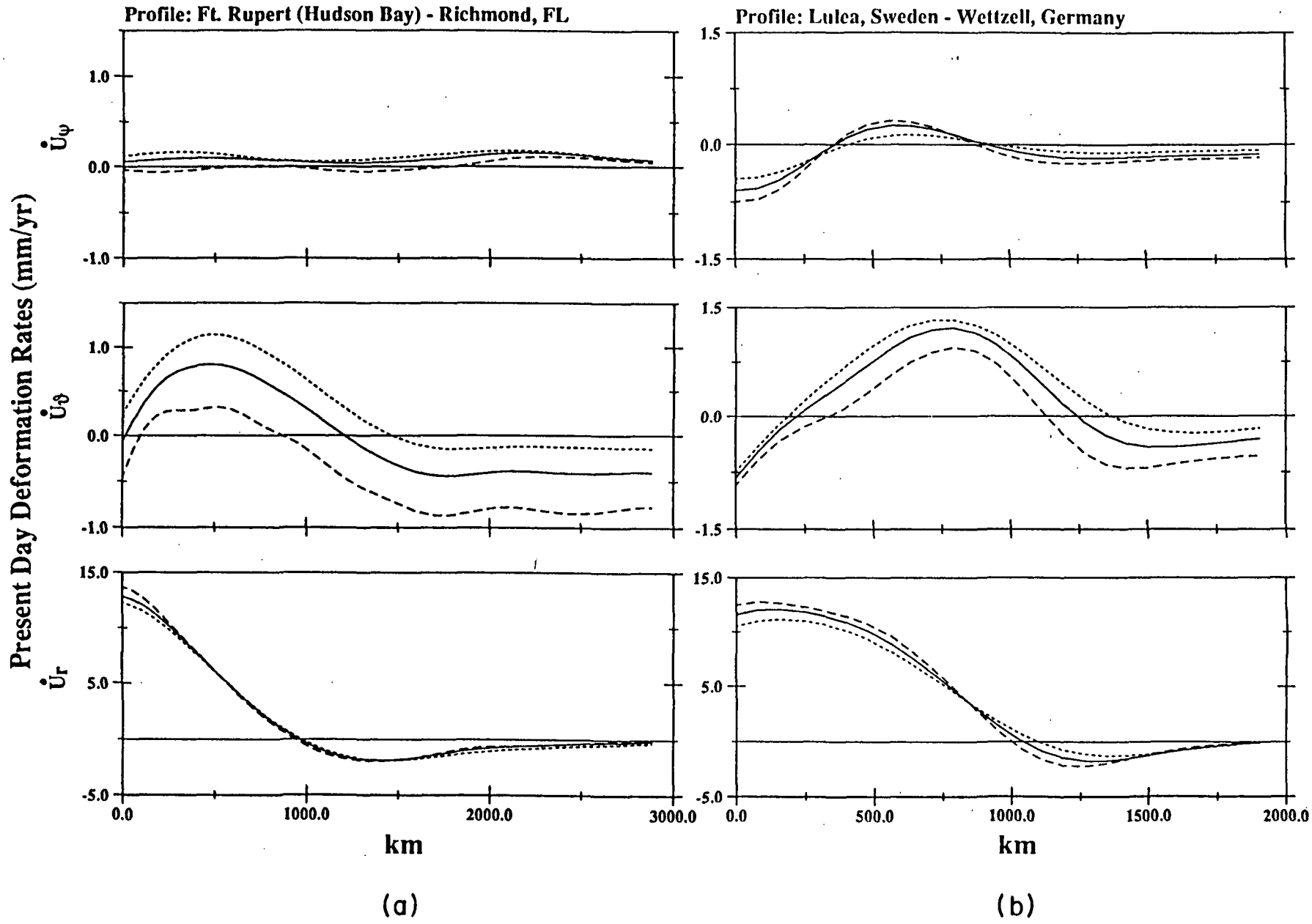
Profile: Ft. Rupert (Hudson Bay) - Richmond, FL
Profile: Lulea, Sweden - Wettzell, Germany
Present Day Deformation Rates (mm/yr)
$\dot{U}_\psi$
$\dot{U}_\theta$
$\dot{U}_r$
1.0
0.0
-1.0
1.5
-1.5
15.0
5.0
-5.0
0.0
1000.0
2000.0
3000.0
500.0
1500.0
km
(a)
(b)

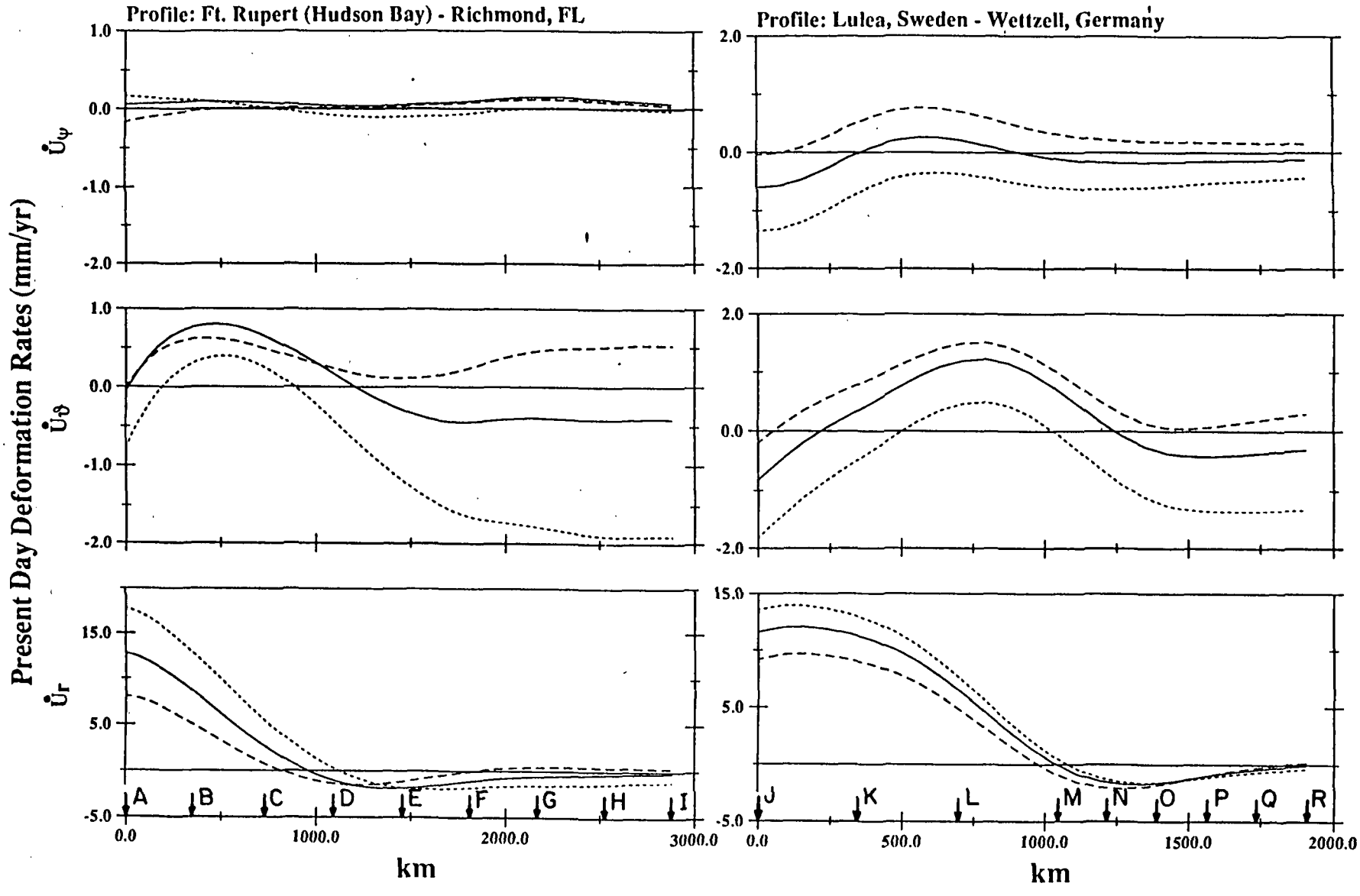
Profile: Ft. Rupert (Hudson Bay) - Richmond, FL
Profile: Lulea, Sweden - Wettzell, Germany
Present Day Deformation Rates (mm/yr)
$\dot{U}_\psi$
$\dot{U}_\vartheta$
$\dot{U}_r$
1.0
0.0
-1.0
-2.0
2.0
15.0
5.0
-5.0
A
B
C
D
E
F
G
H
I
J
K
L
M
N
O
P
Q
R
0.0
1000.0
2000.0
3000.0
500.0
1500.0
km
(a)
(b)

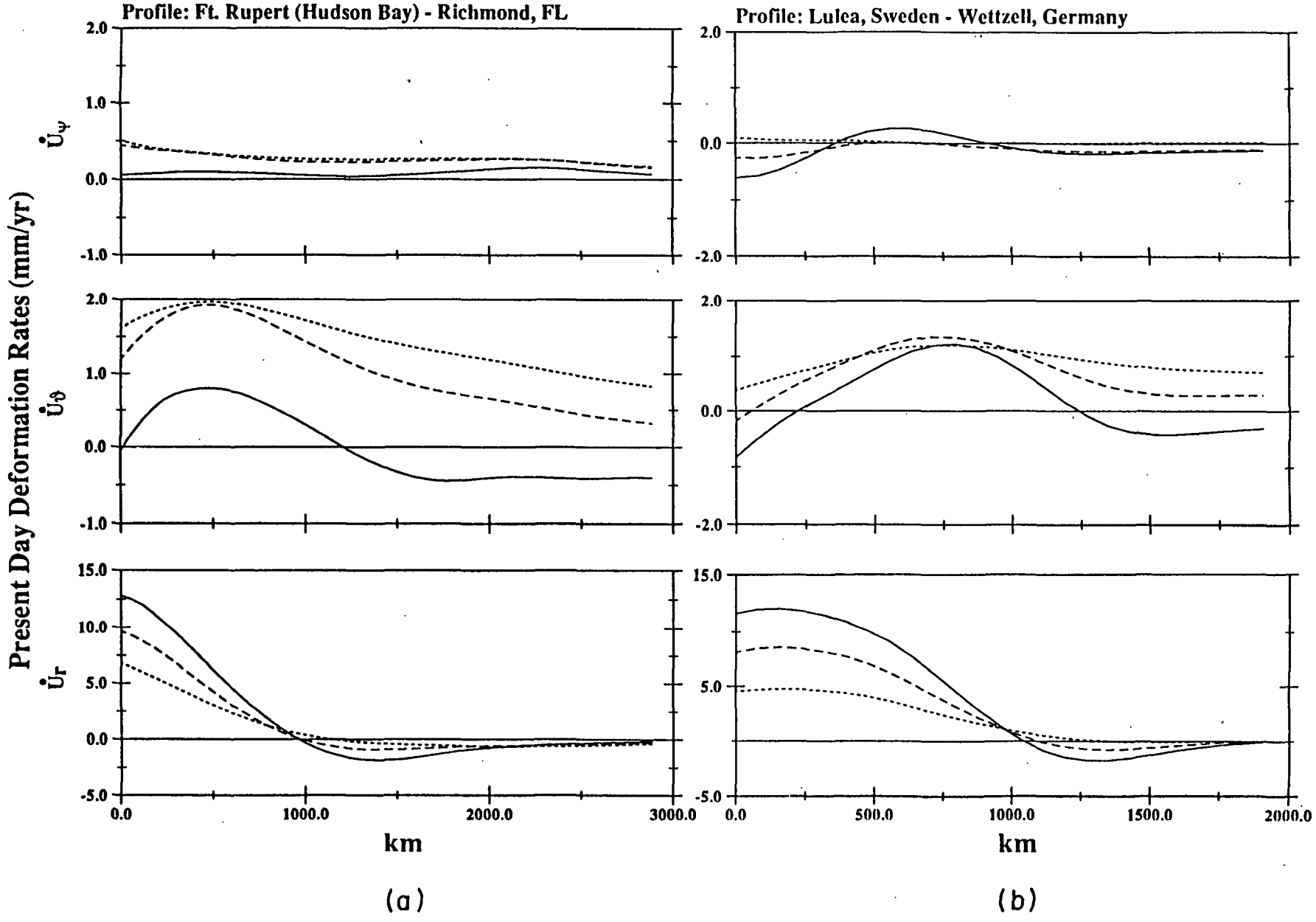
Profile: Ft. Rupert (Hudson Bay) - Richmond, FL
Profile: Lulea, Sweden - Wettzell, Germany
Present Day Deformation Rates (mm/yr)
$\dot{U}_\psi$
$\dot{U}_\vartheta$
$\dot{U}_r$
2.0
1.0
0.0
-1.0
-2.0
15.0
10.0
5.0
-5.0
0.0
1000.0
2000.0
3000.0
500.0
1500.0
km
(a)
(b)

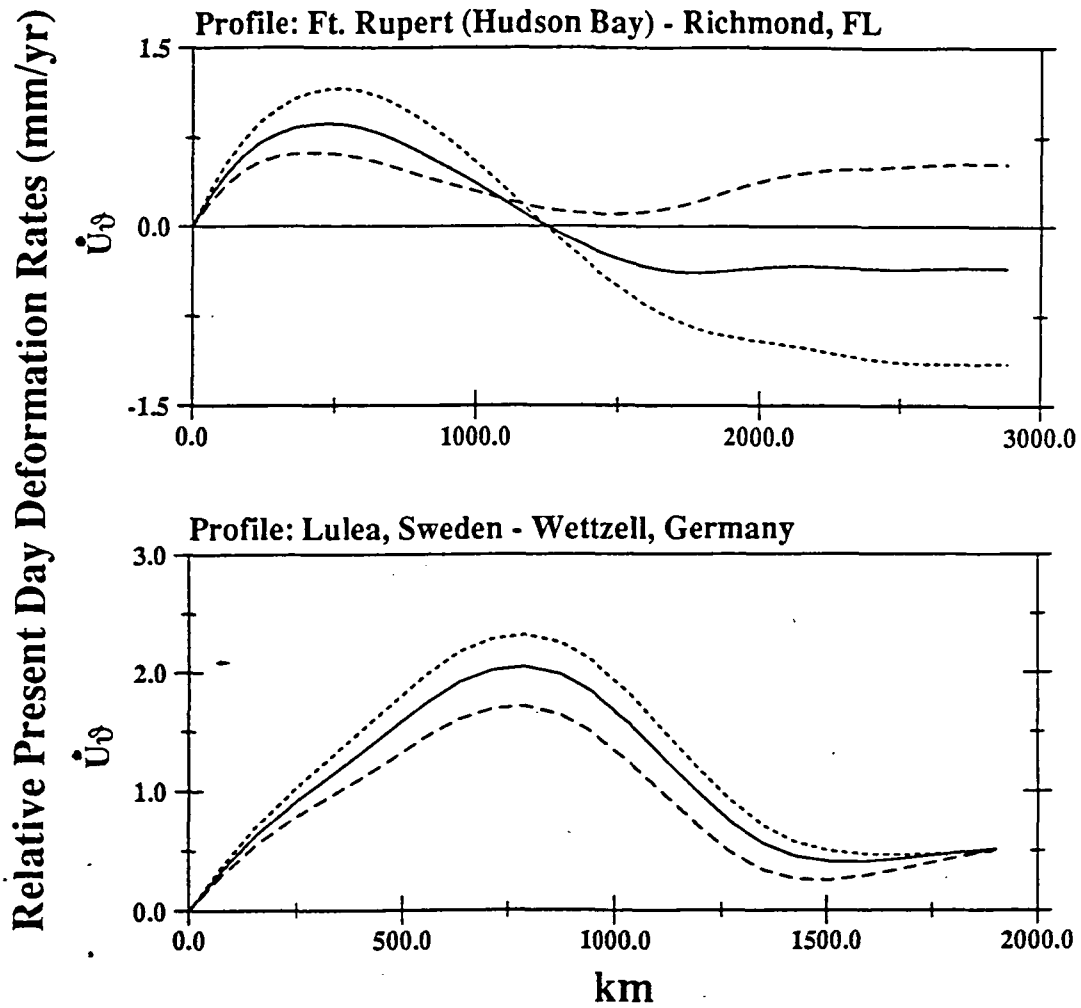
Relative Present Day Deformation Rates (mm/yr)
Profile: Ft. Rupert (Hudson Bay) - Richmond, FL
1.5
0.0
-1.5
$\dot{U}_\vartheta$
0.0
1000.0
2000.0
3000.0
Profile: Lulea, Sweden - Wettzell, Germany
3.0
2.0
1.0
0.0
$\dot{U}_\vartheta$
0.0
500.0
1000.0
1500.0
2000.0
km

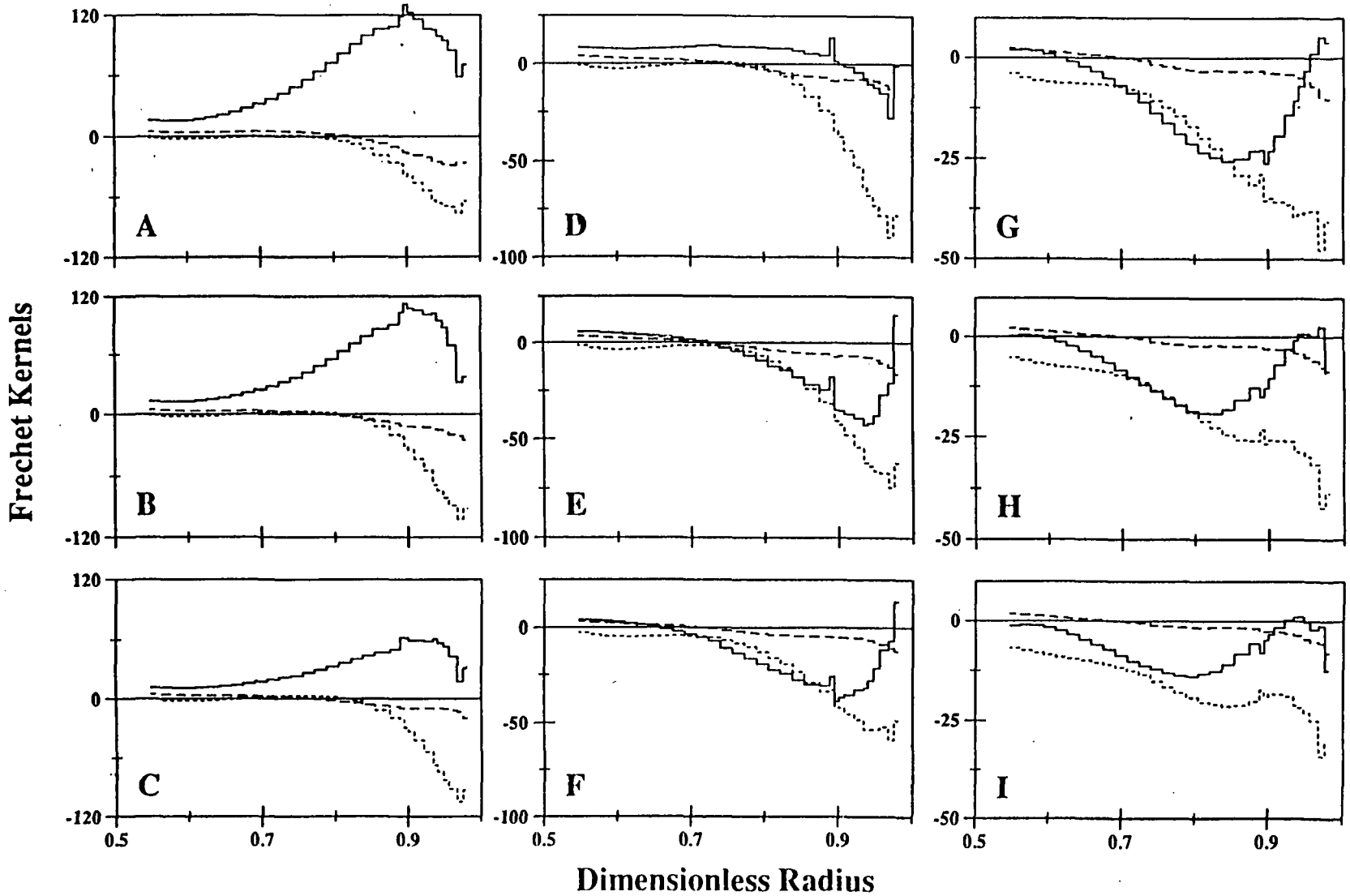
Frechet Kernels
Dimensionless Radius
A
B
C
D
E
F
G
H
I
120
0
-120
-50
-100
-25
0.5
0.7
0.9

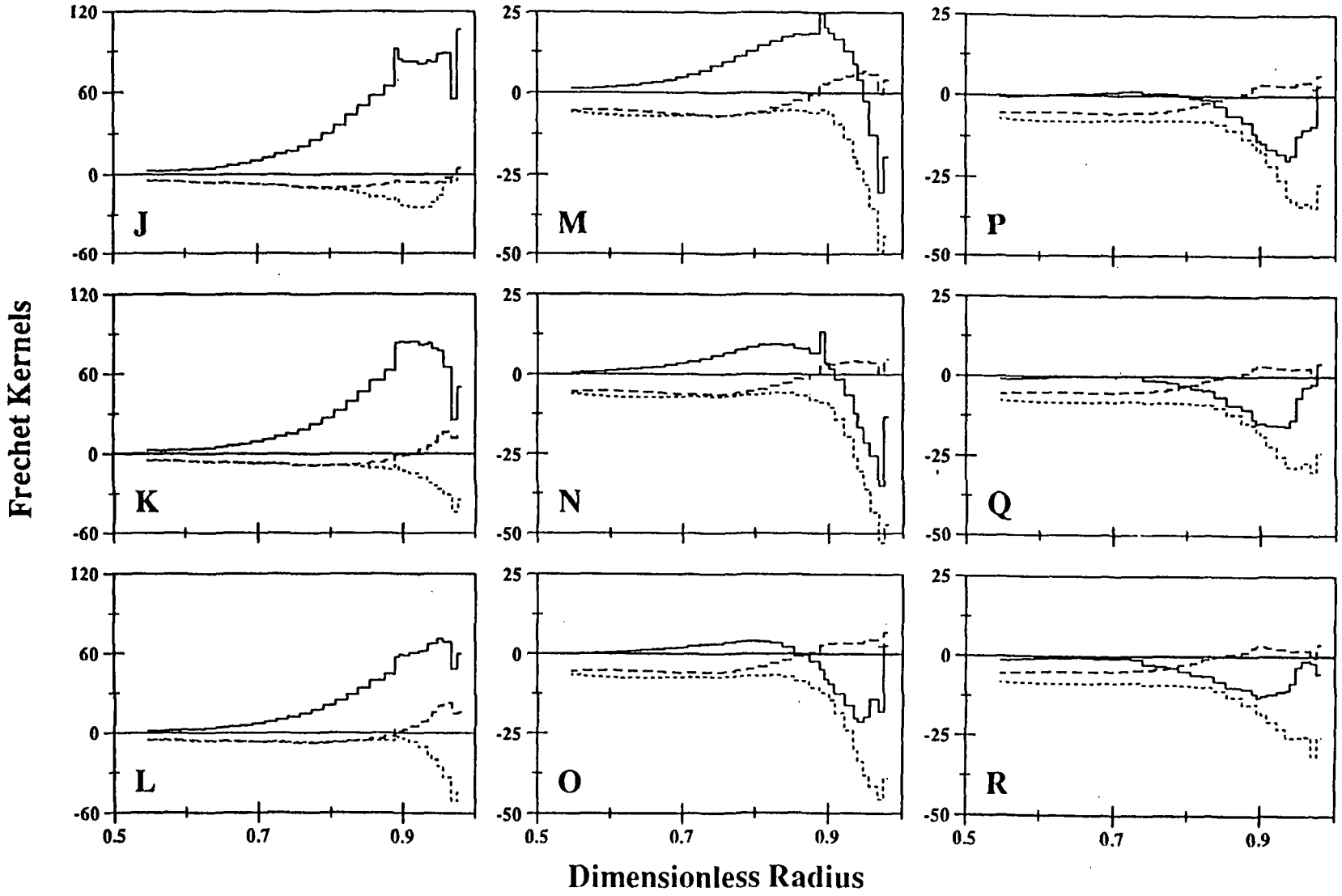
Frechet Kernels
Dimensionless Radius
J
K
L
M
N
O
P
Q
R
120
60
0
-60
25
-25
-50
0.5
0.7
0.9

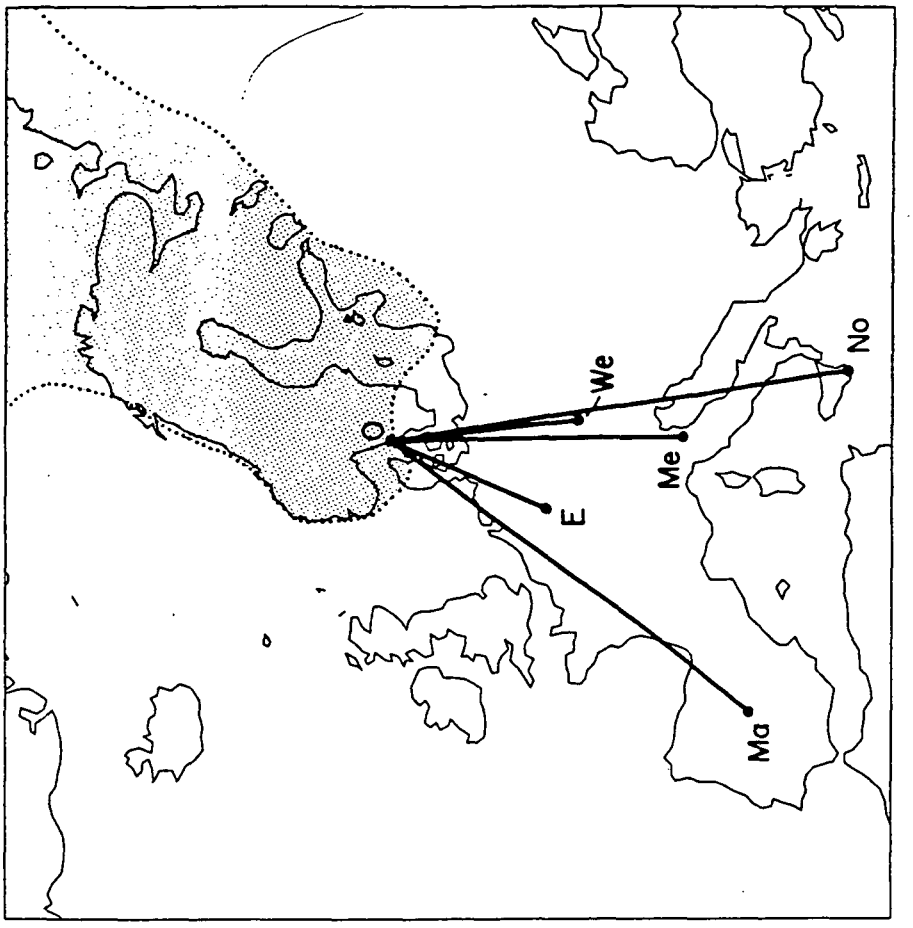
O
We
No
Me
E
Ma

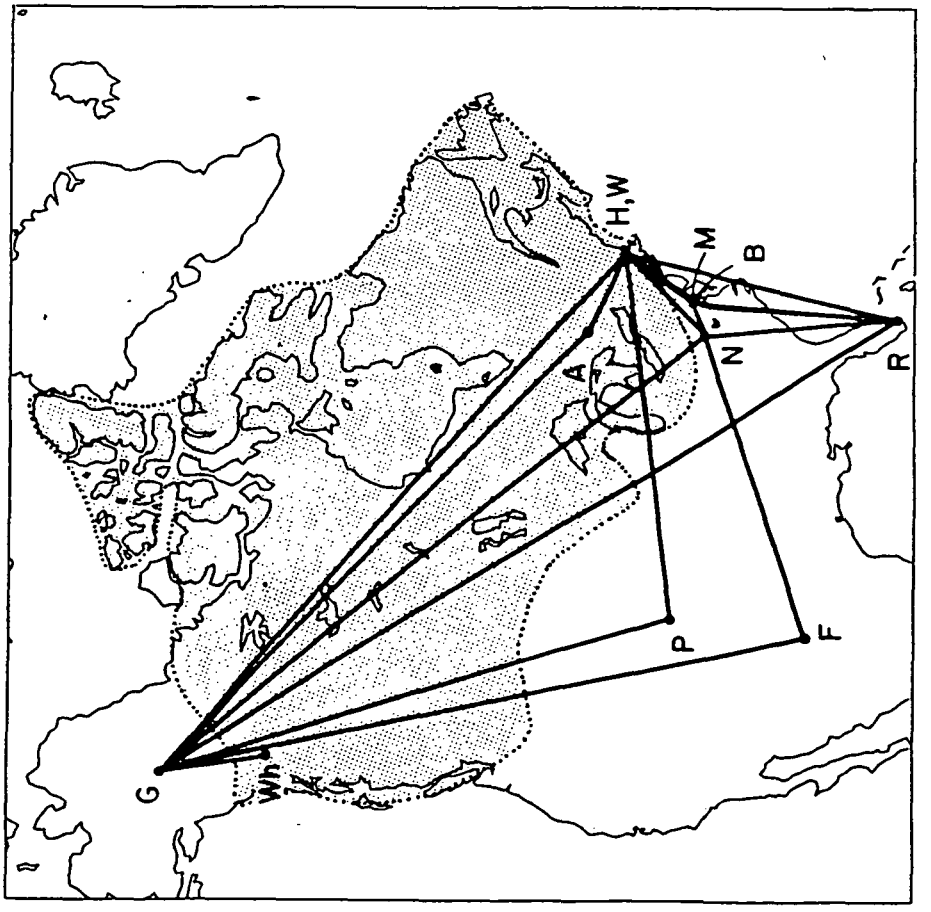
H,W
M
B
N
A
R
P
F
G
Wh

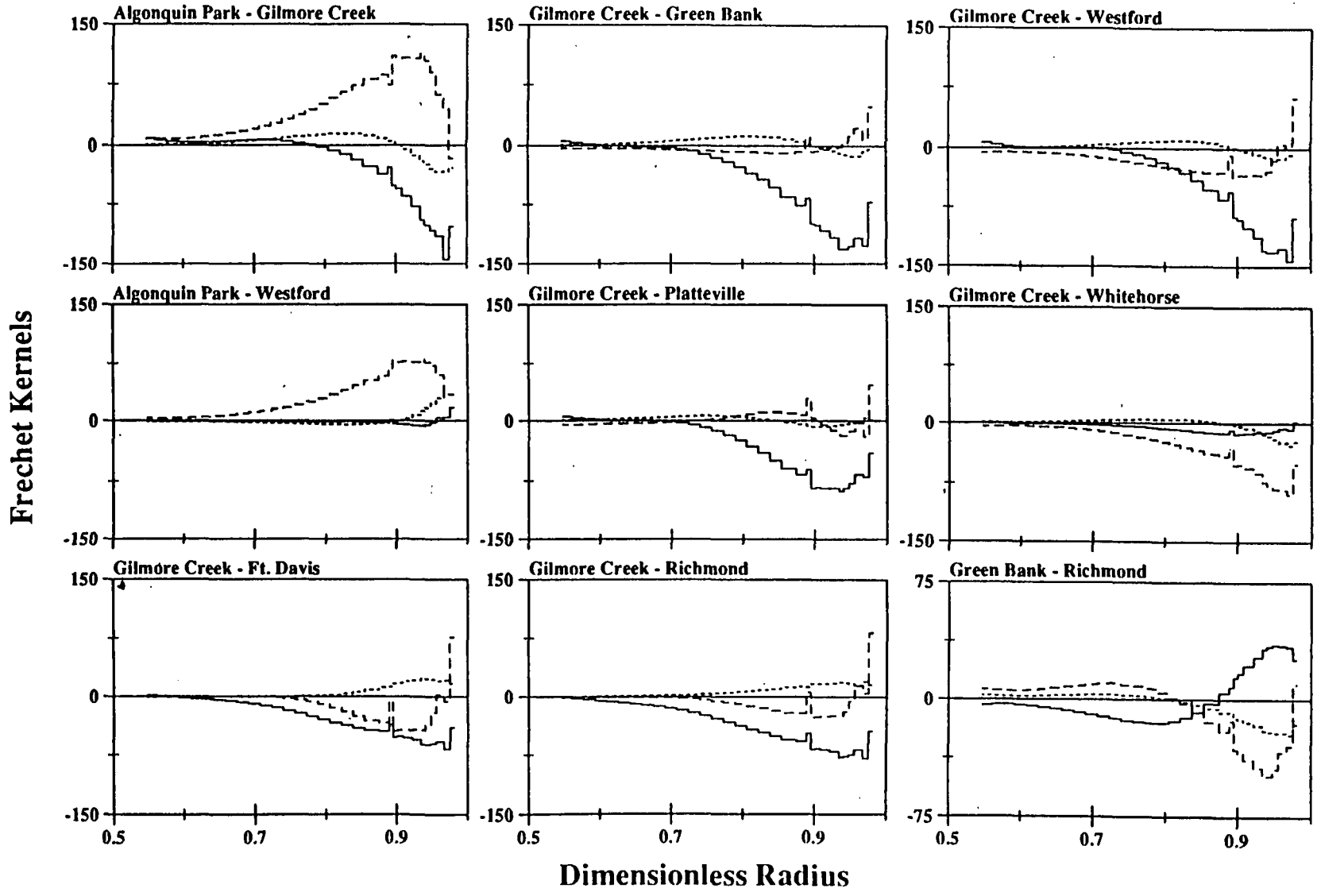
Algonquin Park - Gilmore Creek
Gilmore Creek - Green Bank
Gilmore Creek - Westford
Algonquin Park - Westford
Gilmore Creek - Platteville
Gilmore Creek - Whitehorse
Gilmore Creek - Ft. Davis
Gilmore Creek - Richmond
Green Bank - Richmond
150
0
-150
75
-75
0.5
0.7
0.9
Frechet Kernels
Dimensionless Radius

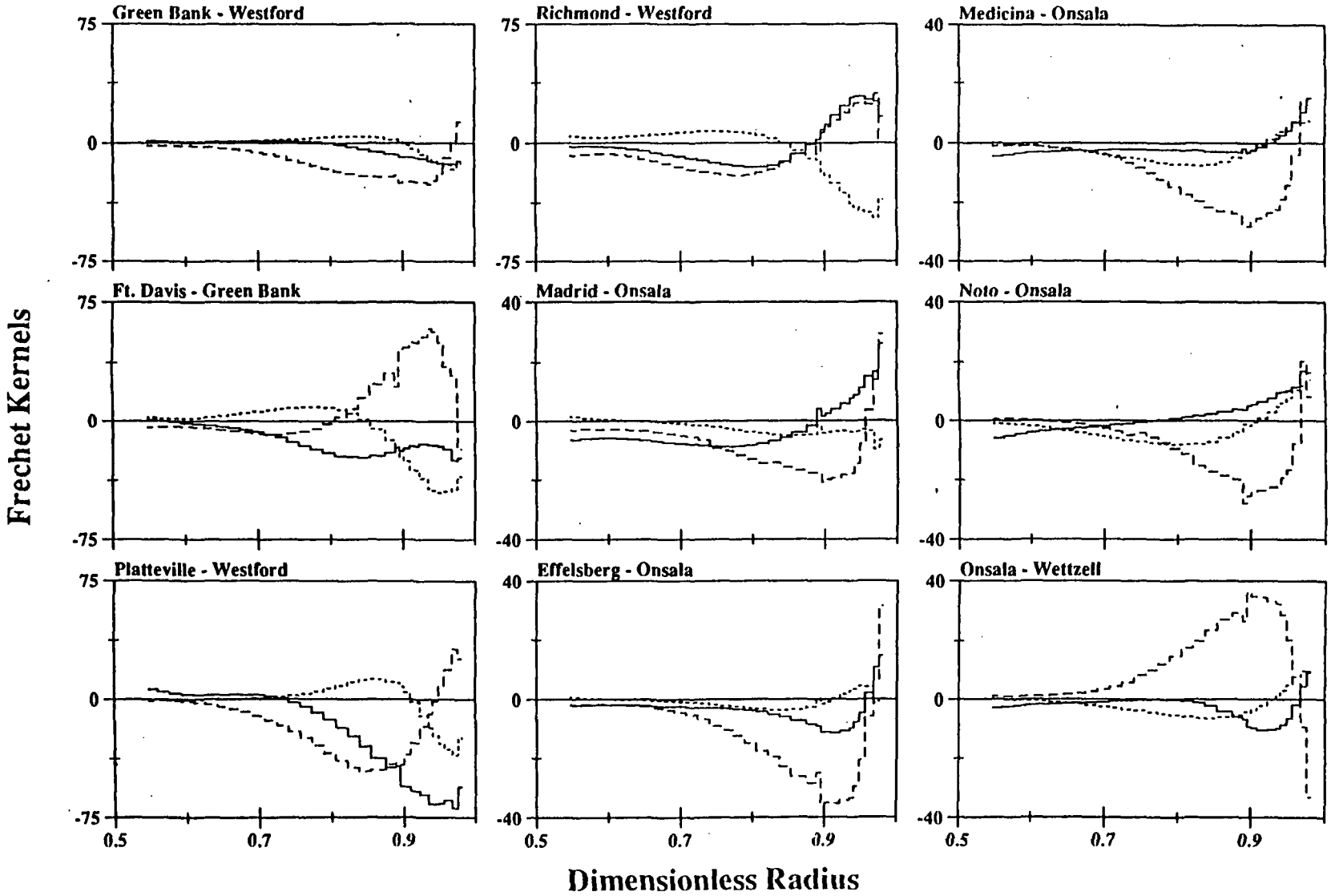
Green Bank - Westford
Richmond - Westford
Medicina - Onsala
Ft. Davis - Green Bank
Madrid - Onsala
Noto - Onsala
Platteville - Westford
Effelsberg - Onsala
Onsala - Wettzell
Frechet Kernels
Dimensionless Radius
75
0
-75
40
-40
0.5
0.7
0.9

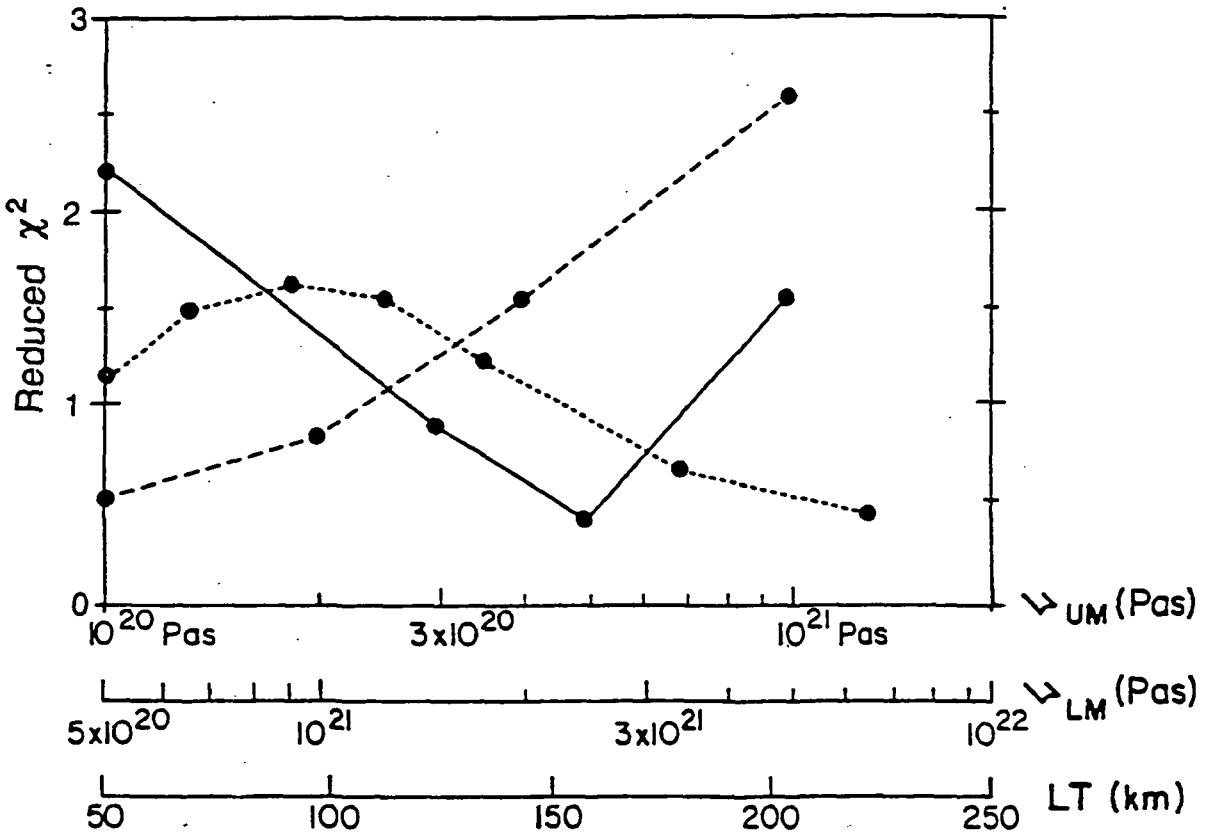
Reduced χ^2
3
2
1
0
10^{20} Pas
3×10^{20}
10^{21} Pas
η_{UM} (Pas)
5×10^{20}
10^{21}
3×10^{21}
10^{22}
η_{LM} (Pas)
50
100
150
200
250
LT (km)